AN ABSTRACT OF THE DISSERTATION OF

Wei-Li Hong for the degree of Doctor of Philosophy in Oceanography presented on March 17, 2014.

Title: Application of Transport-Reaction Modeling to Constrain Biogeochemical Processes in Marine Sediments.

Abstract approved:

_____

Marta E. Torres

Quantifying the mass transport through marine sediments, and the geochemical response to such flow with numerical models has become a common and powerful approach for geochemical data interpretation. In this dissertation, I developed and applied transport-reaction models to unravel complex and interdependent reactions involving carbon, sulfur and silica transformations in shallow marine sediments, and the impact of physical (mass transport deposits) and depositional events (volcanic ash input) on the overall geochemical state of the system.

Carbon cycling in the gas hydrate bearing sediments of the Ulleung Basin was quantified using both box and kinetic modeling approaches. The box model balances mass, flux, and carbon isotopes of carbon (Chapter 2), and led to a better understanding of how methane is cycled in the marine sediments of this area. This effort demonstrates the significance of CO_2 reduction, a previously overlooked reaction. The picture of reaction network derived from this work serves as the foundation for a transport-reaction model (Chapter 3). The kinetic model results revealed a very different biogeochemistry between two distinct fluid-flow environments. At sites where transport is predominantly diffusive (non-chimney

environments), organic matter decomposition is the dominant process driving production of methane, dissolved inorganic carbon (DIC) and consumption of sulfate. In contrast, anaerobic oxidation of methane (AOM) drives both carbon and sulfur cycles in the advective settings characterized by acoustic chimneys indicative of gas transport. I show that methane produced within the model domain, through CO_2 reduction and methanogenesis, fuels AOM in the non-chimney sites while AOM is primarily induced by methane from external sources at the chimney sites. A simulation of the system evolution from a non-chimney to a chimney condition was developed by increasing the bottom methane supply to an originally diffusion-controlled site. Results from this exercise show that the higher methane flux leads to a higher AOM activity, and enhanced organic matter decomposition through methanogenesis.

Organic carbon cycling is also affected by changes in the depositional environment, as shown by application of the kinetic model to the sediments from the Krishna-Godavary (K-G) basin along the eastern Indian margin (Chapter 4). Proximity to large rivers results in the widespread occurrence of mass transport deposits (MTD) throughout the basin. In this work, MTD is defined as a fluidized sediment block whose pore water composition is identical to sea water value to reflect the homogenization process during sediment transport. The pore water sulfate and ammonium profiles measured at seven sites drilled in the K-G Basin during the NGHP-01 expedition were simulated to provide a quantitative description of how MTDs can affect geochemistry profiles, not only for sulfate and ammonium but potentially all pore water species. This model provides reliable estimates of the MTDs thickness, the time elapsed after the most recent event, and the organoclastic sulfate reduction rate at these seven sites.

A transport-reaction modeling approach was also applied to investigate the silica diagenetic reactions fueled by volcanic ash decomposition in Shikuko Basin, Nankai Trough (Chapter 5). The model developed for this setting reproduces a silica diagenetic boundary (SDB) at each site, which is defined by marked decreases in

reactive volcanic ash, pore water silica and potassium. Volcanic ash alteration was constrained by modeling pore water $^{87}Sr/^{86}Sr$ profiles. Below the SDB, formation of clinoptilolite consumes potassium and regulates the extension of amorphous silica by consuming $SiO_{2(aq)}$. The observed low $SiO_{2(aq)}$ and dissolved potassium in these deep sequences require continuous precipitation of clinoptilolite; however in order to maintain oversaturation of this mineral at the low $SiO_{2(aq)}$ in sediments below the SDB, an increase in pH is required, consistent with pore water observations. Thermal history, rather than temperature alone, controls the inferred reaction network as shown by the convergence of the thermal maturity of sediments at the SDB from all studied sites and is consistent with other locations documented onshore Japan. These results are valuable as we move forward in understanding the mechanisms and consequences of ash alteration in convergent margins worldwide.

©Copyright by Wei-Li Hong
March 17, 2014
All Rights Reserved

Application of Transport-Reaction Modeling to Constrain Biogeochemical Processes in Marine Sediments

by
Wei-Li Hong

A DISSERTATION

submitted to

Oregon State University

in partial fulfillment of
the requirements for the
degree of

Doctor of Philosophy

Presented March 17, 2014
Commencement June 2014

Doctor of Philosophy dissertation of Wei-Li Hong presented on March 17, 2014

APPROVED:

Major Professor, representing Oceanography

Dean of the College of Earth Ocean and Atmospheric Sciences

Dean of the Graduate School

I understand that my dissertation will become part of the permanent collection of Oregon State University libraries. My signature below authorizes release of my dissertation to any reader upon request.

Wei-Li Hong, Author

ACKNOWLEDGEMENTS

I still remember the joy when I first received the email from Marta in 2009 saying that she was happy to consider my application. That email was my ticket to a whole new world. Survival was, however, not easy for me, as an international student. Difference in culture and language was a great barrier to develop new friendships. Away from family and friends made me feel homesick frequently. I still remembered, too, how awkward I felt when I attended a party where I did not know how to start a conversation with others. I am, now, more adapted and even fall in love with the beautiful Oregon and the lovely people here. Many people I have met for the past four and half years helped me get over the hard times.

My adviser and friend, Dr. Marta Torres, helps and supports me constantly for the past four and half years. Her enthusiasm, patient, and encouragement keep motivate me to complete this dissertation. Much appreciation to the members in my committee: Dr. Robert Harris, Dr. Clare Reimers, Dr. Glenn Spinelli, and Dr. Brian Wood (alphabetical order). Valuable and critical comments from you all help shape this dissertation. Thanks for the CEOAS family. Many of you treat me with great patient and company me through different hurdles.

Big thanks to my beloved mom, dad, and brother. Your support makes this possible.

CONTRIBUTION OF AUTHORS

Dr. Ji-Hoon Kim, Mrs. Jiyoung Choi, and Dr. Jang-Jun Bahk assisted with collection and interpretation of data from the works included in Chapter 2 and 3.

Dr. Evan A. Solomon assisted in data collection and interpretation for the work included in Chapter 4.

Dr. Glenn A. Spinelli assisted in data collection and interpretation of the work in Chapter 5, as well as the design and writing of Chapter 5 (the "5.5.5 Role of sediment thermal history" section).

TABLE OF CONTENTS

Page

CHAPTER 1 General Introduction 2

CHAPTER 2 Carbon cycling within the sulfate-methane-transition-zone in marine sediments from the Ulleung Basin 11

2.1 Abstract 12
2.2 Introduction 13
2.3 Study area and sediment properties 14
2.4 Analytical method and results 15
2.4.1 Sample collection 15
2.4.2 Analytical approaches 16
2.4.3 Analytical results 17
2.5 Box model framework 18
2.5.1 Transport terms 20
2.5.2 Reaction terms 22
2.5.3 Assessment of the error associated with flux estimates 24
2.6 Model evaluation 24
2.7 Discussion 29
2.7.1 Carbon cycling around the SMTZ in Ulleung Basin 29
2.7.2 Evidence for coupling AOM and CR in natural and laboratory studies 31
2.7.3 Future improvements 32
2.8 Conclusion 33
2.9 Acknowledgements 34

CHAPTER 3 Towards quantifying the reaction network around the sulfate-methane-transition-zone in the Ulleung Basin, East Sea, with a kinetic modeling approach ... 48

3.1 Abstract 49
3.2 Introduction 50
3.3 Model architecture 51

TABLE OF CONTENTS (Continued)

Page

3.3.1 Fundamental parameters 51
3.3.2 Reaction network and carbon isotopes 53
3.3.3 Reaction Formulation 55
3.3.4 Model-experiment setup 57
3.4 Pore water data and geochemical environment 58
3.5 Results and Discussion 58
3.5.1 DIC cycling around SMTZ 59
3.5.2 CH_4 cycling around SMTZ 60
3.5.3 Sulfur cycling around SMTZ 61
3.5.4 Kinetic model vs. box model approaches 62
3.5.5 Model experiment result 64
3.6 Conclusions 65
3.7 Acknowledgements 67

CHAPTER 4 A kinetic-model approach to quantify the effect of mass transport deposits on pore water profiles in the Krishna-Godavari Basin, Bay of Bengal 86

4.1 Abstract 87
4.2 Introduction 88
4.3 Study region 88
4.4 Effect of MTDs on the pore water data 89
4.5 Model architecture 90
4.5.1 Reaction formulation 90
4.5.2 Model logistics 92
4.5.3 Porosity, formation factor, and formation temperature 93
4.5.4 Sensitivity tests 94
4.6 Results and discussion 95
4.6.1 Model-estimated MTD scale and age 95
4.6.2 Sulfate reduction dynamics in the MTD sections 96
4.6.3 Influence of MTDs on pore water profiles 98
4.7 Conclusions 99

TABLE OF CONTENTS (Continued)

Page

4.8 Acknowledgement 100

CHAPTER 5 Diagenetic formation and dissolution of silica in sediments approaching the Nankai margin subduction zone 111

5.1 Abstract 112
5.2 Introduction 113
5.3 Background and Hypothesis 114
5.4 Methods 116
5.4.1 Modeling Scheme 116
5.4.2 Temperature and porosity 118
5.4.3 Chemical transport parameters 119
5.4.4 Chemical species 119
5.5 Results and discussion 119
5.5.1 Silica release above the SDB: Amorphous silicate precipitation and ash decomposition rate 119
5.5.2 Dissolved silica uptake below SDB: Role of aluminosilicate minerals 122
5.5.3 Carbonate and pH control 124
5.5.4 Reaction network controlling the kinetics of amorphous silica 125
5.5.5 Role of sediment thermal history 127
5.6 Implications 130
5.7 Conclusions 131
5.8 Acknowledgements 132

CHAPTER 6 General Conclusion 147

Bibliography 148

Appendix 163

Appendix 1 Table of parameters used in the box model in Chapter 2 163

Appendix 2 The CrunchFlow input file for the transport-reaction model in Chapter 3 165

Appendix 3 CrunchFlow database used for the transport-reaction model in Chapter 3 169

Appendix 4 Graphic presentation of the model scheme in Chapter 5. 173

Appendix 5 Test of different lower boundary conditions in Chpater 5. 174

Appendix 6 Sensitivity tests on ash alteration rate using Sr isotopes and volcanic ash content in Chapter 5. 175

Appendix 7 Model setup for the tests of different lower boundary conditions in Chapter 5. 176

LIST OF FIGURES

Figure Page

Figure 2-1 The definitions of SMTZ and ESMTZ considered in our model.....35

Figure 2-2 Map of the UBGH2 drill sites in the Ulleung Basin. 36

Figure 2-3 Porosity profiles of the study sites. 37

Figure 2-4 Pore water profiles of data available for the box model. 38

Figure 2-5 Framework of our box model.....39

Figure 2-6 The isotopic fractionation factors for AOM (α_{AOM}) calculated from our box model based on the 4 different settings 40

Figure 2-7 (A) Relationship between fraction of organic matter that is consumed by sulfate reduction (*f*) and isotopic fractionation of AOM (α_{AOM}). (B) Relationship between the fraction of organic matter that is consumed by sulfate reduction (*f*) and the fraction of DIC that is recycled by AOM (*b*).....41

Figure 2-8 The relative contribution of each reaction. 42

Figure 3-1 Map of the eight sites drilled during the 2010 Ulleung Basin gas hydrate drilling expedition (UBGH2) used in this study. 68

Figure 3-2 : Reaction network considered in our kinetic model.....69

Figure 3-3 Carbon isotopic profiles of dissolved inorganic carbon (DIC) and methane. 70

Figure 3-4 Model results for (a) the five non-chimney sites and (b) the three chimney sites. 71

Figure 3-5 Depth-integrated rates estimated from our kinetic model at all sites...73

Figure 3-6 Correlations between external methane flux and (a) SMTZ depth and (b) thickness of gas hydrate occurrence zone (GHOZ). 76

Figure 3-7 Comparisons of reaction rates estimated by the box model (Hong et al., 2013) and the current kinetic model. 77

Figure 3-8 Evolution of a system from a low methane flux to one of high methane flux. 78

Figure 3-9 Cartoon illustrates the different modes of carbon cycling around SMTZ in the (a) non-chimney and (b) chimney environments. 79

Figure 4-1 map of the study area 102

LIST OF FIGURES (Continued)

Figure Page

Figure 4-2 Schematic diagram showing the steps involved in the transport-reaction model to simulate the effect of MTDs on pore water sulfate profiles. 103

Figure 4-3 Simulation conducted at Site 5C to test the sensitivity of the model to the Δx, Δt_1 and k_{OM} parameters..... 104

Figure 4-4 Model results and the observed sulfate, methane, and ammonium profiles at the seven study sites. 105

Figure 4-5 Correlation between water depth and the average depositional rate ($\Delta x/\Delta t$). 107

Figure 4-6 Conceptual model to exaplain the sulfate profile at Site 15A..... 108

Figure 5-1Map showing the 4 sites investigated in this study (Sites 1173, 1177, C0011, and C0012) and three additional sites discussed (Site 297, 808, and 1174). 134

Figure 5-2 Pore water Si and K from site 808 and the predominated mineral assemblages identified by XRD in Masuda et al. (1993)..... 135

Figure 5-3 Strontium isotopic profiles at (A&B) Sites C0011 and (C&D) C0012 (Joseph et al., 2013) 136

Figure 5-4 Illite, smectite, and clinoptilolite solubility at the current pore water composition in our four study sites. 137

Figure 5-5 Observed (closed dots) and modeled (blue lines) profiles of key pore water species and volcanic ash for the four study sites. 138

Figure 5-6 Reaction network proposed in the three reaction zones..... 140

Figure 5-7 Temperature and thermal maturity dependency of SDB at the four study sites and Site 808 142

LIST OF TABLES

Table Page

Table 2-1 Depth of the BSR, first appearance of gas hydrate and the SMTZ, as well as organic carbon content of the study sites 43

Table 2-2 Parameters used to fit the porosity profiles shown in Figure 2-2 44

Table 2-3 Fluxesof various solutes across the SMTZ calculated from pore water profiles. 45

Table 2-4 Error of flux estimates for each of the dissolved species considered in our model 46

Table 2-5 Range of the depth-integrated reaction rates (μmol/cm^2/yr) derived from Case 4. 47

Table 3-1 List of pore water and solid species considered in the model 80

Table 3-2 Site-specific information 81

Table 3-3 Full list of reactions considered in the model 82

Table 3-4 Model input parameters 83

Table 3-5 Values of Gibbs free energy used to calculate the equilibrium constants of AOM and CO_2 reduction 84

Table 3-6 Depth integrated rates for all study sites 85

Table 4-1 Water depth and the location of the seven study sites. 108

Table 4-2 Input parameters for model simulations. 109

Table 4-3 Model-derived results 110

Table 5-1 Initial and boundary conditions of all sites 142

Table 5-2 Reaction rates 143

Table 5-3 Histories of sedimentation rate and basal heat input 144

Table 5-4 Temperature and sum of TTI at SDB of each site 146

Application of Transport-Reaction Modeling to Constrain - Biogeochemical Processes in Marine Sediments -

CHAPTER 1 General Introduction

Quantifying the mass transport of solutes and solid phases through marine sediments, and the geochemical response to such flow with numerical model approaches has become a common and powerful tool for geochemists to interpret their data. The root of such models can be traced back to as early as the 1960s, when Garrels and Thompson (1962) first applied chemical modeling to predict the distribution of species and equilibrium of minerals with ambient waters. About the same time, Helgeson (1968) presented the first geochemistry model that was able to run with computers. Led by this first generation computerized model, the knowledge of numerical modeling and its application rapidly advanced (e.g., Berner, 1971; Helgeson et al., 1974a; 1974b; 1976; 1981; Wolery, 1978). Wolery (1979) developed the first software package, EQ3/EQ6, that was made available to the broad geochemistry community. Since then, numerous studies have applied this approach to constrain a myriad of processes in marine sediments (e.g., Berner, 1980; Boudreau, 1996; Bethke, 1996; 2008; Luff et al., 2000; Wallmann et al., 2006; Regnier et al., 2011).

The strength of this approach is clearly documented by Boudreau (1996). In particular, a mathematical description of diagenetic processes that is based on physical, chemical, and geological principles is critical to any robust assessment and hypothesis testing that involve complex geochemical systems. Any synthetic consideration that includes all the system components is usually impossible without quantification of all processes involved and a proper tool to evaluate different scenarios that can be constrained by data. In addition, numerical modeling can simulate the temporal evolution of a system and provide insights on how a system may respond to perturbations. It is not always possible to directly observe the temporal evolution or the response of a system to various forcing mechanisms (e.g., temperature changes, variations in flow, sediment slumping, volcanic eruptions). Lastly, numerical modeling can be used to evaluate laboratory observations, which very often disturb the system as the experiments are being performed.

Throughout this dissertation, I use a numerical transport-reaction model to highlight two important phenomena: transport and reaction between fluid and solid. Different names have been given for the same type of modeling approach by different investigators. For example, Berner (1980) and Boudreau (1996) describe it as "diagenetic modeling" and focused on the ability of a model to simulate property changes in sediments or sedimentary rocks upon deposition from the water column. Bethke (1996; 2008) named it "geochemical modeling" to emphasize the ability to include thorough geochemical considerations. Here I stress the importance of both transport and reaction terms, based on the "reactive flow and transport model" approach by Dr. Carl Steefel (Steefel and Maher, 2009). I consider both components to be equally important as the transport of fluid and solids can initiate new reactions, which will then modify the physical properties of the system and consequently the transport behavior.

This dissertation consists of four published or submitted papers that address three different topics, but all four aim to understand the interactions between fluid and solid transport with geochemical reactions. I made strong use of CrunchFlow (Steefel, 2009), a FORTRAN-based model routine developed by Dr. Carl Steefel from Lawrence Berkeley National Laboratory. In the following paragraphs I will introduce CrunchFlow and how the transport and reactions are formulated in the software. I will then briefly present the focus of each individual topic. The rationale and modifications to the model are fully described in each of the thesis chapters.

Short introduction of CrunchFlow

A description of CrunchFlow is detailed by Steefel (2009), here I only present a short introduction to the software. The governing equation in CrunchFlow is the conservation of solute mass (Steefel, 1992; Steefel and Lasaga, 1994):

$$\frac{\partial}{\partial t}(\phi\rho_f M_{H_2O}U_i) + \nabla\bullet\left[-D\nabla(\rho_f M_{H_2O}U_i) + u\rho_f M_{H_2O}U_i\right] = R_i \ \ (i = 1,2,...N_{tot}) \quad (1.1)$$

where U_i is the molal concentration of solute, M_{H2O} is water mass fraction, ρ_f is fluid density, ϕ is porosity, D is diffusion coefficient, u is fluid advection rate, R is the sum

of all reactions that influence solute concentration, and N_{tot} is the number of solute species considered. The concept of total concentration (Reed, 1982; Lichtner, 1985; Kirkner and Reeves, 1988) was adapted in CrunchFlow to reduce the number of independent species that need to be solved, as follows:

$$U_i = C_p + \sum_{s=1}^{n} v_{sp} C_s \quad (1.2)$$

U_i is the total concentration of an element in a solvent (e.g., total aluminum in a solvent). This total concentration can be partitioned into primary species (e.g., Al^{+3} with concentration of C_p) and secondary species (e.g., $Al(OH)_4^-$ with concentration of C_s). The secondary is assumed to reach immediate equilibrium with primary species and the distribution is described with the equilibrium constants. v_{sp} is the numbers of moles of primary species in the secondary species. With the assumption of chemical equilibrium, only the concentration of primary species needs to be solved by the model, since secondary species are linearly dependent on the primary species. The choice of primary species is, however, not unique, and I usually choose for my appliations the most abundant species in the pH range of interest.

Two mathematical engines, GIMRT and OS3D, were used by CrunchFlow to solve Eq. (1.1) under different flow conditions. GIMRT, uses a global implicit approach and solves the transport and reaction terms simultaneously. It uses a first order accurate upwind scheme for spatial derivative and backward difference for temporal derivative. In contrast, the OS3D engine uses an operator splitting approach, which solves the transport and reaction terms separately. OS3D offers a real benefit when dealing with systems that have a dominant advection component since this engine has better numerical stability (i.e., less numerical dispersion). OS3D is, however, limited by the smaller temporal discretization required in order to achieve additional accuracy, a disadvantage that is more apparent when applying Crunch Flow to near steady-state conditions. Therefore, Steefel (2009) recommends the use of the GIMRT engine when the topic of interest spans geological time scales.

Transport behavior of solid and liquid phases in marine sediments

The two transport processes considered within the scope of my dissertation are diffusion and the burial of solid and fluids. The difference in burial rate of sediment and pore fluid results in a weak Darcy-type advective flow.

Diffusion is formulated following Fick's 2nd law. For a 1-D problem, the following applies:

$$\frac{\partial C}{\partial t} = -D_{eff}\phi\frac{\partial^2 C}{\partial x^2} \quad (1.3)$$

where t and x are time and space, C is the concentration of species of interest, and D_{eff} is the effective diffusion coefficient that is corrected for tortuosity effect following:

$$D_{eff} = \frac{D_{25}}{F} \quad (1.4)$$

where D_{25} is molecular diffusion coefficient in water at 25 ^{o}C (default temperature in CrunchFlow), which can be found in the databases or calculated from Li and Gregory (1974) and Boudreau (1996). F, the formation factor, quantifies tortuosity in porous media. Based on the available information, I either assigned a formation factor value that makes the tortuosity correction independent to porosity, or alternatively a cementation exponent (m), which relates formation factor and porosity as:

$$m = -\frac{\log(F)}{\phi} \quad (1.5)$$

By assigning a cementation exponent, the tortuosity correction will then be porosity-dependent.

Diffusion coefficients at temperature other than 25 ^{o}C are calculated according to:

$$D_T = D_{25}e^{-\frac{Ea}{RT}} \quad (1.6)$$

where *Ea* is activation energy, *R* is ideal gas constant, and *T* is temperature. CrunchFlow uses a default activation energy of 5 kcal/mol; however, the temperature dependency can be changed by assigning a different *Ea* value. When diffusion coefficients for different species are considered, CrunchFlow will include an explicit calculation of electrochemical migration using the Nernst-Planck equation.

Sediment grain and pore water are buried in different rates due to compaction of the solid matrix. Based on the available dating information and assuming steady state compaction, I calculated burial rates of solid and fluid according to Berner (1980):

$$\omega = \frac{1-\phi_z}{1-\phi}\omega_z \quad (1.7)$$

$$\upsilon = \frac{\phi_z}{\phi}\omega_z \quad (1.8)$$

where ω and υ are burial rates of solid and fluid, respectively. ϕ is porosity, ϕ_z and ω_z are porosity and solid burial rate at depth assuming there is no compaction or where porosity does not change with depth.

The relative importance between diffusive and advective flow of water can be assessed by calculating the Péclet number:

$$P_e = \frac{\upsilon L}{D} \quad (1.9)$$

The range of υ considered in this dissertation is 10^{-4} to 10^{-5} m/yr whereas diffusion coefficients (*D*) for all the species considered are in the range of 10^{-1} to 10^{-2} m^2/yr. The length (L) considered ranges from 10^2 to 10^1 meters. The Péclet numbers calculated from this information range from 10^0 to 10^{-3} suggesting that, in most of the cases, diffusion is more important than advection for the dissolved species to transport.

Biogeochemical reactions

The activity coefficients for different solutes are calculated by the extended Debye-Hückel formulation. The five types of reactions considered are: acid-base, gas dissolution, redox, mineral precipitation/dissolution, and ion exchange. Both acid-base and gas dissolution reactions are assumed to happen instantaneously in CrunchFlow. Therefore, the acid-base pairs and gas species are assigned as secondary species. The equilibrium between primary and secondary or gas species is described by the temperature-dependent equilibrium constants from CrunchFlow database. The information in the database is mostly inherited from predecessor models such as PHREEQC (Parkhurst and Appelo, 1999) or EQ3/EQ6 (Wolery, 1992).

Microbial-mediated redox reactions are formulated as Monod-type reactions in CrunchFlow:

$$R_{redox} = k_{\max} \prod_{i=1}^{n} \left(\frac{C_i}{C_i + K_{half-i}} \right) \left(1 - \frac{Q}{K_{eq}} \right) \prod_{j=1}^{m} \left(\frac{K_{in-j} + C_j}{K_{in-j}} \right) \quad (1.10)$$

where k_{max} is the theoretical maximum rate, C_i is the concentration of species involved in the Monod term, K_{half-i} is the half saturation constant, Q is ion activity product, and K_{eq} is equilibrium constant. The last term in Eq. (1.10) is the inhibition term, where K_{in-j} is the inhibition constant and C_j is the concentration of inhibitor. The Monod terms add additional dependency of the limiting species to the overall reaction rate. The overall rate decreases faster when the concentration (i.e., C_i) is lower than the half saturation constant, a dependency that is supported by empirical observations (Monod, 1949). The inhibition terms take a similar but reverse form as the Monod term. With the inhibition term, the overall reaction rate is suppressed until the concentration of inhibitor (i.e., C_j) drops below the level set by the inhibition constant.

To describe formation or decomposition of solids (e.g., minerals and organic matter), two rate expressions are used. One is the *tst*-type, which is formulated as:

$$R_{\min} = A_m k_m \exp[\frac{-Ea}{RT}] \prod a_i^n [1 - \frac{Q}{K_{eq}}] \quad (1.11)$$

where A_m are k_m are the surface area and kinetic constant. Πa_i^n is the activity product of solutes in the reaction with their stoichiometry (n) as exponents. This rate expression applies for most of the minerals. The other type of rate expression applies for microbial-mediated reactions such as organic matter degradation. It has a similar rate expression as Eq. (1.11) but includes Monod and inhibition terms following. k_m in Eq. (1.11) is modified to include Monod term:

$$k_m = \sum_{i=1}^{n} k_{\max} \left(\frac{C_i}{C_i + K_{half-i}} \right) \quad (1.12)$$

and the inhibition term is formulated as:

$$I = \prod_{j=1}^{m} \left(\frac{K_{in-j} + C_j}{K_{in-j}} \right) \quad (1.13)$$

The last reaction type considered is ion exchange, which is the exchange of ions in the aqueous phase with ions adsorbed unto a mineral surface. CrunchFlow quantifies this reaction with an equilibrium constant that describes the partitioning between adsorbed and free ions. This requires knowledge of the concentration of sites on a mineral surface, which can be calculated with knowledge of mineral assemblage in the sediments. Detailed considerations of these reactions for each system studied are provided in the four dissertation chapters.

Brief introduction of the three topics

The first project is focused on understanding the carbon cycling around the sulfate-methane-transition-zone (SMTZ) in the sediments of Ulleung Basin. The complicated interactions among different species and reactions make it almost impossible to resolve without using a transport-reaction model approach. I applied CrunchFlow to better quantify the reactions involved in generation and cycling of methane in environments controlled by purely diffusive fluxes (non-chimney environments) or in environments where methane advection constitutes a significant component (chimney

environments) of the methane budgets. I use pore water compositional and isotopic data collected from eight sites drilled during the second Ulleung Basin gas hydrate drilling expedition (UBGH2) in 2010 to constrain the model. Assessment of processes reveal the very different biogeochemistry between the two environments. Organic matter decomposition is an important process for production of methane, dissolved inorganic carbon (DIC) and consumption of sulfate in the non-chimney sites while anaerobic oxidation of methane (AOM) dominates in both carbon and sulfur cycles of the chimney environment. AOM is mediated by methane from different sources between the two settings. The internally produced methane, through CO_2 reduction (CR) and methanogenesis, fuels AOM in the non-chimney sites while AOM is primarily induced by methane from external sources in the chimney sites. By conducting a simulation of system evolution from a non-chimney to a chimney condition by increasing the bottom methane supply, we showed that the higher CH_4 flux leads to a higher microbial activity of AOM, and more organic matter decomposition through methanogenesis. The higher rate ratios between AOM and CR and methanogenesis rates in the chimney sites are responsible for the isotopically lighter DIC and heavier methane in this environment relative to the non-chimney sites.

With the full description of the biogeochemical reaction network established, I then extend this model to Krishna-Godavari (K-G) Basin on the eastern Indian margin. The pore water profiles of sediments from seven sites cored during the 2006 Indian National Gas Hydrate Project (NGHP-01) expedition show the influence of mass transport deposits (MTDs), which is defined as a fluidilized sediment block whose pore water composition is identical to sea water. The first 10 to 25 meters of pore water profiles at these sites are dominated by the signal from MTDs. Sulfate profiles, especially, show signs of consumption in the first few meters and then maintain constant levels until the depth where methane content starts to increase. By simulating the pore water sulfate and ammonium concentrations, I and co-authors provide a quantitative description of how the MTDs can affect the geochemistry profiles, not only for sulfate and ammonium but potentially all pore water species. Our model provides reliable estimates of the MTDs thickness, the time elapsed after the most recent event, and the organoclastic sulfate reduction rate (RSR) at these seven sites. I also estimated the time required for the system to reach a new steady state after the

MTD events. In addition, the results are highly relevant in that they illustrate the potential mis-interpretations that can arise when using the pore water profiles to infer metabolic processes of sites experiencing significant MTDs. In particular, we question the postulated sulfate-reducing ammonium oxidation pathway by Schrum et al. (2009), based on the low ammonium concentration observed within the first sulfate reduction zone at Site 14A. The model clearly shows that the aforementioned profiles instead reflect a non-steady state condition triggered by MTD in this basin.

In the last project, CrunchFlow is applied to investigate the critical reactions that control silica diagenesis in the incoming sediments to the Nankai Trough. I and the co-authors present a silica reaction network and validate our results against existing pore water and sediment geochemical data at four sites of different sedimentary and thermal conditions, drilled during ODP and IODP expeditions. Our model reproduces a silica diagenetic boundary (SDB) at each site, which is defined by marked decreases in reactive volcanic ash, pore water silica and potassium. Volcanic ash alteration, is estimated by modeling pore water $^{87}Sr/^{86}Sr$ profiles, and the derived reaction rate of $10^{-12.13}$ to $10^{-11.75}$ mol of $Si/m^2/sec$ provides the $SiO_{2(aq)}$ at rates required to form authigenic amorphous silica phase above the SDB. Below the SDB, formation of clinoptilolite consumes potassium and regulates the extension of amorphous silica by consuming $SiO_{2(aq)}$. The observed low $SiO_{2(aq)}$ and dissolved potassium in these deep sequences require continuous precipitation of clinoptilolite; however in order to maintain oversaturation of this mineral at the low $SiO_{2(aq)}$ in sediments below the SDB, an increase in pH is required, consistent with pore water observations. Thermal history, rather than temperature alone, controls the inferred reaction network as shown by the convergence of the thermal maturity of sediments at the SDB from all sites (ΣTTI ranges from 0.0053-0.0124), consistent with other locations documented onshore Japan. Our study results are valuable as we move forward in understanding the mechanisms and consequences of ash alteration in convergent margins worldwide.

CHAPTER 2

Carbon cycling within the sulfate-methane-transition-zone in marine sediments from the Ulleung Basin

Wei-Li Hong, Marta E. Torres, Ji-Hoon Kim, -
Jiyoung Choi, and Jang-Jun Bahk -

BIOGEOCHEMISTRY
115 (1-3) :129-148
DOI: 10.1007/s10533-012-9824-y
Published: OCT 2013

2.1 Abstract

The significance of the various carbon cycling pathways in driving the sharp sulfate methane transition (SMTZ) observed at many locations on continental margins is still a topic of debate. Unraveling these processes is important to our understanding of the carbon cycle in general and to evaluate whether the location of this front can be used to infer present and past methane fluxes from deep reservoirs (*e.g.,* gas hydrate). Here we report the pore water data from the second Ulleung Basin Gas Hydrate Expedition (UBGH2) and on the results of a box model that balances solute fluxes among different carbon pools and satisfies the observed isotopic signatures. Our analysis identifies a secondary methanogenesis pathway within the SMTZ, whereby 25 to 35% of the dissolved inorganic carbon (DIC) produced by the anaerobic oxidation of methane (AOM) is consumed by CO_2 reduction (CR). To balance this DIC consumption, a comparable rate of organic matter degradation becomes necessary, which in turn consumes a significant amount of sulfate. The fraction of sulfate consumed by AOM ranges from 70 to 90%. Whereas a simple mass balance would suggest a one to one relationship between sulfate and methane fluxes; our isotopic considerations show that methane flux estimates based solely on sulfate data may be in error by as much as 30%. Furthermore, the carbon cycling within the SMTZ is fueled by a significant contribution (10-40%) of methane produced by organic matter degradation just below the SMTZ. Therefore AOM rates cannot necessarily be used to infer methane contributions from gas hydrate reservoirs that may lay tens to hundreds of meters below the SMTZ.

2.2 Introduction

The sulfate methane transition zone (SMTZ) along continental margins, where sulfate is almost depleted and methane concentration starts to dramatically increase (Figure 1), is usually no deeper than a few to tens of meters. We have a good first order understanding of the reactions driving this front; however, the various carbon cycle pathways involved, and the relative fraction of sulfate consumed by these reactions is still being debated. Using data from sediment cores taken off Namibia and assuming there was no organoclastic sulfate reduction at the sediment surface, Niewöhner et al. (1998) suggested that the sulfate flux in this region can be fully explained by anaerobic oxidation of methane (AOM). On the other hand, down-core sulfate reduction rate measurements were used by Fossing et al. (2000) to demonstrate that more than 60% of the sulfate reduction can occur within the first meter of the sediments due to fast organic matter degradation. For the Black Sea, Jørgensen et al. (2001) showed that sulfate profile remained unaffected by organoclastic sulfate reduction because in this area sulfate diffuses rapidly into surface sediments, whereas sulfate is replenished only very slowly at the SMTZ depth. These data suggest that in diffusive systems, sulfate profiles may be fully dictated by AOM and not by organoclastic sulfate reduction, even if there was a significant component of organoclastic sulfate reduction in the shallowest sediments.

These results are significant because, if the depth of the SMTZ were to scale inversely with the strength of an upward diffusive methane flux, sulfate can be used as a proxy for the methane supply from the gas hydrate reservoirs, as postulated by several investigators (Borowski et al., 1996, 1999; Niewöhner et al., 1998; Dickens, 2001; Lin et al., 2006; Yang et al., 2008; Chuang et al., 2006, 2010). However, such inference is based on two simplified assumptions: 1) sulfate is dominantly consumed by methane through AOM and 2) all the methane consumed by AOM comes from gas hydrate dissociation. The first assumption may be undermined if there is a significant contribution of sulfate reduction fueled by organic matter degradation above or within the SMTZ. The second assumption may also be problematic, since a zone of methane generation by microbial activity has been shown to occur just below the SMTZ (Oremland et al., 1982; Claypool et al., 2006; Colwell et al., 2008). To account for

this shallow zone of methane generation, we incorporate it into our model, and designate our box as an expanded sulfate methane transition zone (ESMTZ) (Figure 2-1). The upper boundary of this box is demarked by the sharp transition in the sulfate and methane profiles, and the lower boundary is conceptually defined to include the methanogenesis zone just below the depth where sulfate is exhausted.

Here we report on pore water profiles for the upper 30 m at five sites drilled in the Ulleung Basin offshore Korea, and present a complete mass balance approach that includes concentrations, isotopes and fluxes of various metabolites from SMTZ or ESMTZ (Figure 2-1). Our primary conclusion is that, while AOM may consume much of the sulfate in this basin, other pathways that modify the DIC concentration – namely, reduction of POC, and shallow methanogenesis- are important, and need to be quantified. We argue that the methane produced locally by converting DIC from AOM into methane (secondary methanogenesis) and from organic carbon diagenesis immediately below SMTZ need to be considered in order to achieve a carbon isotopic mass balance across the SMTZ. These shallow methane sources, both distinct in the isotopic composition of the substrate, need to be considered to fully characterize carbon cycle budgets and in the assessment of methane contribution from gas hydrate reservoirs based on sulfate gradients.

2.3 Study area and sediment properties

The Ulleung Basin, one of the three main basins in the East Sea, is bounded by the steep continental slope of the Korean Peninsula to the west and the Korean Plateau to the north (Figure 2-2A). This area harbors a thick (4 km) sediment section characterized by extensive turbidite and mass transport deposits, with moderate total organic matter content (~1-4%, Kim et al., 2007 and Table 2-1). Gas hydrates have been recovered from this margin, and hydrocarbon analyses point to a biogenic source for the methane in these deposits (Bahk et al., 2009; Chun et al., 2011; Kim et al., 2011, 2012).

Here we focus on five sites (UBGH2-1_1, 2-2_1, 2-5, 2-6, and 2-10) drilled during the second Ulleung Basin Gas Hydrate Expedition (UBGH2) in 2010 (Figure 2-2B). The depth penetrated by these sites ranges from 230 to 360 meters below seafloor

(mbsf). The depth of bottom simulating reflector (BSR), depth of gas hydrate first appearance, and average content of particulate organic carbon (POC) content, have been reported by the UBGH2 Scientists (2010), and are included in Table 2-1. The depth of the BSR is shallower than 190 meters at all sites. Gas hydrate in these sites was first observed at 71 to 153 mbsf. POC content ranges from less than 0.1% to 4%, with an average of ~1.5%.

Onboard porosity measurements at these sites show that they follow the classic equation for depth-dependent porosity (Boudreau, 1997):

$$\phi(z) = \phi_f + (\phi_0 - \phi_f)\exp(\gamma z) \quad (2.1)$$

where ϕ_f and ϕ_0 are porosity at great depth and at the water-sediment interface, respectively. γ is an empirical constant, which can be obtained from data fitting and z is the depth in the sediments. The measured porosity (UBGH2 Scientists, 2010) and trends used to fit those measurements are shown in Figure 2-3. Parameters used to fit the observations according to Eq.(2.1) are listed in Table 2-2. These fitted trends will be used for porosity estimation in our box model.

2.4 Analytical method and results

2.4.1 Sample collection

Pore water, gas, gas hydrate and sediment samples were collected from all the drilled sites following the protocols detailed in UBGH2 Scientists (2010). Pore water was extracted from whole round sediment samples (5-20 cm length) collected immediately after retrieval of the cores. Following extrusion from the core liner, the surface of the sediment sample was carefully scraped with a clean spatula or clean ceramic knife to avoid any contamination with drilling fluid (ambient surface seawater). Pore water was extracted from the clean sediments using titanium squeezer, modified after the stainless steel squeezer of Manheim and Sayles (1974), and a laboratory Carver hydraulic press (< 20 MPa). Pore water was filtered through a Whatman paper and a 0.20 μm disposable polytetrafluoroethylene in-line filter, and collected in HCl

prewashed syringes. Aliquots were transferred into HCl prewashed high density polyethylene vials for shipboard analyses of major and minor ions. Subsamples for isotopic analyses of the dissolved inorganic carbon (DIC) were collected in 2 ml septum screw-lid glass vials and preserved with $HgCl_2$.

Void gases in the core were sampled by piercing the liner and allowing gas to expand into a 60 ml syringe connected to the penetration tool. The gas sample was then transferred to a 50 ml serum glass vial which was pre-filled with saturated NaCl solution. For headspace gas analyses, a 3 ml sediment sample was taken with a 5 ml cut-off plastic syringe from the freshly exposed end of each core section, and extruded into a 30 ml serum glass vial. Following the method described in Riedel et al. (2006), 2 ml of saturated NaCl was added to each vial, which was then sealed with a 10 mm-thick septum and a metal crimp cap to preserve the samples.

2.4.2 Analytical approaches

Sulfate and alkalinity were measured onboard. The first 5 ml of pore water was immediately subsampled for pH and alkalinity determinations using a pH electrode and a Gran titration with a Metrohm autotitrator. The precision of the alkalinity titrations was monitored by repeated analysis of International Association for the Physical Sciences of the Ocean (IAPSO) standard seawater, and was less than 2%. Sulfate was analyzed by ion chromatography (Dionex ICS-2100 IC) using 0.2 ml samples diluted with 5.8 ml of Milli-Q water. At the beginning and the end of each run, several different dilutions of IAPSO standard seawater were analyzed as a quality control and to determine accuracy. IAPSO standard seawater was analyzed after every seven samples as a check for instrumental drift and to calculate analytical precision. Precision for the sulfate analyses was better than 0.8%, and average accuracy was better than 1.5%.

Immediately after samples were collected, concentration of methane, ethane, propane, and CO_2 in the head space and void gas samples were measured onboard by gas chromatography (GC; Agilent 3000A Micro GC) with a thermal conductivity detector (TCD) and two independent columns: PLOT-U (8 m long and 0.32 mm inner

diameter) for C_1-C_4 hydrocarbons and MolSieve 5A Plot (10 m long and 0.32 mm inner diameter) for O_2, N_2, CO_2 and CO. The temperature of the injector and the Plot-U column is stabilized at 90 ^oC while the temperature for the MolSieve 5A Plot is 105 ^oC. Helium is chosen as carrier gas and column flow rate is 2.2 ml/min. The accuracy of CH_4 and CO_2 analysis, determined by repeated measurements of 1% standard gas, is better than 4 % and 6%, respectively. Since both headspace gas and void gas samples suffered from severe degassing during core recovery, it is impossible to precisely determine the in-situ gas concentration.

The isotopic composition of DIC in pore water was analyzed with a Finnigan DELTA-Plus mass spectrometer using a Gas-Bench II automated sampler at Oregon State University, as described in Torres et al. (2005). The precision and accuracy are better than ±0.15‰ and ±0.07‰, respectively, based on the multiple standard measurements. The stable carbon isotope of methane ($\delta^{13}C_{CH4}$) was measured using an isotope ratio-monitoring gas chromatography/mass spectrometer in Isotech, Champaign, IL. The reproducibility was ±0.1‰. The stable carbon isotope values for DIC and methane are reported in the conventional δ notation in permil (‰) relative to V-PDB.

2.4.3 Analytical results

The concentration profiles of the parameters required for our box model are illustrated in Figure 2-4 and listed in Table 2-3. Data and the detailed calculations can be found in the supplementary material online. The depth of the SMTZ was defined by the sulfate and methane profiles at each site. Since this study only examines the carbon cycling around the depth of the SMTZ, we only show data for the upper 30 mbsf. We did not differentiate among the various dissolved carbonate species (bicarbonate, carbonate, and $CO_{2(g)}$) but treat them as a single DIC (dissolved inorganic carbon) pool. Alkalinity can reasonably represent DIC concentration within the pH range of our samples (7.3-7.8). Therefore, alkalinity is used as synonymous with DIC throughout this paper. The alkalinity and calcium profiles show a distinct change in their concentration gradient across the depth of the SMTZ, indicating that the bicarbonate produced by AOM increases alkalinity and consumes calcium through

authigenic carbonate precipitation. Abnormally high alkalinity around the SMTZ was explained by Kim et al. (2011) as an indication of DIC leaking from a deep methanogenesis zone; this observation suggests that organic matter degradation by methanogenesis is an important component of the carbon cycling in the Ulleung Basin. The carbon isotopic profiles of methane and DIC, display minimum values around the SMTZ, reflecting the carbon pathways between the methane and DIC pools through AOM and CR, as previously suggested by Borowski et al. (1997) for Blake Ridge sediments.

2.5 Box model framework

We constructed a model that encompasses the SMTZ and the methanogenesis zone immediately below the depth of sulfate depletion; in a zone we designate ESMTZ. It includes 2 solid phases (organic matter and authigenic carbonate) and 3 dissolved components (sulfate, methane, and alkalinity) (Figure 2-5). All symbols used are listed in the Appendix 1. For the three dissolved components in Figure 2-5, we constructed a mass balance between input and output rates and fluxes, which includes transport (grey arrows) and reaction terms (red, orange, blue, purple, and green arrows). All components are linked via five reactions with a different degree of isotopic fractionation, which is parameterized as:

$$\alpha = \frac{r_r}{r_p} \quad (2.2)$$

where r_r and r_p are the isotopic ratios ($^{13}C/^{12}C$) of the reactant and product.

The five reactions under consideration are:

POC sulfate reduction (POCSR):

$$CH_2O + \frac{1}{2}SO_4^{-2} \rightarrow \frac{1}{2}H_2S + HCO_3^- \quad \delta^{13}C_{CH2O}\text{=-23‰}, \ \alpha_{POCSR} \cong 1 \quad (2.3)$$

Calcium carbonate precipitation (CP):

$$Ca^{+2} + CO_3^{-2} \rightarrow CaCO_3 \quad \delta^{13}C_{DIC}\text{=varies}, \ \alpha_{CP} \cong 1 \quad (2.4)$$

Anaerobic oxidation of methane (AOM):

$$CH_4 + SO_4^{-2} \rightarrow HS^- + HCO_3^- \quad \delta^{13}C_{CH4}=\text{varies},\ 1.004 < \alpha_{AOM} < 1.03 \quad (2.5)$$

Secondary methanogenesis or CO_2 reduction (CR)

$$CO_2 + 4H_2 \rightarrow CH_4 + 2H_2O \quad \delta^{13}C_{DIC},\ ^{13}C_{CH4}=\text{varies},\ 1.01 < \alpha_{CR} < 1.095 \quad (2.6)$$

Methanogenesis (ME)

$$CH_2O \rightarrow \frac{1}{2}CH_4 + \frac{1}{2}CO_2 \quad \delta^{13}C_{DIC},\ ^{13}C_{CH4}=\text{varies},\ \delta^{13}C_{CH2O}=-23‰,$$

$$1.01 < \alpha_{ME} < 1.095 \quad (2.7)$$

The isotopic fractionation factors listed here are from Whiticar (1999). Organic matter degradation via sulfate (POCSR, Eq. (3)) usually occurs well above the SMTZ (e.g., in the first tens centimeters below sediment-water interface as shown in Fossing et al. (2000)). Although POCSR does not occur within the SMTZ, it consumes a portion of sulfate supply from the seafloor and, therefore, decreases the flux of sulfate into the SMTZ. POCSR is thus expressed as the portion of sulfate flux that does not enter the SMTZ in our box model. AOM (Eq. (5)) that consumes both sulfate and methane in the SMTZ produces DIC and induces precipitation of calcium carbonate (Eq. (4)), which consumes most of the calcium flux from seafloor.

The first three reactions discussed above (Eqs. (3) to (5)) has been well accepted among literature (*e.g.,* Kim et al., 2007 and Chatterjee et al., 2011). However, Eqs. (2.6) and (2.7) are typically not considered in carbon cycling studies around the SMTZ, even though there are several studies showing that the rate of microbial methanogenesis peaks immediately below the SMTZ (*e.g.,* Oremland et al., 1982; Claypool et al., 2006; Colwell et al., 2008). Secondary methanogenesis or CR, is specified in our model as the reaction utilizes CO_2 produced from AOM. For methanogenesis (ME), the primary substrate is organic carbon. Whereas this metabolic process involves several steps (*e.g.*, production of CO_2 and hydrogen gas; and carbonate reduction to methane), for the purpose of the model it is described by reaction (7). These two reactions that generate methane (CR and ME) are defined in terms of their carbon sources: the DIC produced by ME comes directly from organic

matter decomposition while the DIC utilized by CR is produced by AOM and it is not directly linked to organic matter degradation.

Within the ESMTZ (defined to include the zone of methanogenesis below the SMTZ, Figure 2-1), the following three equations are used to describe the mass balance for sulfate, DIC, and methane:

$$F_{SO4.in}=F_{SO4.out}+R_{POCSR\text{-}S}+R_{AOM} \quad (2.8)$$

$$F_{DIC.in}+R_{ME\text{-}DIC}+R_{POCSR\text{-}C}+R_{AOM}=F_{DIC.out}+R_{CR}+R_{CP} \quad (2.9)$$

$$F_{CH4.in}+R_{CR}+R_{ME\text{-}CH4}=F_{CH4.out}+R_{AOM} \quad (2.10)$$

where "F" denotes flux, "R" denotes reaction rate, and *in* and *out* indicate the flux direction relative to the ESMTZ. $R_{POCSR\text{-}S}$ and $R_{POCSR\text{-}C}$ are the rates of sulfate consumption and DIC production through POCSR. They relate to each other according to the stoichiometry in Eq. (2.3) (*i.e.*, $R_{POCSR\text{-}C}=2\times R_{POCSR\text{-}S}$). $R_{ME\text{-}DIC}$ and $R_{ME\text{-}CH4}$ are rates of ME in terms of DIC and methane production. Both of these rates are half of the ME rate (*i.e.*, $R_{ME}=2\times R_{ME\text{-}DIC}=2\times R_{ME\text{-}CH4}$) followed the stoichiometry in Eq. (2.7). These fluxes and rate terms are illustrated in Figure 2-4 and 2-5. In our following calculations and discussion, we assume that both sulfate and methane are fully consumed within the ESMTZ, so that the values for $F_{SO4.out}$ and $F_{CH4.out}$ are negligible and can be ignored in Eq.(2.8) and (2.10). $F_{CH4.in}$ denotes the flux of methane that comes from outside the box (Figure 2-1) and carries a distinct isotopic signature that is not related to any reaction considered in our model frame.

2.5.1 Transport terms

This study focuses on sites with diffusion-dominated concentration profiles (Figure 2-4), and where no sign of advective flow was observed emerging from seafloor or in geophysical surveys (UBGH2 Scientists, 2010). By assuming a diffusion-dominated system under steady state, we can quantify the magnitude of the fluxes F_{in} and F_{out} with Fick's law:

$$F = -D\frac{\Delta(\phi C)}{\Delta z} \quad (2.11)$$

Porosity information is given in Figure 2-3 and Table 2-2. Tortuosity-corrected diffusion coefficients (D) for sulfate, calcium, and DIC are derived from the relationships in Boudreau (1997) assuming a constant temperature in the sediments of 4°C. The concentration gradients ($\frac{\Delta(\phi C)}{\Delta z}$) are calculated from individual profiles and are used to calculate F_{in} and F_{out}. Since most of the gradients in our sites are linear, we apply a simple 1st order linear regression to calculate each gradient (Table 2-3).

To satisfy isotopic mass balance considerations, it is necessary to calculate the transport of both the heavy and light carbon (*i.e.,* ^{13}C and ^{12}C) by CH_4 and DIC. In combination with measured isotopic ratios, this information is used to infer the concentration profiles for $^{12}C_{DIC}$ and $^{13}C_{DIC}$ as follows:

$$^{12}C_{DIC} = \frac{C_T}{(1 + r_{DIC})} \quad (2.12)$$
$$^{13}C_{DIC} = C_T - {}^{12}C_{DIC}$$

where C_T is the total concentration (*i.e.,* alkalinity in Figure 2-4) and r_{DIC} is the concentration ratio of heavy to light carbon ($^{13}C/^{12}C$) from its isotopic value:

$$r_{DIC} = (\frac{\delta^{13}C_{DIC}}{1000} + 1) \times r_{std} \quad (2.13)$$

where r_{std} is the ratio for V-PDB standard (0.0112372).

A migration-induced isotopic fractionation is related to the mass ratio of the two isotopes (Zeebe and Wolf-Gladrow, 2001). However, since such fractionation is much smaller than the fractionation from other reactions (diffusion coefficients of $^{13}CO_2$ is

only 0.7-0.87 ‰ smaller than it for $^{12}CO_2$; O'Leary, 1984 and Jähne and Dietrich, 1987), we have neglected it in our calculation.

2.5.2 Reaction terms

The isotopic fractionation for each of the five reactions considered here (Eqs. (2.3) to (2.7)), is fundamental to our understanding of processes occurring within the SMTZ. The isotopic effect (α) for a steady-state one-step reaction may be expressed in terms of the rate constant of the heavy (k^H) and light (k^L) isotopes (Rees, 1973):

$$\alpha = \frac{k^L}{k^H} \quad (2.14)$$

From Eqs. (2.2) and (2.14), we can then formulate the reaction rates for all light and heavy isotopes. For *light* carbon (*i.e.,* ^{12}C), reactions are formulated as follow:

$$^{12}R_{POCSR\text{-}S} = \phi\left(\frac{1}{2} f R_{OM}\right) \quad (2.15)$$

$$^{12}R_{POCSR\text{-}C} = \phi\left(f R_{OM}\right) \quad (2.16)$$

$$^{12}R_{ME\text{-}DIC} = \phi(1-f)\frac{1}{2} R_{OM} \quad (2.17)$$

$$^{12}R_{ME\text{-}CH4} = \phi(1-f)\frac{1}{2} R_{OM} \quad (2.18)$$

$$^{12}R_{AOM} = F_{SO4.in} - \phi\frac{1}{2} f R_{OM} \quad (2.19)$$

$$^{12}R_{CP} = F_{Ca} \quad (2.20)$$

$$^{12}R_{CR} = b\,^{12}R_{AOM} \quad (2.21)$$

where R_{OM} is the rate of organic matter degradation through both POCSR and ME (*i.e.,* $R_{OM}=R_{ME}+R_{POCSR\text{-}C}$), f is the fraction of organic matter being utilized by POCSR. Stoichiometric considerations are included by the 0.5 multiplier in Eq. (2.15) (*i.e.,*

every mole of organic matter consumed by sulfate is equivalent to 0.5 moles of sulfate) and the 0.5 multiplier in Eq. (2.17) and (2.18) (*i.e.,* every mole of organic matter consumed by methanogenesis produces 0.5 moles each of DIC and CH_4). To describe the production of methane through CR from the pool of DIC generated by AOM (Borowski et al., 1997), we assume the rate of CR is proportional to AOM rate within the SMTZ (Eq. (2.21)). Based on this definition, *b* in Eq. (2.21) must range from 0 to 1.

For the *heavy* carbon (*i.e.,* ^{13}C), we apply the following reaction rate expressions

$$^{13}R_{POCSR\text{-}C} = \phi(fR_{OM})r_{OM} \quad (2.22)$$

$$^{13}R_{ME\text{-}DIC} = \phi(1-f)\frac{1}{2}R_{OM}r_{DIC-bot} \quad (2.23)$$

$$^{13}R_{ME\text{-}CH4} = \phi(1-f)\frac{1}{2}R_{OM}r_{CH4-bot} \quad (2.24)$$

$$^{13}R_{AOM} = (F_{SO4.in} - \phi\frac{1}{2}fR_{OM})\frac{r_{CH_4-SMTZ}}{\alpha_{AOM}} \quad (2.25)$$

$$^{13}R_{CP} = F_{Ca} \times r_{DIC-SMTZ} \quad (2.26)$$

$$^{13}R_{CR} = b^{13}R_{AOM} \times \frac{1}{\alpha_{CR}} \quad (2.27)$$

where *r* is the ^{13}C to ^{12}C ratio of organic matter (r_{OM}), DIC, and CH_4 at the *SMTZ* (r_{CH_4-SMTZ} and $r_{DIC-SMTZ}$) or bottom of the core (r_{CH_4-bot} and $r_{DIC-bot}$) which can be calculated from the isotopic signature listed in Table 2-3. α_{AOM} is the fractionation factor of AOM, which we will calculate from the box model. α_{CR} is the isotopic fractionation of CR and ME. This value is estimated from the isotopic signature of DIC and CH_4 at the core bottom ($\alpha_{CR}=1+(\delta^{13}C_{DIC\text{-}bot}-\delta^{13}C_{CH4\text{-}bot})\times 1000$) for each site (Table 2-3). Detail calculation of the box model can be found from the supplementary material.

2.5.3 Assessment of the error associated with flux estimates

In our box model, reaction rates are always linked to the flux of dissolved species. Therefore, to estimate the errors in our model, we need to quantify the potential errors from our flux estimates; which fall within two general categories. The first include uncertainties associated with parameters such as porosity and tortuosity, which will have the same degree of influence on all fluxes at a given site. This type of error will only affect the absolute but not the relative magnitude of the fluxes, and since most of our discussion relies on the relative magnitude of the fluxes, these uncertainties do not directly impact our discussion.

The second type of error, which arises during the calculation of gradient from each of the chemical species, will affect both the absolute and relative magnitude of the fluxes and hence directly affect our conclusions. The error on our flux estimates is the sum of the error associated with fitting the concentration and isotopic profiles to the data, plus the standard error of the regression slope. Fitting of concentration profiles for sulfate and calcium fluxes is not necessary, thus for these species the error of the flux estimates arises solely from the standard error of regression line, and is usually smaller than 5% (Table 2-4). Fitting of the concentration and isotopic profiles of DIC based on insufficient data, is responsible for most of the error associated with the DIC flux estimates, which range from 6.2 to 20.3% while, in most cases, around 10 to 15%. The error of flux estimation may potentially increase the uncertainties of our rate estimation. Errors of different fluxes at different sites are summarized in Table 2-4. Detailed calculation of the errors is given in the supplementary material.

2.6 Model evaluation

To best illustrate the relative significance of each reaction involving carbon cycling at the ESMTZ, we run our box model on 4 different scenarios, as described below.

Case1: Anaerobic oxidation of methane (AOM) as the only reaction

In this first scenario (Figure 2-5A), we assumed that AOM is the *ONLY* reaction responsible for sulfate consumption and all methane for AOM is supported by upward diffusion of methane from below the SMTZ (*i.e.,* no reactions generate methane

within the SMTZ). Eq. (2.9) is modified and applied to both carbon isotopes, such that the relevant fluxes are estimated by:

$$F_{SO4.in}=R_{AOM} \quad (2.28)$$

$$^{12}F_{DIC.in}+^{12}R_{AOM}=^{12}F_{DIC.out}+^{12}R_{CP} \quad (2.29)$$

$$^{13}F_{DIC.in}+^{13}R_{AOM}=^{13}F_{DIC.out}+^{13}R_{CP} \quad (2.30)$$

and Eq. (2.19) and (2.25) are modified to fit our assumption that sulfate is fully consumed by AOM:

$$^{12}R_{AOM}=F_{SO4.in} \quad (2.31)$$

$$^{13}R_{AOM}=F_{SO4.in}\times\frac{r_{CH_4-SMTZ}}{\alpha_{AOM}} \quad (2.32)$$

Eqs. (2.31) and (2.32) can be plugged into Eqs. (2.29) and (2.30), respectively. The α_{AOM} is the only remaining unknown in this set of equations. Using this approach and the data available for Site UBGH2-1_1, the α_{AOM} generated from this assumption is 0.934. Similar values for $\alpha<1$ were obtained for all sites (Figure 2-6). Both experimental and field data have shown that α_{AOM} is always slightly larger than 1 and ranges from 1.004 to 1.030 (Whiticar, 1999) due to the preferential utilization of light carbon during this microbial-mediated reaction. The results of our Case 1 scenario demonstrate that AOM alone is not sufficient to explain the isotopic composition of DIC and methane observed at the SMTZ.

Snyder et al. (2007) and Wehrmann et al. (2011) performed a similar calculation but did not include carbon isotopic considerations. Since they can fully satisfy Eq. (29) by their approaches, these authors concluded that AOM is the dominant reaction consuming sulfate. However, by including an isotopic mass balance we show the need to include other reactions, and argue that only balancing the fluxes of the total carbon

does not provide sufficient evidence to conclude that AOM is the only reaction that needs consideration.

Case2: Anaerobic oxidation of methane (AOM) and particulate organic carbon sulfate reduction (POCSR)

Here our box model is formulated as:

$$F_{SO4.in}=R_{POCSR-S}+R_{AOM} \quad (2.33)$$

$$^{12}F_{DIC.in}+^{12}R_{POCSR-C}+^{12}R_{AOM}=^{12}F_{DIC.out}+^{12}R_{CP} \quad (2.34)$$

$$^{13}F_{DIC.in}+^{13}R_{POCSR-C}+^{13}R_{AOM}=^{13}F_{DIC.out}+^{13}R_{CP} \quad (2.35)$$

In this scenario (Figure 2-5B), organic matter is allowed to react with sulfate only (*i.e.,* f=1). $^{12}R_{POCSR-C}$ and $^{12}R_{AOM}$ can be solved from Eqs. (2.33) and (2.34) (assuming $^{12}R_{POCSR-C}=2\times R_{POCSR-S}$ and $^{12}R_{AOM}=R_{AOM}$). By plugging Eqs. (2.22) and (2.25) into Eq. (2.35), we can then estimate the isotopic fractionation for AOM (α_{AOM}), which yields a value of 0.941 for Site UBGH2-1_1 (and similar values for other sites). Although this value is slightly larger than that by Case 1, it is still notably smaller than 1, demonstrating that the isotopic mass balance is not satisfied under the Case 2 scenario (Figure 2-6). The small α_{AOM} from Case 1 and 2 suggests that consumption of isotopically light DIC is required to fulfill the mass balance. Such sign suggests consumption of DIC through CR and leads us to the next case.

Case3: Anaerobic oxidation of methane (AOM), particulate organic carbon sulfate reduction (POCSR) and secondary methanogenesis by CO_2 reduction (CR).

By including in our methane sources the recycling of the DIC generated by AOM via CO_2 reduction (CR in Figure 2-5C), we now expand the conventional SMTZ to include the region of methanogenesis in our ESMTZ and have 4 unknowns: R_{OM}, R_{AOM}, $^{12}R_{CR,}$ and the fractionation factors of AOM (α_{AOM}). In order to uniquely solve this set of equations, we need another constraint, which comes from the mass balance equations for methane. The equation set becomes:

$$F_{SO4.in}=R_{POCSR\text{-}S}+R_{AOM} \quad (2.36)$$

$$^{12}F_{DIC.in}+^{12}R_{POCSR\text{-}C}+^{12}R_{AOM}=^{12}F_{DIC.out}+^{12}R_{CR}+^{12}R_{CP} \quad (2.37)$$

$$^{13}F_{DIC.in}+^{13}R_{POCSR\text{-}C}+^{13}R_{AOM}=^{13}F_{DIC.out}+^{13}R_{CR}+^{13}R_{CP} \quad (2.38)$$

$$^{12}F_{CH4.in}+^{12}R_{CR}=^{12}R_{AOM} \quad (2.39)$$

$$^{13}F_{CH4.in}+^{13}R_{CR}=^{13}R_{AOM} \quad (2.40)$$

Since more than 90% of the in situ methane is lost during core recovery (Wallace et al., 2000), it is very unlikely to accurately determine methane flux (*i.e.,* $^{12}F_{CH4.in}$ and $^{13}F_{CH4.in}$). A slightly different in the degree of degassing would result in huge difference in flux estimation from headspace methane concentration gradient. Besides, the depth of gas hydrate first appearance is also adapted by some studies, such as Malinverno and Pohlman (2011), to be the constraint of methane flux since such depth should theoretically correspond to where dissolved methane concentration exceeds its solubility. However, as Torres et al. (2008) pointed out, the distribution of gas hydrate is also highly dependent on lithology. Such lithology-dependent control on gas hydrate distribution was observed in Ulleung Basin (UBGH2 scientists, 2010). Therefore, it may not be a proper approach. Alternatively, we constrain methane flux from its isotopic signature in order to solve another unknown in our equations. We consider this as a better approach since we focus here the isotopic signature of methane entering our model frame.

If we assume that methane concentration within the SMTZ ($^{13}C_{CH4\text{-}SMTZ}$ and $^{12}C_{CH4\text{-}SMTZ}$) is much lower than the methane at depth ($^{13}C_{CH4\text{-}bot}$ and $^{12}C_{CH4\text{-}bot}$) (Figure 2-1), we are able to relate the flux ratio of methane ($\frac{^{13}F_{CH_4.in}}{^{12}F_{CH_4.in}}$) to the concentration ratio of heavy to light methane carbon at the depth where $\delta^{13}C_{CH4}$ approaches a fixed value ($^{12/13}C_{CH4.bot}$ in Figure 2-1). This assumption allows us to combine Eqs. (2.39) and (2.40) in the following way:

$$\frac{^{13}F_{CH_4.in}}{^{12}F_{CH_4.in}} = \frac{\frac{^{13}C_{CH_4-bot} - ^{13}C_{CH_4-SMTZ}}{L}}{\frac{^{12}C_{CH_4-bot} - ^{12}C_{CH_4-SMTZ}}{L}} \cong \frac{^{13}C_{CH_4-bot}}{^{12}C_{CH_4-bot}} = r_{CH_4-bot} = \frac{^{13}R_{AOM} - ^{13}R_{CR}}{^{12}R_{AOM} - ^{12}R_{CR}} \quad (2.41)$$

where L is the depth between $C_{CH4\text{-}SMTZ}$ and $C_{CH4\text{-}bot}$ (Figure 2-1). From Eqs. (2.36), (2.37), (2.38), and (2.41), we can uniquely solve for the 4 unknowns (R_{OM}, $R_{AOM,}$ b, and α_{AOM}). Except for Site UBGH2-10, the resulting value for α_{AOM} estimated with this approach (Figure 2-6) is higher than 1.03, which is out of the possible range suggested by Whiticar (1999). The unreasonably large α_{AOM} for most sites suggests, under the assumption in Case 3, more isotopically light DIC has to be produced in order to satisfy the mass balance. ME, which produces isotopically heavier DIC than the signature at SMTZ, may not be a suitable reaction at first glance. However, ME also produces isotopically light CH_4 which will be consumed and formed isotopically light DIC through AOM. Therefore, it is still logical to include this reaction.

Case 4: Anaerobic oxidation of methane (AOM), particulate organic carbon sulfate reduction (POCSR), secondary methanogenesis by CO_2 reduction (CR) and methane generation from organic carbon (ME)

We thus include ME in the box mode (Figure 2-5D). Since we must account for a fraction of organic matter being converted to methane (Eq. (2.7)), the fraction of organic matter that is consumed by sulfate reduction (*f* values in Eqs. (2.15) and (2.17)) is no longer 1 as in Case 1 to 3, but a number smaller than 1. The equation set for this case can be expressed as (Figure 2-5D):

$$F_{SO4.in} = R_{POCSR\text{-}S} + R_{AOM} \quad (2.42)$$

$$^{12}F_{DIC.in} + ^{12}R_{POCSR\text{-}C} + ^{12}R_{AOM} + ^{12}R_{ME\text{-}DIC} = ^{12}F_{DIC.out} + ^{12}R_{CR} + ^{12}R_{CP} \quad (2.43)$$

$$^{13}F_{DIC.in} + ^{13}R_{POCSR\text{-}C} + ^{13}R_{AOM} + ^{13}R_{ME\text{-}DIC} = ^{13}F_{DIC.out} + ^{13}R_{CR} + ^{13}R_{CP} \quad (2.44)$$

$$\frac{^{13}F_{CH_4.in}}{^{12}F_{CH_4.in}} \cong \frac{^{13}C_{CH_4-bot}}{^{12}C_{CH_4-bot}} = \frac{^{13}R_{AOM} - ^{13}R_{CR} - ^{13}R_{ME-CH_4}}{^{12}R_{AOM} - ^{12}R_{CR} - ^{12}R_{ME-CH_4}} \quad (2.45)$$

In addition to the 4 unknowns detailed in Case 3, we now have one more unknown, *f*. Therefore, we are not able to uniquely constrain the system with the available data. Nonetheless, we are able to evaluate the equation sets by varying *f* from 0 to 1 to determine the ranges of *f* for which α_{AOM} falls within a reasonable range, as illustrated by the data that lie within the dash lines in Figure 2-7A. We also calculated the possible fraction of DIC from AOM that is recycled through CR (*i.e., b*), as shown in Figure 2-7B.

Our results suggest that:

1) In order to satisfy the isotopic mass balance (as inferred by agreement with α_{AOM} values from the literature), a significant fraction (>50% in 4 of the studied sites as the *f* is smaller than 0.5 in Figure 2-7A for these sites) of the organic matter is metabolized via methanogenesis (ME) rather than via sulfate reduction POCSR. Only at Site UBGH2-10 can we achieve isotopic compliance without ME; and

2) ME alone is not able to satisfy the isotopic mass balance, but in all cases a significant fraction (28 to 45%) of the DIC produced from AOM (*b* in Figure 2-7B) has to be recycled to methane by CR. This, however, is not what Chatterjee et al. (2011) concluded from their kinetic model that aims at achieving a mass balance with a full consideration of methane and DIC isotopic signatures. Our approach differs in that we specifically separate CR from ME in order to describe the cycling of carbon between methane and DIC pools, which influence the model results and hence leads to different interpretations. Although Chatterjee et al. (2011) also included isotopic signature of methane into their model, they did not track its change. Therefore, we are not able to verify the mass balance of their model based on the results presented.

2.7 Discussion

2.7.1 Carbon cycling around the SMTZ in Ulleung Basin

The relative contribution of the 5 individual reactions considered in ESMTZ to the overall DIC pool, has been estimated as the ratio of the reaction rates to the net DIC flux ($\Delta F_{DIC} = F_{DIC.in} - F_{DIC.out}$). The results at each of the study sites are depicted in Figure 2-8, and Table 2-5 summarizes the depth-integrated rates for each reaction. Except for Site UBGH2-10, the contribution of each reaction to DIC production is

AOM>ME>POCSR. It is also apparent from these results that a fraction of the DIC produced by AOM is consumed by CR within the ESMTZ. To balance this DIC consumption, a similar rate of organic matter degradation becomes necessary, and as shown in Figure 2-8, the overall POCSR may be responsible for utilizing up to 30% of the total sulfate input from seafloor.

We conducted a series of correlation tests between the site-specific parameters (Table 2-1) and the model inputs (Table 2-3) and outputs (Table 2-5). Although correlation can not be used to infer consequential relationships, it is informative to identify the connected parameters. The results of this correlation test could be found in the supplementary material. It is interesting to note that the depth of the SMTZ depth is, as expected, inversely correlated with the sulfate flux (r^2=0.89) and with DIC flux above the SMTZ (r^2=0.92). It is, however, not distinctly correlated with any of the absolute reaction rates except for POCSR (r^2=0.61), which suggests a connection between the SMTZ depth and organic matter degradation rate rather than with the AOM rate. The average POC content is inversely correlated with the organic matter degradation rate (r^2=0.54) and with the methane carbon isotope at the SMTZ (r^2=0.51).

Bhatnagar et al. (2011) suggested that the depth of gas hydrate first occurrence is positively correlated with the SMTZ depth assuming fluid flow is the most dominant factor affecting both. However for the Ulleung Basin, neither the depths of BSR nor that of the gas hydrate first appearance shows any appreciable correlation with the SMTZ depth nor with the carbon or sulfate fluxes. Bhatnagar et al. (2011) shows that SMTZ depth and sulfate gradients may be used to infer the average gas hydrate saturation in the Cascadia margin system but only when all methane comes from a deep external reservoir (*e.g.*, gas hydrate) and AOM is the only sink of sulfate. Our box model results indicate that neither of these assumptions is valid in the Ulleung Basin, since POCSR consumes a significant fraction of sulfate and there is an important methane source that originates just below the SMTZ also contributes to the overall carbon cycling within the SMTZ. There is also no correlation between the AOM rate and gas hydrate abundance indicators (*i.e.*, depth of BSR and first gas hydrate appearance in Table 2-1), which suggests that the deep gas hydrate system (>70 mbsf) in these diffusion-dominated sites at Ulleung Basin is too remote to

effectively influence the shallow (< 30 mbsf) carbon cycles around the SMTZ. Thus, in the sites discussed here, the AOM rates cannot be used to quantify methane contributions from gas hydrate reservoirs that lay tens to hundreds of meters below the SMTZ. Nonetheless, we speculate that the advective systems that characterize acoustic chimney locations in the Ulleung Basin (Torres et al., 2011; Kim et al., 2011, 2012) will indeed have a profound influence on the carbon cycling around the SMTZ.

2.7.2 Evidence for coupling AOM and CR in natural and laboratory studies

Carbon cycling through an AOM-CR coupled pathway at the SMTZ, was originally proposed by Borowski et al. (1997), based on observations of anomalously light carbon isotopic values of DIC and methane around the SMTZ in samples collected by Ocean Drilling Program at the Blake Ridge (Claypool and Threlkeld, 1983; Galimov and Kvenvolden, 1983). Since then, an anomalously light carbon isotopic signature of microbial biomass (House et al., 2009) and lipid biomarkers (Orcutt et al., 2005; Alperin and Hoehler, 2009) near the SMTZ, have been used as an important AOM-CR coupling indicator, because the measured fractionations cannot be explained solely from organic carbon degradation, and require fractionation by methanogens (Alperin and Hoehler, 2009).

Direct evidence for the existence of this AOM-CR coupling was presented by Zehnder and Brock (1979, 1980), who quantified both reactions simultaneously in culture experiments. Radiotracer experiments have also shown that the CR rate is not only of comparable magnitude to that of AOM, in some cases, these rates are shown to be proportional to each other (Pimenov et al., 1997; Orcutt et al., 2005; Seifert et al., 2006; Knab et al., 2009) and maybe a function of the methane and sulfate availability (Orcutt et al., 2008).

Hoehler et al. (1994) postulated that the methanogenic archaea, which mediate AOM, may be able to switch their metabolism between methanogenesis and methanotrophy depending on the fluid composition, and thus may thermodynamically favor one pathway over the other. In addition, metagenomic studies of communities collected

from the SMTZ indicate that methanotrophic archaea possess most of the genes that are typically required for methanogenesis thus supporting the hypothesis that these microbes are capable of carrying out "reverse methanogenesis" (Hallam et al. 2004). Whether methanogenic archaea can indeed switch their metabolic pathway is still debated. However, rDNA and rRNA maxima at and immediately below the SMTZ, were used by Lloyd et al. (2011) to reinforce the idea that ANME-1 may indeed be capable of consuming and producing methane, and that the dominant metabolic pathway does depend on the attendant geochemical environment.

Of course, for CR to precede an additional source of H_2 is needed. We do not know that the H_2 source has been established; however, the aforementioned studies all show the coupling between AOM and CR to be highly prevalent. The actual metabolic pathways and the organisms involved are still being debated by the geomicrobiology community; however, it is becoming more and more apparent that the AOM and CR reaction rates are interdependent and are controlled by the methane and sulfate availability. These observations and the results of our box model indicate that it is necessary to take this important carbon cycling pathway into consideration in future studies aimed at unraveling processes at, and immediately below, the SMTZ.

2.7.3 Future improvements

We were not able to uniquely solve all 5 reactions involved in the cycling of carbon (Case 4), due to lack of additional data. Quantification of the 5 unknowns (R_{OM}, R_{AOM}, b, α_{AOM}, and f) from field or experimental studies, would allow us to fully constrain the system. Alternatively, we can also use robust data on the in situ methane concentrations, which would allow us to confidently estimate the methane fluxes from beneath the ESMTZ ($C_{CH4\text{-}bot}$ or $F_{CH4.in}$ in Figure 2-4A). This in situ methane concentration may be obtained by sampling the sediments with a pressure core sampler (PCS) that maintains the in-situ conditions. Results from Case 3 and 4 also emphasize the need of incorporating the methane isotopic composition to fully constrain the carbon metabolic pathways in the SMTZ. These data have not been included in previous studies (Snyder et al., 2007) or its significance was not fully appreciated (Chatterjee et al., 2011; Malinverno and Pohlman, 2011).

2.8 Conclusion

Sulfate gradients have been used as an important proxy to quantify the methane supply from deep reservoirs such as gas hydrate, which is critical to fully constrain carbon cycling in marine sediments. However, the commonly used assumption that sulfate gradients are fully coupled to the anaerobic oxidation of methane (AOM) is complicated by the sulfate consumption from organic matter degradation (POCSR), and carbon cycling between pools of methane and dissolved inorganic carbon (DIC) via and CO_2 reduction (CR).

We developed a box model, which incorporates stoichiometry, flux, and isotopic mass balances, to constrain the relative proportion of the five reactions involved the cycling of carbon within the SMTZ. We show that in the Ulleung Basin, more than half of the DIC input to the SMTZ is directly related to organic matter degradation (either via sulfate reduction, POCSR, or methanogenesis (ME), while AOM is responsible for the rest of DIC flux. The fraction of DIC that is reduced to methane via a secondary methanogenesis (*i.e.,* CR) within the SMTZ ranges from 25 to 35%, and the methane produced by this reaction will further feed AOM.

By including isotopic considerations in our model, the quantification of organic matter degradation and of the cycling of carbon between the DIC and methane pools (through AOM and CR) revealed that the rates of AOM and sulfate reduction are not necessary equal to each other, as would be suggested by mass fluxes alone. Instead, the fraction of sulfate consumed by AOM ranges from 70 to 90%. Therefore, whereas first order relative estimates of methane fluxes can be made based solely on sulfate data, such methane flux estimates may have errors that range from 10 to 30%.

Isotopic data was also the key in documenting that AOM is not supported in its entirety by a methane flux into the SMTZ from deep sources, rather a significant contribution of this methane originates immediately below the SMTZ. Thus, at least in the Ulleung Basin, the SMTZ depth by itself cannot be used as a quantitative indicator of methane supplied from gas hydrate reservoirs, as it has been postulated for other gas hydrate bearing locations.

2.9 Acknowledgements

The authors would like to thank the co-chief scientists (Byong-Jae Ryu, Timothy S. Collett, and Michael Riedel), the captain, crew members, and shipboard scientific party of the D/V Fugro Synergy for the excellent support they provided during the 2010 UBGH2 Expedition. This project was made possible with the funding support from Korea Institute of Geosciences and Mineral Resources (KIGAM) (GP2012-026) and US Department of Energy, National Energy Technology Lab under RES contract (DE-FE0004000). The authors would also like to thank Dr. Reimers and three anonymous reviewers for valuable comments to the manuscript.

Figure 2-1 The definitions of SMTZ and ESMTZ considered in our model. ESMTZ stands for Expanded Sulfate Methane Transition Zone that includes the shollow methanogenic zone right below the SMTZ.

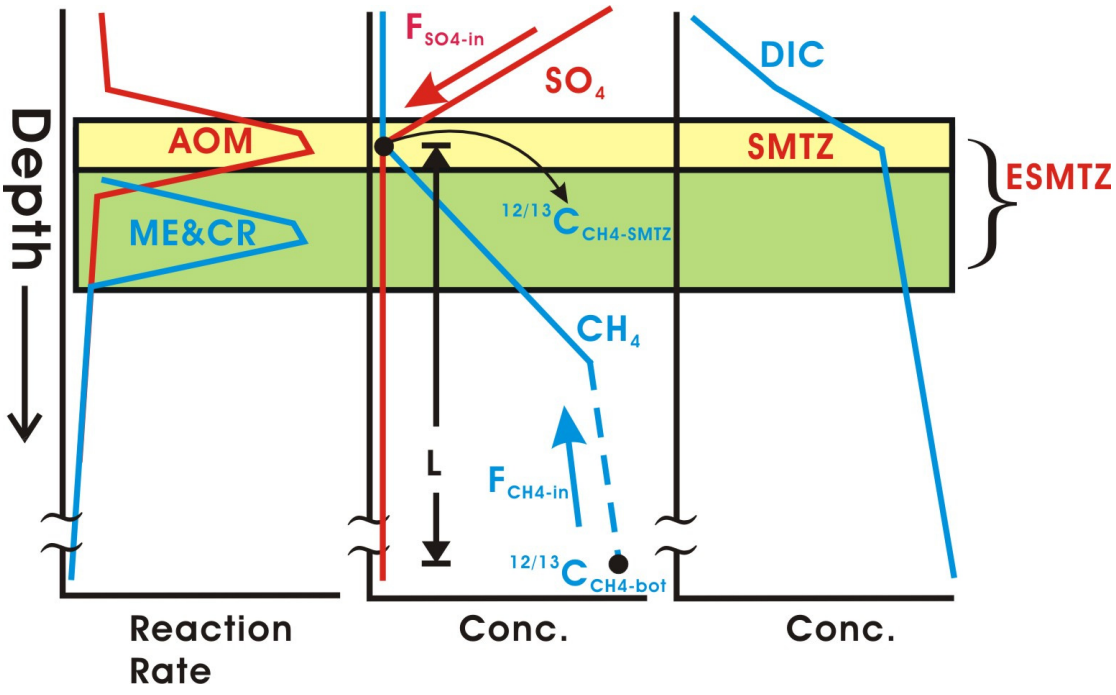

Figure 2-2 Map of the UBGH2 drill sites in the Ulleung Basin. (A) Regional map of the basin. (B) The five sites investigated in this study.

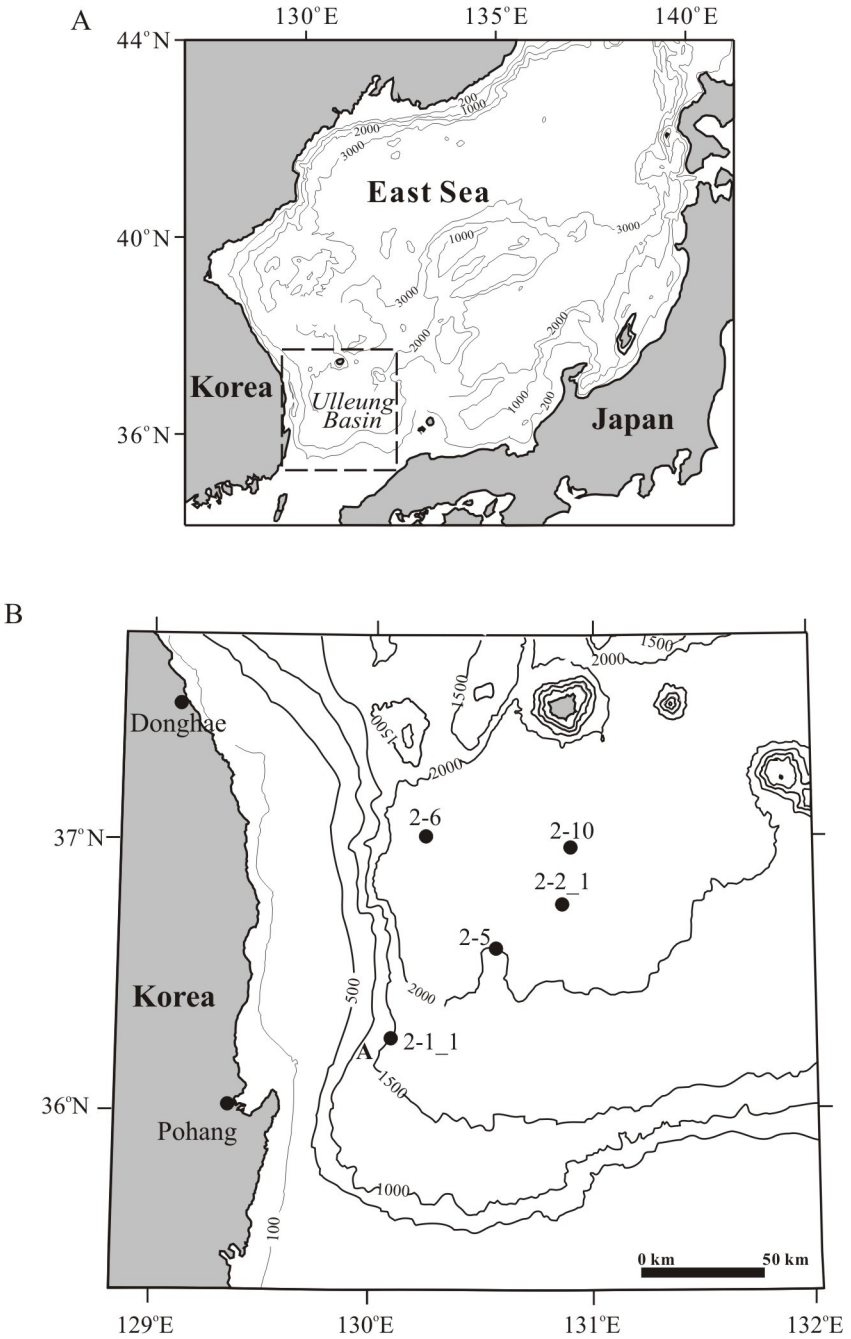

Figure 2-3 Porosity profiles of the study sites. Black dots are onboard measurements while black lines are fitted profile using the parameters listed in Table 2-2.

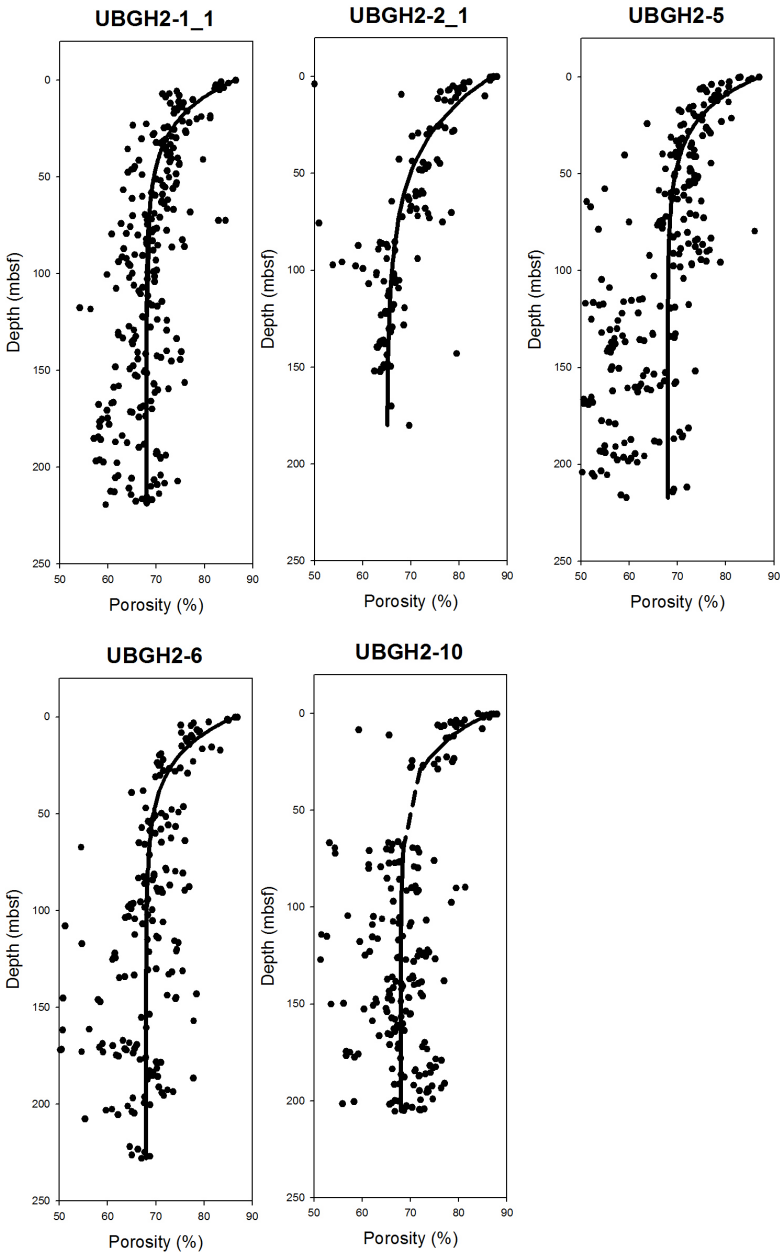

Figure 2-4 Pore water profiles of data available for the box model. Red arrows illustrate the flux terms used in our box model. $r_{CH4.SMTZ}$, $r_{DIC.SMTZ}$ are $^{12}C/^{13}C$ of DIC or CH_4 that are calculated from isotopic values.

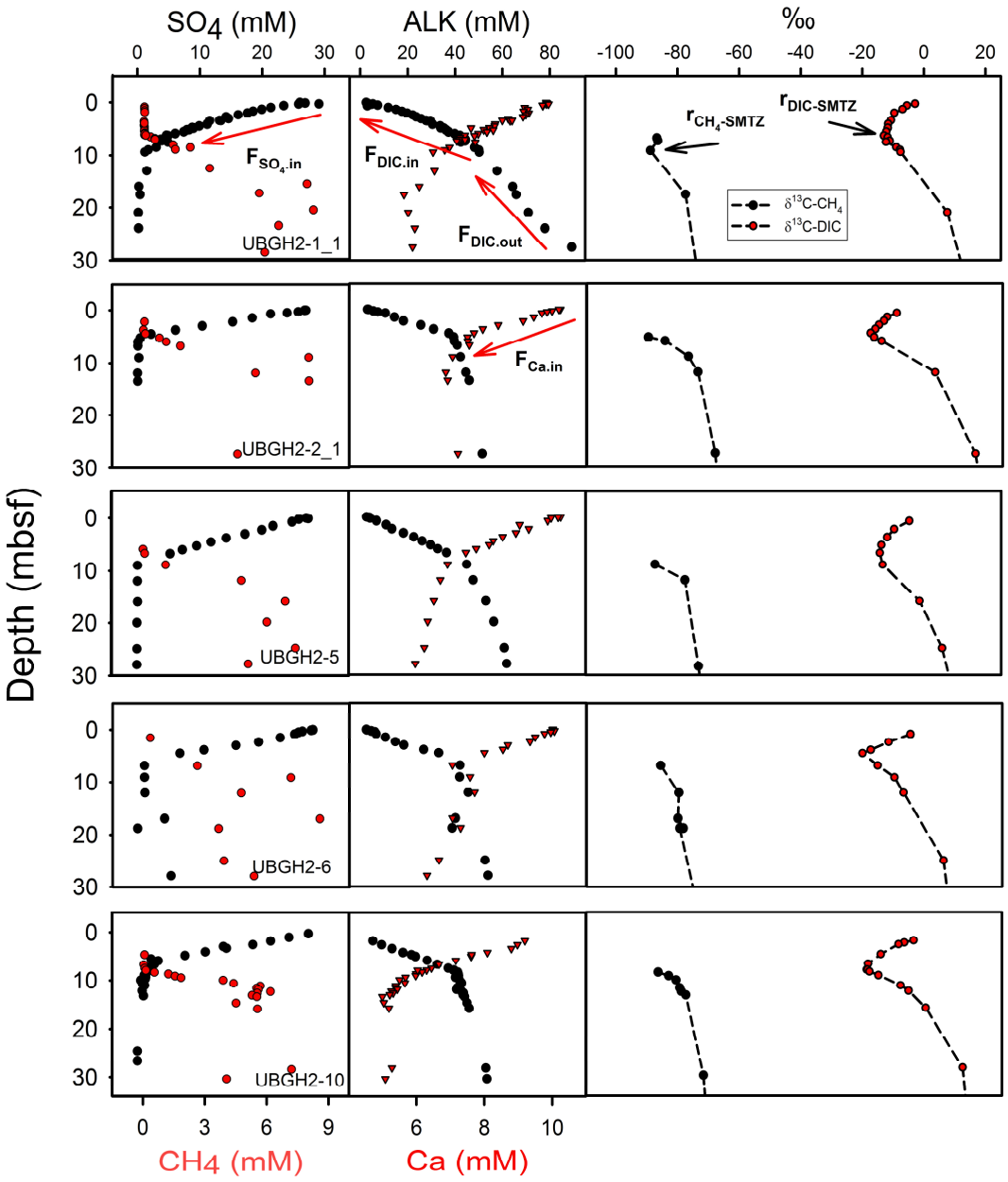

Figure 2-5 Framework of our box model. (A) Illustration of box model for Case 1, which only considers AOM and CP with in the SMTZ. (B) POCSR is added into the box in addition to the reactions considered in Case 1. (C) CR is included in the box model in addition to the reactions considered in Case 2. (D) ME is included in Case 4 which requires expanding the SMTZ (*i.e.,* ESMTZ) in this case.

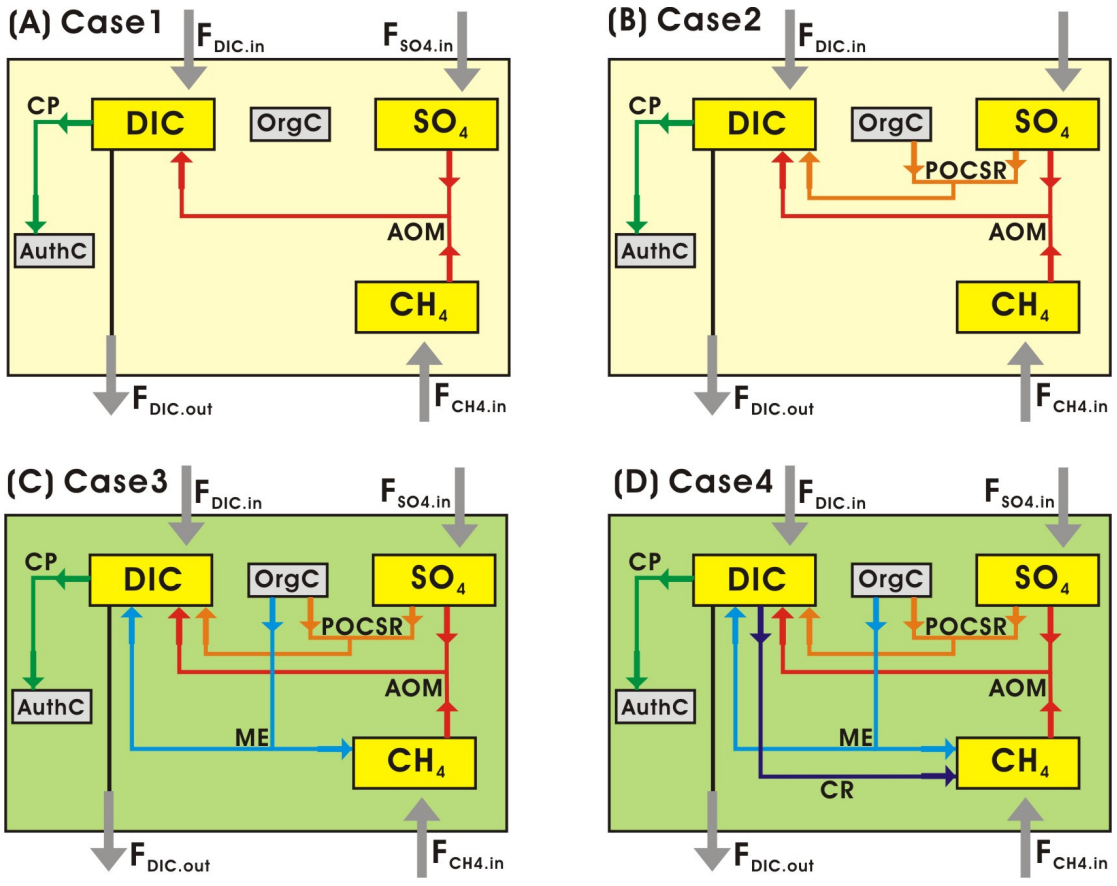

Figure 2-6 The isotopic fractionation factors for AOM (α_{AOM}) calculated from our box model based on the 4 different settings. The green area indicates range of fractionation factors from the literature (1.004-1.03; Whitcar, 1999). In Case 1 and 2, the fractionation factors are notably lower than expected. For Case 3, only the value for the site UBGH2-10 falls in the reasonable range; the rest are distinctly higher than expected range of value. The fractionation factors for sites UBGH2-1_1 and UBGH2-5 are much larger than 2; thus, they are not plotted in the figure. All the fractionation factors calculated from all sites in Case 4 agree well with the expected range indicating that isotopic mass balance is satisfied in this setting.

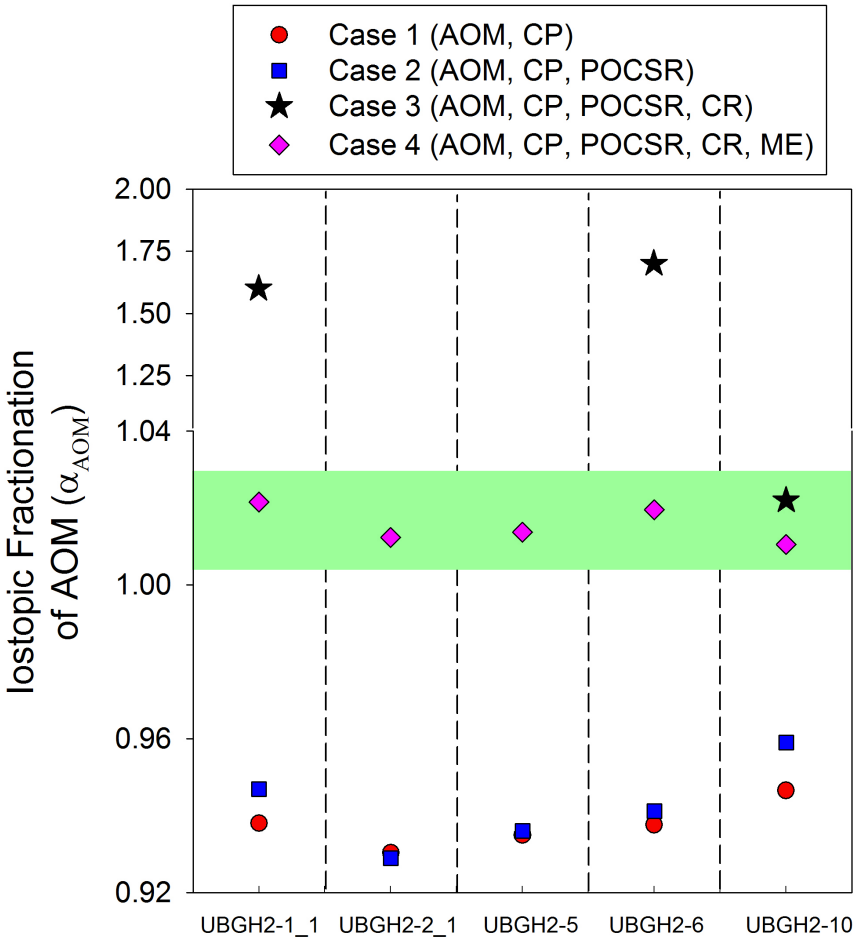

Figure 2-7 (A) Relationship between fraction of organic matter that is consumed by sulfate reduction (*f*) and isotopic fractionation of AOM (α_{AOM}). The horizontal dash line marks the range of α_{AOM} from literature (Whiticar, 1999). The vertical dash line marks the result of Case 3 which assumes all organic matter is consumed through POCSR. (B) Relationship between the fraction of organic matter that is consumed by sulfate reduction (*f*) and the fraction of DIC that is recycled by AOM (*b*) at each of the five sites. Only the *f* values that result in the literature α_{AOM} values in (A) are plotted here.

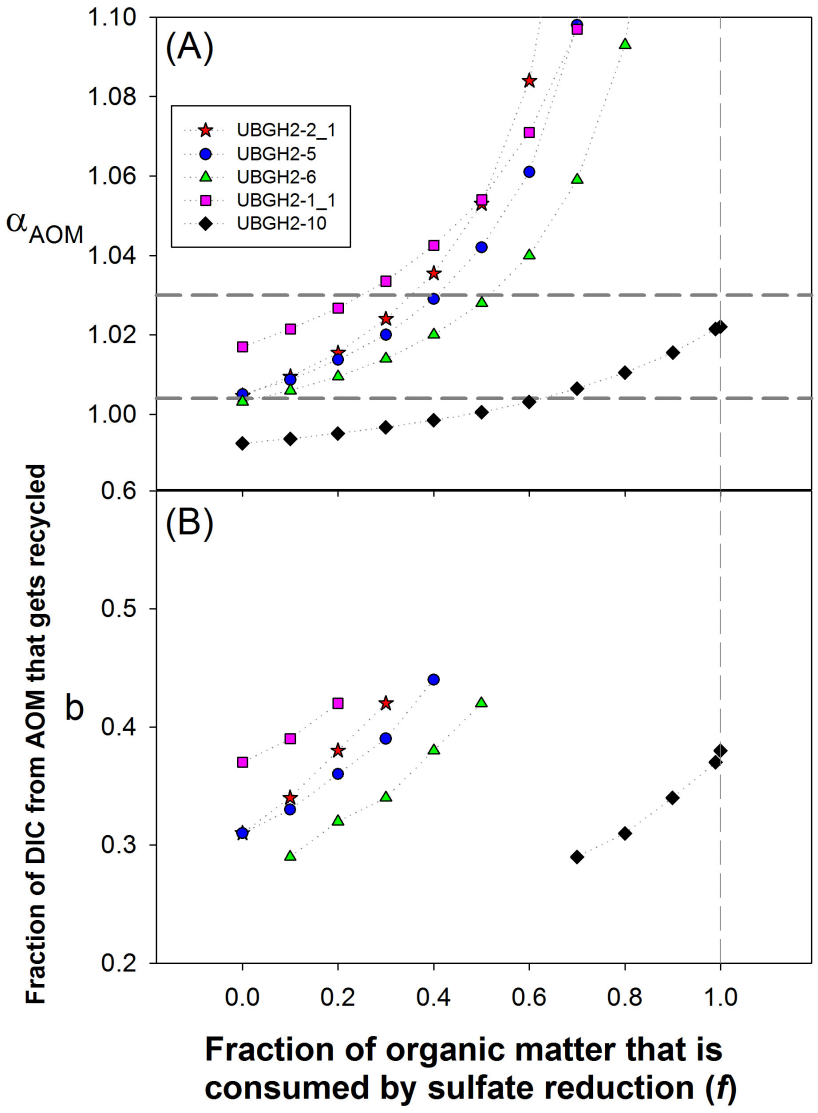

Figure 2-8 The relative contribution of each reaction. In the left panel, the contribution from the five reactions studied are normalized with different DIC fluxes ($\Delta F_{DIC}=F_{DIC.in}-F_{DIC.out}$). In the right panel, the fraction of sulfate that is consumed through AOM is plotted. The bars at the top of each column represent the range of contributions.

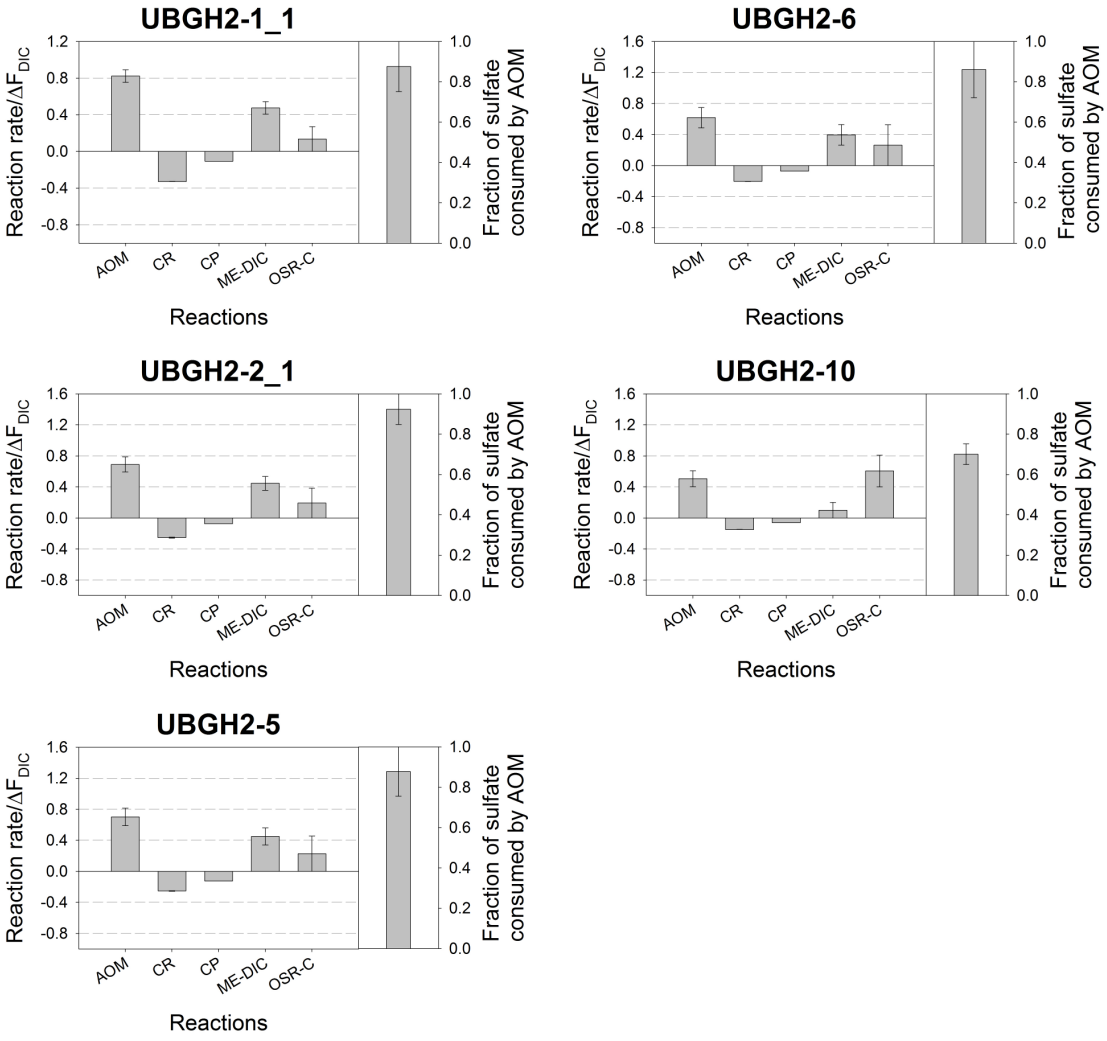

Table 2-1 Depth of the BSR, first appearance of gas hydrate and the SMTZ, as well as organic carbon content of the study sites

Site	BSR (mbsf)	First GH appearance depth (mbsf)	Depth of the SMTZ (mbsf)	POC (wt%)		
				Min.	Average	Max.
UBGH2-1_1	165	93	7.7	0.62	1.93	4.03
UBGH2-2_1	176	71	7.0	0.31	1.59	3.66
UBGH2-5	189.5	153	8.0	0.16	1.30	3.91
UBGH2-6	167	113	6.6	0.09	1.23	4.15
UBGH2-10	171	77	6.2	0.21	1.40	3.44

Table 2-2 Parameters used to fit the porosity profiles shown in Figure 2-2

Site	Initial porosity at water-sediment interface ϕ_0 (%)	Final porosity at depth ϕ_f (%)	empirical constant for data fitting γ
UBGH2-1_1	86.50	68.00	-0.05
UBGH2-2_1	87.00	65.00	-0.03
UBGH2-5	86.97	68.00	-0.05
UBGH2-6	86.48	68.00	-0.05
UBGH2-10	86.74	68.00	-0.05

Table 2-3 Fluxes (positive for upward flow) of various solutes across the SMTZ calculated from pore water profiles, DIC and CH_4 carbon isotopes at the SMTZ and at the core bottom for each of the 5 sites investigated in the Ulleung Basin. See text for the detailed definition of each term.

Site	$^{12}F_{DIC.in}$ ($\mu mol/cm^2/yr$)	$^{12}F_{DIC.out}$ ($\mu mol/cm^2/yr$)	$^{13}F_{DIC.in}$ (10^{-2} $\mu mol/cm^2/yr$)	$^{13}F_{DIC.out}$ (10^{-2} $\mu mol/cm^2/yr$)	$F_{SO4.in}$ ($\mu mol/cm^2/yr$)	F_{Ca} ($\mu mol/cm^2/yr$)	$^{13}C_{DIC-SMTZ}$ (‰)	$^{13}C_{CH4-SMTZ}$ (‰)	$^{13}C_{DIC-bot}$ (‰)	$^{13}C_{CH4-bot}$ (‰)	α_{CR}
UBGH2-1_1	1.92	7.44	2.23	8.28	-4.92	-0.59	-13.0	-88.8	17.0	-64.5	1.082
UBGH2-2_1	0.28	7.97	0.37	8.84	-6.04	-0.57	-17.8	-90.0	22.0	-62.0	1.084
UBGH2-5	0.63	7.25	0.76	8.03	-5.40	-0.84	-14.4	-87.4	18.5	-62.0	1.081
UBGH2-6	0.41	9.35	0.51	10.31	-6.70	-0.65	-20.4	-85.9	17.0	-63.3	1.080
UBGH2-10	0.57	9.53	0.76	10.49	-7.23	-0.55	-18.9	-86.6	20.0	-64.3	1.084

Table 2-4 Error of flux estimates for each of the dissolved species considered in our model

	UBGH2-1_1	**UBGH2-2_1**	**UBGH2-5**	**UBGH2-6**	**UBGH2-10**
$\mathbf{F_{SO4}}$	3.2%	3.2%	1.8%	3.3%	3.0%
$\mathbf{^{12}F_{DIC.in}}$	6.2%	14.7%	20.3%	9.1%	12.6%
$\mathbf{^{12}F_{DIC.out}}$	17.5%	16.7%	7.9%	11.2%	9.0%
$\mathbf{^{13}F_{DIC.in}}$	6.3%	8.9%	20.2%	9.1%	11.8%
$\mathbf{^{13}F_{DIC.out}}$	17.3%	14.5%	7.8%	11.2%	9.1%
$\mathbf{F_{Ca}}$	3.2%	4.9%	12.0%	4.4%	2.9%

Table 2-5 Range of the depth-integrated reaction rates (μmol/cm^2/yr) derived from Case 4.

	R_{AOM} μmol/cm^2/yr	R_{CR} μmol/cm^2/yr	R_{CP} μmol/cm^2/yr	R_{OM} μmol/cm^2/yr	R_{ME} μmol/cm^2/yr	$R_{POCSR-C}$ μmol/cm^2/yr
UBGH2-1_1	4.54±0.37	1.81±0.01	0.58	6.00±0.01	5.25±0.76	0.75±0.75
UBGH2-2_1	5.30±0.74	1.96±0.05	0.56	8.34±0.11	6.86±1.37	1.48±1.48
UBGH2-5	4.65±0.75	1.68±0.02	0.83	7.47±0.04	5.97±1.46	1.50±1.5
UBGH2-6	5.53±1.17	1.83±0.01	0.64	9.41±0.01	7.06±2.36	2.35±2.35
UBGH2-10	4.52±0.92	1.34±0.02	0.55	7.22±0.04	1.80±1.8	5.42±1.83

CHAPTER 3

Towards quantifying the reaction network around the sulfate-methane-transition-zone in the Ulleung Basin, East Sea, with a kinetic modeling approach

Wei-Li Hong, Marta E. Torres, Ji-Hoon Kim,
Jiyoung Choi, and Jang-Jun Bahk

Gechimica et Cosmochimica Acta
in review

3.1 Abstract

We present a kinetic model based upon pore water data collected from eight sites drilled during the second Ulleung Basin gas hydrate drilling expedition (UBGH2) in 2010. Three sites were drilled at locations where acoustic chimneys were identified in seismic data, and the rest were drilled on non-chimney environments. We employ our model and include all necessary compositional and isotopic profiles to understand the difference between those two environments in terms of reactions around the sulfate-methane-transition-zone (SMTZ). Our model assessment reveals very different biogeochemistry between the two environments. Organic matter decomposition is an important process for production of methane, dissolved inorganic carbon (DIC) and consumption of sulfate in the non-chimney sites, whereas anaerobic oxidation of methane (AOM) dominates both carbon and sulfur cycles in the chimney environment. Different sources of methane mediate AOM in the two settings. Internally produced methane through CO_2 reduction (CR) and methanogenesis fuels AOM in the non-chimney sites, whereas AOM is sustained by methane from external sources in the chimney sites. We also simulate the system evolution from non-chimney to chimney conditions by increasing the bottom methane supply to a non-chimney setting. We show that the higher CH_4 flux leads to a higher microbial activity of AOM, and more organic matter decomposition through mehanogenesis. A higher methanogenesis rate and a smaller CR/AOM rate in the chimney sites are responsible for the isotopically lighter DIC and heavier methane in this environment relative to the non-chimney sites.

3.2 Introduction

Anaerobic oxidation of methane (AOM) in marine sediments is the main reaction that prevents methane from leaking into the water column and potentially the atmosphere (Barnes and Goldberg, 1976; Heeschen et al., 2005; Chuang et al., 2006; Yang et al., 2006; Reeburgh, 2007; Regnier et al., 2011). A thorough understanding of AOM is thus critical to assessing the role of deep-subseafloor methane (*e.g.,* gas hydrate, gas/oil reservoirs, etc) on the carbon cycle under past, present or future environmental changes. The sulfate-methane-transition-zone (SMTZ) in marine sediments, where sulfate is exhausted and methane concentration starts to increase, is intuitively related to the strength of AOM (Borowski et al., 1996; Dickens, 2001; Chuang et al., 2010); though the actual reaction pathways can not be easily inferred solely from concentration profiles and may require consideration of carbon isotopic data (Borowski et al., 1997; Chatterjee et al., 2011; Hong et al., 2013).

Previous studies have sketched a first-order picture of the many interdependent biogeochemical reactions around SMTZ (Borowski et al., 1996; Dale et al., 2006; Wallmann et al., 2006; Chatterjee et al., 2011; Regnier et al., 2011; Hong et al., 2013), and it is now widely accepted that the depth of SMTZ is controlled by the interaction of several reactions, such as organoclastic sulfate reduction (Fossing et al., 2000; Wallmann et al., 2006), CO_2 reduction (Borowski et al., 1997; Pohlman et al., 2008; Hong et al., 2013), and methanogenesis (Chatterjee et al., 2011). To better understand the system, we need a more comprehensive and quantitative understanding of how the carbon and sulfur cycles are connected at the SMTZ. Hong et al. (2013) presented a box model calculation, based on the balances of mass, flux, and isotopes of carbon, which allows for first-order estimates of the relative weight of these different reactions based on the geochemical profiles in various diffusion-dominated locations. This calculation is, however, restricted to steady-state conditions and only applicable to environments where diffusion is the dominant mechanism supplying methane to the SMTZ. In the Ulleung Basin, there are many locations where acoustic chimneys have been identified in the seismic data (*e.g.*, Haacke et al., 2009; Horozal et al., 2009; Torres et al., 2011; Yoo et al., 2013). These chimneys are known to act as advective methane gas conduits that fuel massive gas hydrate formation near the seafloor (Torres et al., 2011; Kim et al., 2012; Choi et al., 2013).

In this work, we present a kinetic model that simulates the concentration and isotopic profiles of pore water from eight sites drilled in Ulleung Basin, offshore Korea, during the second gas hydrate drilling expedition (UBGH2) (Figure 3-1). We build our kinetic model using data from the five sites that are apparently diffusion-dominated, as they were drilled away from seismic blanking structures (non-chimney sites hereafter). These data were used by Hong et al. (2013) in their box model, and permit comparison between the steady state and kinetic model approaches. We also apply the kinetic model to three additional sites that were drilled at the acoustic blanking zone from the seismic profile to represent a high methane flux end member (Torres et al., 2011; Kim et al., 2012) (chimney sites hereafter). Such acoustic blanking zone is indicative to the upward migration of free gas, mostly methane, in the sediments, which lowers the acoustic velocity. Very shallow SMTZ (< 3mbsf) and the appearance of concentrated gas hydrate also infer the strong methane supply from below (KIGAM, 2011). We compare carbon and sulfur cycles in these two environments and study the biogeochemical response of the system to an increase of methane flux.

3.3 Model architecture

The model was implemented using CrunchFlow, a FORTRAN routine developed by Steefel (2009), and has been applied to many other studies (Maher et al., 2009; Yang et al., 2010; Hong et al., 2013). The model setup, including the geochemical database and input file, can be found in the Appendices 2 and 3.

3.3.1 Fundamental parameters

In CrunchFlow, a global implicit scheme (GIMRT; Steefel and Yabusaki, 1996), which solves the reaction and transport terms simultaneously in each step, is used for the diffusion dominated systems (*i.e.,* systems with low Péclet number). An explicit, operator splitting numerical scheme (OS3D; Steefel and Yabusaki, 1996), which provides better numerical stability in the environments with high Péclet numbers, is adopted as solver. CrunchFlow chooses the type of scheme it uses automatically based on the transport behavior of the simulation.

We use a 20-m model frame for the non-chimney sites and a 5-m long frame for the chimney sites, such that it excludes free gas from the model regime. We ran the simulation for 400 and 100 kyr at the non-chimney and chimney sites, respectively. These time periods correspond to the time needed for the first sediment parcel to move through the model frame. Although steady state is not assumed, the simulation time is long enough for all dissolved and solid species to reach steady state. We chose 15 primary species as the fundamental building blocks of the model. In addition, we selected ten secondary species, five gases, and five minerals, which can all be formulated exclusively by primary species. The full list of species considered is listed in Table 3-1. The porosity profiles at each site were obtained by fitting the observed profiles with the classic equation for depth-dependent porosity (Boudreau, 1997):

$$\phi(z) = \phi_f + (\phi_0 - \phi_f)\exp(\gamma z) \quad (3.1)$$

where ϕ_f and ϕ_0 are the asymptotic porosity and porosity at the water-sediment interface, respectively. γ is an empirical constant obtained from data-fitting. Values for these parameters are reported in Table 3-2. The seafloor temperature and geothermal gradient at each site (Ryu et al., 2012; Riedel et al., 2013) are also listed in Table 3-2. We used the formulations of Boudreau (1997) to calculate the molecular diffusion coefficients for all dissolved species at 25 ^{o}C in a pure media (e.g., water), and a diffusion activation energy of 4.5 kcal/mol is used to calculate diffusion coefficients at temperatures other than 25 ^{o}C (Appendix 2). In order to account for the effect of tortuosity on diffusion coefficients in porous media, we adopted the information of formation factor (FF) calculated by Riedel et al. (2013) from the electrical resistivity logging. We related the downcore formation factor profile with porosity through Archie equation:

$$FF = \phi^{m} \quad (3.2)$$

the *m* value can then be fed to CrunchFlow to derive the effective diffusion coefficient in sediments. We adopt an average *m* of 1.9 for our simulation at all sites. Based on the age model derived from the micro-fossil records (Yi et al., 2012), we calculated

the sedimentation rates to be 4.6×10^{-5} to 6.6×10^{-5} m/yr. An average value of 5.6×10^{-5} m/yr was chosen as solid burial rate for all sites. With a steady-state compaction assumption, Berner (1980) showed that the pore water burial rate can be related to solid burial rate through the porosity change with depth. Based on our porosity profiles, we estimated a pore water burial rate of 3.1×10^{-5} m/yr (55% of solid burial rate). We chose Dirichlet type upper and lower boundary conditions and assigned them based on the measured concentrations. Bottom water composition for pore water was used as the initial condition at each site.

3.3.2 Reaction network and carbon isotopes

Our model includes 19 reactions which are listed in Table 3-3 with the corresponding abbreviations used in this study. The reaction network is illustrated in Figure 3-2, and comprises the carbon (upper middle in Figure 3-2) and sulfur (lower left in Figure 3-2) cycles, which are linked via AOM (Eq. 17). CO_2 reduction (CR, Eq. 18), which we describe here as methane generated from the dissolved inorganic carbon (DIC) produced from both organic carbon degradation and AOM, has been commonly ignored in previous studies. Hong et al. (2013), however, showed the significance of this reaction to achieve an isotopic mass balance of carbon around the SMTZ. Particulate organic matter (POC) is consumed via either sulfate reduction (POCSR) (Eq. 20) or methanogenesis (ME) (Eq. 21). Authigenic carbonate (CP, Eq. 19) removes dissolved carbonate species from the pore water. Methane in our model can be generated in-situ through CR and ME or delivered to our modeled sediment layer by external fluid.

Hydrogen sulfide is produced from both AOM and POCSR. Formation of pyrite (Eq. 22) down to the depth of SMTZ has often been associated with these reactions (*e.g.*, Wallmann et al., 2006; Lim et al., 2011), but the exact formation mechanism remains controversial (Burdige, 2006). For our modeling purposes we adopted a pyrite precipitation from the less crystalline mineral mackinawite, as inferred from both theoretical calculations and lab experiments (Rickard, 1997; Rickard and Luther, 1997, 2007; Dale et al., 2009). This process fixes hydrogen sulfide from pore water and produces hydrogen gas, which supports CR. The most likely iron sources for

mackinawite formation are the labile Fe oxyhydroxides. Other minerals, such as hematite may also act as Fe sources, but these minerals are not included in the current model.

To correctly account for the change of alkalinity and pH, we included all major cations and anions, as well as various acid-base pairs of carbon, sulfur, nitrogen, and phosphate species (Eq. 6 to 13). The acid-base pairs are treated as secondary species in CrunchFlow, and are assumed to reach immediate equilibrium. CH_4 and CO_2 gases are allowed to form (Eq. 14 and 15), but for simplicity in this current version of the model, the gas phase is pinned to the pore water and is not allowed to migrate as a separate phase and the fluid is considered to reach up to 100% saturation. Kim et al. (2012) presented evidence from carbon isotopic fractionation in support of a two-phase transport (gas and liquid) at chimney sites. We acknowledge this process but have not included this two-phase transport in the current model.

The carbon isotopic profiles were modeled by tracking ^{12}C and ^{13}C in all carbon species individually. Within our formulation, the measured isotopic variability can be explained by four different processes. First, a diffusion-induced fractionation has been quantified by Zeebe and Wolf-Gladrow (2001), who showed that the diffusion coefficients are inversely proportional to the square root of the reduced masses. Secondly, isotopic changes can result in mixing of carbon with different isotopic signatures and without any isotopic fractionation. For example, DIC released from POCSR (Eq. 20) has a constant carbon isotopic signature that is similar to the organic matter (values of -23 or -19 ‰ from Kim (2007) were used for non-chimney and chimney sites, respectively). ME (Eq. 21) releases methane and DIC with very different isotopic signatures (Table 3-4) that reflects the isotopic fractionation during this reaction. The authigenic carbonate also has a constant carbon isotopic signature of -38‰ (Nehza et al., 2012). Noticeable difference in carbon isotopes was not observed from the authigenic carbonates between chimney and non-chimney sites (Nehza et al., 2012). The third type of isotopic fractionation is the equilibrium reaction between the various carbonate species, which can be as large as 9‰ between $CO_{2(aq)}$ and HCO_3^- (Mook, 1986; Zhang et al., 1995). This is accounted for in our model by including the ^{12}C and ^{13}C carbonate species. The last source of fractionation

comes from the kinetic effect of the non-equilibrium reactions such as AOM and CR. We estimated this fractionation effect by assigning different kinetic constants for each of these reactions as detailed in the next section.

3.3.3 Reaction Formulation

Reactions can be classified as either homogeneous or heterogeneous (Table 3-3). Homogenous reactions include acid-base, gas dissolution, and aquatic redox reactions (Table 3-3a). Acid-base reaction and gas dissolution are described by assigning appropriate equilibrium constants (*i.e.*, K_a and K_H) from either the CrunchFlow database or by theoretical estimates using the Zeebe and Wolf-Gladrow, (2001) approach (Appendix 3). Aquatic redox reactions (*i.e.,* AOM and CR) were formulated as double-Monod-type kinetic reactions, which require inputs for equilibrium constants (K_{eq}), half saturation constants (K_{half}), maximum reaction rates (k_{max}), and inhibition constants (K_{in}). AOM rates for ^{12}C and ^{13}C were formulated as follow:

$$^{12/13}R_{AOM} = {}^{12/13}k_{\max}\left(\frac{C_{SO_4}}{C_{SO_4}+K_{half-SO_4}}\right)\left(\frac{C_{^{12/13}CH_4}}{C_{^{12/13}CH_4}+{}^{12/13}K_{half-CH_4}}\right)\left(1-\frac{Q}{K_{eq}}\right) \quad (3.3)$$

where C is the concentration of electron donors or acceptors, Q is the ion activity product, $K_{half-SO_4}$ and $^{12}K_{half-CH_4}$ were set to be 500 μM (Wegener and Boetius, 2009) and 5 mM (Nauhaus et al., 2002; Vavilin, 2013), respectively. $^{12}k_{max}$, $^{13}k_{max}$ and $^{13}K_{half-CH_4}$ were obtained from fitting curves to our data and reported in Table 3-4. The equilibrium constant, K_{eq}, was calculated from the standard molar Gibbs free energy (G^0_f) of each reaction at 25 ^oC (Table 3-5). The same K_{eq} was applied for the reactions involving isotopically light and heavy methane. For the Monod type of reaction, isotopic fractionation of AOM (α_{AOM}) was defined as (Maggi and Riley, 2009):

$$\alpha_{AOM} = \frac{{}^{12}k_{\max}\,{}^{13}K_{half-CH_4}}{{}^{13}k_{\max}\,{}^{12}K_{half-CH_4}} \quad (3.4)$$

A fractionation factor of 1.01 (Whiticar, 1999; Holler et al., 2009) was used for all the study sites.

A similar formulation was used for CR, with an additional inhibition term that describes the suppression of the reaction by the presence of sulfate:

$$^{12/13}R_{CR} = {}^{12/13}k_{\max}\left(\frac{C_{H_{2(aq)}}}{C_{H_{2(aq)}}+K_{half-H_2}}\right)\left(\frac{C_{^{12/13}HCO_3}}{C_{^{12/13}HCO_3}+{}^{12/13}K_{half-HCO_3}}\right)\left(1-\frac{Q}{K_{eq}}\right)\left(\frac{K_{in}+C_{SO4}}{K_{in}}\right) \quad (3.5)$$

A K_{half-H_2} value of 1 μM was used (Jin and Bethke, 2005) and the other kinetic parameters in Eq. (3.5) are reported in Table 3-4. The isotopic fractionation of CR (α_{CR}) was formulated as:

$$\alpha_{CR} = \frac{^{12}k_{\max}\,{}^{13}K_{half-HCO_3^-}}{^{13}k_{\max}\,{}^{12}K_{half-HCO_3^-}}$$

A constant value 1.098 was used at all sites (Whiticar, 1999; Holler et al., 2009).

Heterogeneous reactions, or water-rock interactions, include organic matter degradation, mineral precipitation/dissolution (calcite, pyrite, and mackinawite) and ammonium adsorption (Table 3-3b). Mineral precipitation/dissolution (i.e., Calcite, aragonite, pyrite, and mackinawite) were formulated using the default *tst* rate expression in CrunchFlow:

$$R = A_m k_m \exp[\frac{-Ea}{RT}]\prod a_i^n[1-\frac{Q}{K_{eq}}] \quad (3.6)$$

where A_m (=1 for all minerals) are k_m (Table 3-4) are the surface area and kinetic constant. Ea, R, and T are the activation energy, ideal gas constant, and temperature. Πa_i^n is the activity product of solutes in the reaction with their stoichiometry (n) as exponents. $\frac{Q}{K_{eq}}$ determines the direction of reaction where Q is the ion activity product and K_{eq} is the equilibrium constant.

POCSR follows Eq.(24) (Table 3-3b) in the sulfate reduction zone while CH_4 and CO_2 are produced following Eq. (25) in the methanogenesis zone (ME). These two reactions were formulated in a similar fashion as Eq. (3.6) but different in a sense that additional Monod and inhibition terms are included. POCSR has one Monod term that is imbedded in k_m:

$$k_m = k_{\max}\left(\frac{C_{SO4}}{C_{SO4}+K_{half}}\right) \quad (3.7)$$

where k_{max} is the theoretical maximum rate (Table 3-4), K_{half} is the half saturation constant (=100 μM; Wegener and Boetius, 2009), and C_{SO4} is the concentration of sulfate. ME has no Monod term but is inhibited by sulfate, bicarbonate, and methane (Wallmann et al., 2006) by adding the inhibition terms in Eq. (3.6):

$$I_{in} = \left(\frac{K_{in.SO4}+C_{SO4}}{K_{in.SO4}}\right)\left(\frac{K_{in.CH4}+C_{CH4}}{K_{in.CH4}}\right)\left(\frac{K_{in.HCO3}+C_{HCO3}}{K_{in.HCO3}}\right) \quad (3.8)$$

where $K_{in.SO4}$, $K_{in.CH4}$, $K_{in.HCO3}$ are the inhibition constant (1.6 mM, 15 mM, and 15 mM, respectively), and C is the concentration of these inhibitors. Nutrients (NH_4^+ and HPO_4^{-2}) are released during organic matter degradation following the Redfield ratio (Park et al., 2005). Ammonium adsorption is formulated as an ion exchange reaction in CrunchFlow, adopting the Gaines-Thomas convention. The concentration of available exchange sites was expressed as the charge equivalent concentrations (CEC). The value of 1.5×10^{-4} equivalents/g sediments was used for CEC concentration (Rosenfeld, 1979).

3.3.4 Model-experiment setup

To investigate how each reaction responds to an increase in methane flux, we let the model simulate the changes from the geochemical conditions of UBGH2-1_1 (a non-chimney site) to the conditions observed in UBGH2-3 (a chimney site) by delivering more methane to the bottom of the model frame (17 times larger bottom methane

flux). In other words, we suddenly increase the methane concentration at the lower boundary condition.

3.4 Pore water data and geochemical environment

The available data allow us to constrain our model results including carbon isotopes of DIC and methane (Figure 3-3) as well as the concentration of sulfate, calcium, magnesium, ammonium, alkalinity, hydrogen sulfide (only available in 3 sites), and pH (Figure 3-4). All these data and their corresponding analytic procedures have been reported elsewhere (*e.g.*, Ryu et al., 2012; Choi et al., 2013; Hong et al., 2013; Kim et al., 2013a).

At the non-chimney sites, the depth of SMTZ ranges from 5 to 10 meters below seafloor (mbsf) (Table 3-2), and gas hydrates occurred disseminated within the sediment or concentrated within coarse layers at depths ranging from ~70-190 mbsf (Table 3-2), where it occupies 12 to 79% of the pore space (Bahk et al., 2013). In contrast, the shallow depths of the SMTZ (<2 mbsf) at the three chimney sites point to a higher methane flux, where it is thought to support formation of massive gas hydrate at shallow depths (<10 mbsf) (Table 3-2; Torres et al., 2011; Kim et al., 2013b).

Distinct geochemical features can be observed from the isotopic profiles between the two groups. There is no significant difference in the isotopic signatures in the deep fluids and gas (>150 mbsf) among all sites (Figure 3-3 and Table 3-2). However, around the SMTZ, δ^{13}C-DIC is ~12-20 ‰ lighter at chimney sites relative to the non-chimney sites while δ^{13}C-CH_4 is enriched (~10-15 ‰) in chimney sites. These patterns indicate that reactions around the SMTZ, rather than variations in the fluid source, are responsible for these isotopic patterns.

3.5 Results and Discussion

By fitting our model results to the available data (Figure 3-4), we are able to derive reaction rate profiles. From these, we calculated the depth-integrated rates in terms of DIC, methane, and hydrogen sulfide production/consumption and reported them in Table 3-6 and Figure 3-5. The difference in reaction rates between the non-chimney and chimney sites is discussed in the following paragraphs.

3.5.1 DIC cycling around SMTZ

At all sites, we calculated a ΔF_{DIC} parameter (Figure 3-5a), defined as the difference between inflow and outflow of DIC, a negative value of this parameter represents a net outflux. For all of the non-chimney sites, the DIC production rates through organic matter degradation (POCSR+ME) within the model frame are at least 76% of the ΔF_{DIC}, indicating that the DIC produced through organic matter degradation can account for most of the observed DIC outflux. At these sites, DIC production rate via AOM is always lower than that from organic matter decomposition and accounts for only ~25 to 46% of the total ΔF_{DIC}. On the other hand, at chimney sites, organic matter degradation contributes only slightly to the overall rate, and AOM accounts for more than 85% of the total ΔF_{DIC}.

At non-chimney sites, the primary pathway for organic matter degradation is POCSR, which can account for up to 96% of total organic matter degradation. At chimney sites, however, POCSR within the shallow SMTZ becomes less important. In order to fit the isotopic data at the chimney sites, it is necessary to use higher kinetic constants for ME, which in turn result in higher ME rates in this setting. These results illustrate how the shallow sulfate reduction zone typical of chimney sites in the Ulleung Basin (and elsewhere), acts to deliver more labile organic matter to the methanogenesis zone, where high ME rates lead to enhanced methane generation.

CR, the reaction via which methane is produced by reduction of in situ DIC plus that derived from AOM, is an important sink of DIC for all sites (7-8.3%). However, the ratio of CR to AOM, which represents the portion of self-supported AOM fueled by the cycling between AOM and CR, is remarkably different between the non-chimney and chimney sites. These ratios range from ~20 to ~30% at non-chimney sites, but are only ~10% at chimney sites. These differences indicate that CR is less important, proportionally but not quantitatively, when AOM is actively fueled by high methane flux.

3.5.2 CH_4 cycling around SMTZ

Methane produced by organic matter degradation (*i.e.*, ME) within the model frame supports a fraction of the AOM at all sites (Figure 3-5b). At the non-chimney sites, up to 35% of methane consumed by AOM comes from ME, whereas a maximum 18% of AOM is supported by ME at chimney sites. The other internally-produced source of methane, CR, mediates about 19 to 33% of the AOM in the non-chimney sites and less than 10% in the chimney sites. This reaction describes the carbon cycling between AOM and CR, which helps stabilize the SMTZ when the methane flux is low (*i.e.*, non-chimney sites) and becomes less important when methane flux is high (*i.e.*, chimney sites). The methane that is delivered externally fuels only 37 to 57% of AOM in non-chimney sites but becomes much more important (fuels >74% of AOM) at chimney sites.

If we compare the magnitude of the external methane flux with the SMTZ depth in our sites (Figure 3-6a), we can observe how the external methane flux increases exponentially as SMTZ depth shoals. Such non-linear relationship was already emphasized by the global dataset of AOM rate and SMTZ depth compiled by Regnier et al. (2011). If we were to use a linear extrapolation based on the depth of SMTZ at sites UBGH2-5 and UBGH2-7 and assume that AOM is totally fueled by external methane, we would predict the external methane flux at site UBGH2-7 to be only four times higher than that at site UBGH2-5. A better estimate, based on our model shows that the methane flux at site UBGH2-7 is ~10 times higher than that at site UBGH2-5.

From Figure 3-6b, a loosely proportional relationship between external methane flux and the thickness of gas hydrate occurrence zone (GHOZ; BSR depth minus depth of first gas hydrate observed) suggests that the thickness of gas hydrate reservoir does influence the external methane flux, but factors such as lithology are also significant in controlling the abundance and the type of gas hydrate reservoir in Ulleung Basin (Bahk et a., 2013) and elsewhere (Torres et al., 2008). A universal relationship between geochemical- or geophysical-defined boundaries (*e.g.*, SMTZ, BSR, or GHOZ) and external methane fluxes as proposed by Bhatnagar et al. (2008) maybe possible, but it will require more information.

The source of methane from outside the model frame cannot be directly investigated by our model. However, we can make educated inferences based on the assigned boundary conditions. At chimney sites, the carbon isotopic composition of the methane present at the lower boundary conditions is similar to that reported for the gas hydrate-bounded methane recovered from the Ulleung Basin (Choi et al., 2013; Kim et al., 2013b), and it is commonly heavier than that for the non-chimney sites (Table 3-4). However, at all sites this isotopic signature reflects a microbial source (Choi et al., 2013; Kim et al., 2013b), suggesting that a large portion of the methane is produced by ME at depths deeper than those defined by our model frames, as suggested by Kim et al. (2011, 2012). Furthermore, since the dimension of our simulation is intended to exclude the depth where free gas may form, it is also possible the migration of free gas phase is responsible for the high methane flux in chimney sites, as suggested by Kim et al. (2012).

3.5.3 Sulfur cycling around SMTZ

The entire sulfate flux from seafloor is converted to hydrogen sulfide by either POCSR or AOM within the model frame (Figure 3-5c). For the non-chimney sites, POCSR accounts for 40 to 65% of the total sulfate reduction but only less than 8% is consumed by POCSR in the chimney sites. Hydrogen sulfide was not measured at all sites but only at two non-chimney sites (UBGH2-1_1 and UBGH2-10) (Figure 3-4a) and one chimney site (UBGH2-7) (Figure 3-4b). In these limited sample sets, only trace amount of hydrogen sulfide was detected, suggesting a rapid turnover rate for this species. Our model can correctly reproduce the hydrogen sulfide profiles at these sites by the removal terms that define pyrite and mackinawite formation. Precipitation of pyrite in turn produces hydrogen gas, which is required for CR, thus linking the sulfur cycle back to the carbon cycle.

In order to verify the rate of mackinawite and pyrite formation derived from our model, we estimated the solid Fe consumption rate in the shallow (<20 mbsf) sediments, using the Fe content in sediments in piston cored sediments recovered from the Ulleung Basin in 2003 (Kim, 2007). Assuming a sediment bulk density of sediments of 1.35 g/cm^3 (Ryu et al., 2012) and a long-term sedimentation rate of

5.6×10^{-5} m/yr (rate used in our model, Yi et al., 2012), the observed decrease of 1 wt% iron measured in the solid phase is equivalent to a consumption rate of:

$$\frac{1\ (\text{wt\%})\ \times\ 1.35\times10^{6}\ (\text{g/m}^3)\ \times\ 5.6\times10^{-5}\ (\text{m/yr})}{55.8\ (g\ /\ mol)} = 0.014\ (\text{mol/m}^2\text{/yr})\quad (3.9)$$

or 1.4 μmol/cm^2/yr of solid Fe consumption. This value is somewhat lower than the modeled mackinawite formation rate at the non-chimney sites, which ranges from 6.2 to 8.8 μmol/cm^2/yr (Table 3-6). Considering that the sedimentation rate used in this calculation represents a long-term average, which may underestimate the short-term rate (*i.e.*, sedimentation rate for the 20 meters), a slightly lower Fe consumption rate such as that calculated in Eq. (3.9) is expected. Nonetheless, the rate is of the same order of magnitude as the mackinawite formation in the non-chimney sites derived from our model (Table 3-6). Such agreement not only suggests a reasonable rate estimation from our model, but also points that pyrite formation can be sustained with this newly-formed mackinawite. Although more studies are required to verify the pyrite formation process in Ulleung Basin, this rate is large enough to produce hydrogen gas and sustain the required CO_2 reduction inferred from the carbon isotopic records.

3.5.4 Kinetic model vs. box model approaches

If we compare the reaction rate calculated by our previous box model (Hong et al., 2013) with the rates estimated by the new kinetic modeling (Figure 3-7), we note that both models point to an approximately equal contribution of AOM in DIC production (Figure 3-7a). The largest difference in terms of the absolute AOM rate was noted at site UBGH2-2_1. The concave-downward shape of the chlorinity profile at this site (Kim et al., 2013a) suggests the presence of an advective component, such that the pure diffusion assumption used in the box model may not be valid for this site.

The importance of the CR is apparent in both models, and the estimated CR rates are also similar in both models (Figure 3-7b). These agreements suggest that the simpler box model approach can indeed provide an adequate estimation of the CR rate and its

significance to the overall AOM. In the kinetic model approach, CR has a better theoretical formulation but it also requires more input parameters (*e.g.*, k_{max}, K_{half}, and K_{in}), which may not always be available. When information is limited, the box model approach can provide adequate rate estimates with only one parameter needed as input (parameter *b* in Eq. (21) from Hong et al., 2013).

The rates of the total organic matter degradation (POCSR+ME) estimated by both models are pretty similar (Figure 3-7c). However, the two models suggest different modes of organic matter degradation. In the box model calculations, most of the organic matter is degraded through ME whereas our kinetic model suggests otherwise. Such differences likely arise from the fact that the ME contribution in the box model is calculated based on an asymptotic carbon isotopic signature of methane, which inevitably includes the entire methanogenesis zone (*i.e.*, from within and outside the model frames). The excess ME estimated by the box model also leads to the conclusion that no or very little external methane source is required (*i.e.*, $R_{ME}+R_{CR}$ is always greater than R_{AOM} in Table 3-5 from Hong et al., 2013). This inference results from the fact that external methane flux is already included in the ME rate estimated by the box model, since it includes the entire methanogenesis zone. In contrast, only the 10-15m of the methanogenesis zone is considered by the kinetic model. Such overestimation of ME rate may be avoided by using isotopic signatures that include only the depth of interest, when available.

In summary, the box model approach can provide satisfactory estimates of the aqueous redox reactions (AOM and CR), but underestimates the significance of organic matter degradation. Therefore, it provides only a semi-quantitative picture of the reaction network around the SMTZ. It is useful when a crude understanding is required or the available data is limited. Our kinetic model is more advanced in that it takes all the concentration profiles into consideration and provides more accurate estimation of the reaction rates, as well the location where reactions occur.

3.5.5 Model experiment result

To develop an understanding of the change that a system experiences when subjected to an increase in bottom methane supply, we allowed the model to evolve from the current concentration and isotopic profiles of the non-chimney site UBGH2-1_1 to the conditions observed at the chimney site UBGH2-3. In addition to the forced increase in bottom methane supply that characterizes chimney locations (Figure 3-8a, 3-8b, and 3-8c), two other modifications are required to accurately account for the observations. First, the simulation necessitates a larger AOM kinetic constant, which indicates that at high methane flux sites there is a higher microbial activity. Second, when there is more methane delivered externally to the system, more organic matter is subject to the degradation through ME rather than POCSR, due to the shoaling of the SMTZ.

If only the strength of external methane source is increased, the AOM rate calculated for the non-chimney sites is not able to keep up with the flux of methane from the bottom supply, and the model will yield an erroneous result of a high methane concentration in the sulfate reduction zone. With a higher AOM kinetic constant methane is now exhausted in the sulfate reduction zone faster and SMTZ becomes shallower. This 2-orders-of-magnitude higher AOM rate (Figure 3-8d and 3-8e) is in agreement with the higher concentration of methyl coenzyme M reductase (mcrA) observed at chimney sites relative to the non-chimney sites (KIGAM, 2011; Choi et al., 2013). Wegener and Boetius (2009), who studied the response of AOM strength to changes such as an increase of methane flux or fluid flow in a flow-through simulator, also observed the timely response in AOM rate to an increase of methane supply.

If only a high AOM rate fueled by the high methane flux is considered, the pH and carbon isotopes resulting from this enhanced reaction rate will not match our observations. A good fit to the data is obtained by increasing the decomposition rate of organic matter through ME rather than POCSR (Figure 3-8f). This is consistent with the fact that a shallow sulfate reduction zone will limit the extent of POCSR, since the organic matter will not spend enough time in that redox zone before burial in sediments devoid of sulfate, where it is then available for ME. Collectively, these changes (lower CR to AOM ratios and higher ME rates), are responsible for the

isotopically lighter DIC and heavier methane observed in the SMTZ region of the chimney sites relative to the non-chimney sites (Figure 3-3).

This shift in the organic matter degradation pathways (from POCSR to ME) intuitively suggest a positive feedback to the high methane flux systems. However, due to the difference in response time between the dissolved and solid phases, such positive feedback is limited. As the external methane flux is enhanced, driven by changes in state of the deep gas reservoirs (*e.g.*, gas hydrate, pore pressure, seismicity etc), the SMTZ rapidly migrates upwards and adjusts itself to a new position, determined by the strength of the external methane flux. Such adjustment is complete in couple thousand years (2 kyr in our experiment), depending on the attendant sedimentation rate (*i.e.*, less time required if sedimentation is higher). With the sedimentation rate (5.6×10^{-5} m/yr) assigned in our model, only ~10 cm of sediments will be buried during this time. However, due to the shoaling of SMTZ, more sediment is now exposed to the attack by ME. The carbon isotopic data and pH will begin to reflect the increase in ME rate after 2 kyr. The depth of SMTZ also slightly decreases in this stage (~10 cm). Due to the lower ME rate relative to the AOM rate, it takes in the order of 10^4 years (50 kyr in our experiment) for the system to reach steady state.

3.6 Conclusions

Our kinetic model can successfully reproduce the compositional and isotopic profiles observed at the eight UBGH2 drilled sites. Striking differences in the biogeochemical processes between the chimney and non-chimney environment were revealed and illustrated in Figure 3-9. As a result of the study, we conclude the following:

1. Organic matter that is buried in a non-chimney environment is degraded in the 6-8 m thick sulfate reduction zone through POCSR, and is responsible for the majority of the DIC production in the pore water. This process consumes 40-65% of the sulfate inflow from the seafloor while the rest of sulfate reacts with the methane from beneath the SMTZ. 19-33% of the AOM is mediated by the methane produced internally through CO_2 reduction which utilizes the hydrogen gas produced from pyrite formation. Methane produced by organic matter

degradation through ME can also account for 8.2-35% of the AOM rate. External methane pool contributes less than 65% of the total AOM rate in all non-chimney sites.

2. In contrast, the strong external methane inflow dominates the consumption of sulfate and production of DIC through AOM in the chimney sites. Organic matter degradation becomes less important. While most (67-95%) of the organic matter is degraded through POCSR in the non-chimney sites, more organic matter (56-~100%) is now degraded through ME at the chimney sites due to the shoaling of sulfate reduction zone (*i.e.*, a thinner SMTZ). Our model experiment demonstrates a different response time between pore water and solid species. The depth of SMTZ rapidly responds to the increase of bottom methane flux, in the order of several thousand years, while the mode of organic matter degradation responds to such shift much slower, *i.e.*, in the order of several tens of thousand years afterward. Such difference in response time precludes a positive feedback triggered by the increase in methane produced through ME in high methane flux settings.

From this model assessment, we conclude that the observed difference in carbon isotopic signatures between high and low methane flux conditions around SMTZ (Figure 3-3 and 3-8) is the result of a lower CR to AOM rate ratio and a higher ME reactivity in sites experiencing a higher methane flux.

Both a box model (Hong et al., 2013) and a kinetic model approach provide similar rate estimates for both the aqueous redox reactions (AOM and CR) and the total organic matter degradation (POCSR+ME), though the two models suggest different modes of organic matter degradation. The advantages of the current kinetic model are as follow: reactions can be better formulated based on thermodynamics and kinetic considerations; steady-state assumption is no longer necessary; and fluid advection can be better described. The kinetic model, however, requires more information than the box model, which is not always available.

3.7 Acknowledgements

This project was made possible with the funding support from US Department of Energy, contract numbers: DE-FE0004000 and DOE Award No.: DE-FE0010496. In addition we acknowledge support from Korea Institute of Geosciences and Mineral Resources (KIGAM) (GP2012-026) and the Hanse-Wissenschaftskolleg, Institute for Advanced Study in Delmenhorst, Germany through a fellowship to MT during the spring of 2013.

Figure 3-1 (a) Map of the eight sites drilled during the 2010 Ulleung Basin gas hydrate drilling expedition (UBGH2) used in this study. The three sites drilled on acoustic chimneys (Torres et al., 2011) were plotted in red triangles. (b) Profiles illustrating seismic characteristics of non chimney (UBGH2-1_1) and acoustic chimney (UBGH2-3) sites.

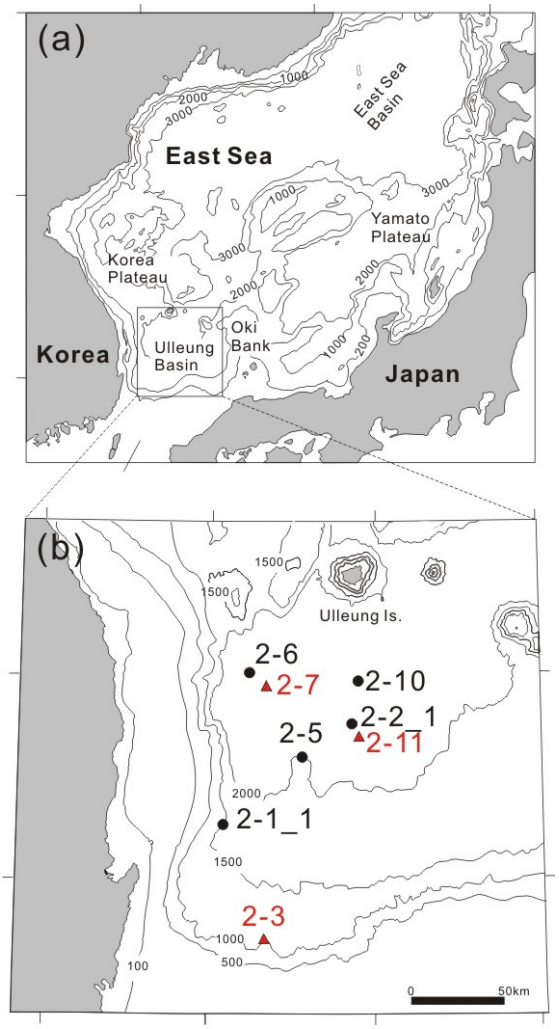

Figure 3-2 : Reaction network considered in our kinetic model. Dissolved species are denoted by yellow boxes and solids are shown in grey. Grey lines and arrows show the input/output of DIC, sulfate, and methane from outside the model domain. The five principal reactions (AOM, CR, POCSR, ME, and CP) are labeled by arrows with different colors. These are the same reactions considered in Hong et al. (2013) and are listed in Table 3-3.

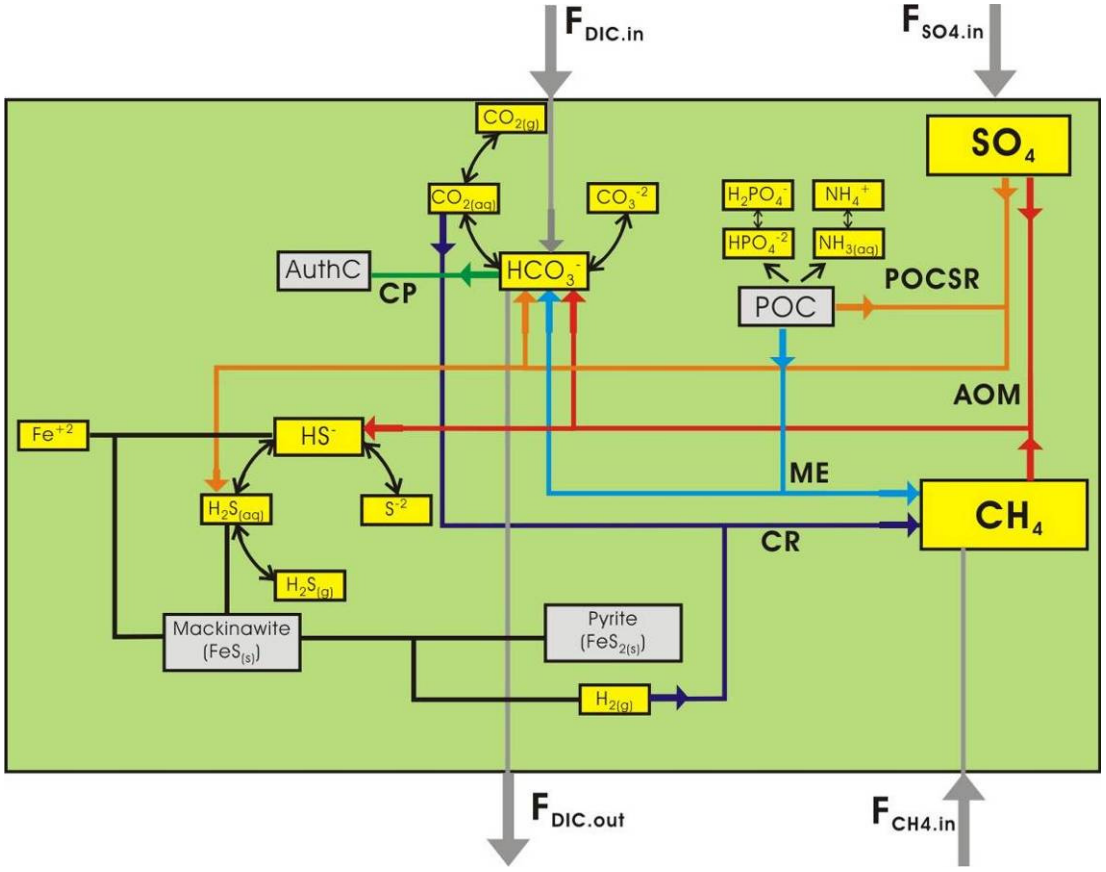

Figure 3-3 Carbon isotopic profiles of dissolved inorganic carbon (DIC) and methane. (a) DIC carbon isotopes from all eight sites investigated. Detailed DIC isotope profiles in the upper 25 meters are plotted in (b) and (c) for chimney and non-chimney sites, respectively. (d) Methane carbon isotopes in the void and headspace gas samples from all sites. (e) The methane carbon isotope for the first 25 m. These DIC and methane carbon isotopic profiles suggest that the fluid source (> 150 mbsf) is not noticeably different in terms of the carbon isotopic signature at all sites. It is the reactions around the SMTZ that cause the observed variation.

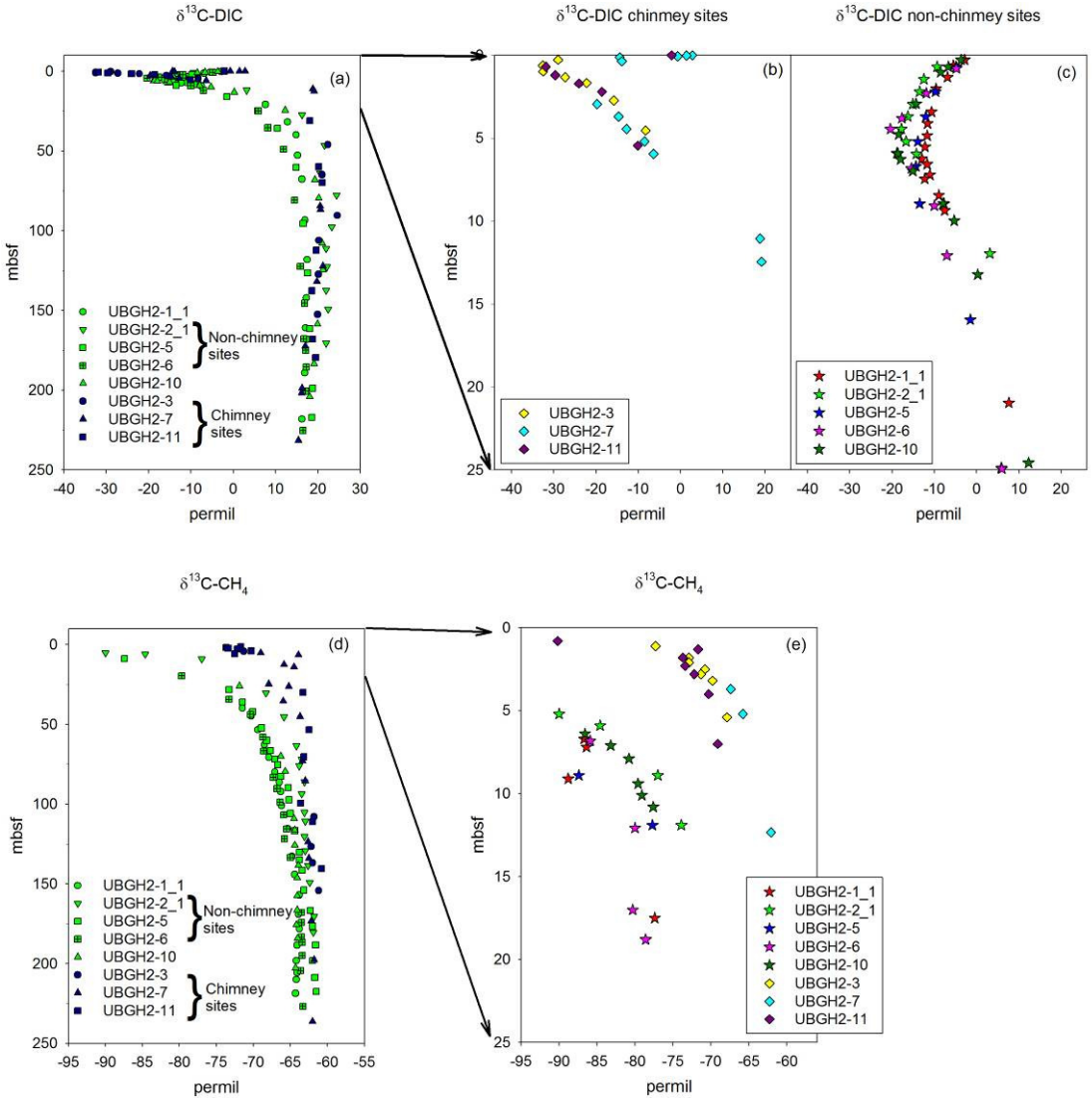

Figure 3-4 Model results for (a) the five non-chimney sites and (b) the three chimney sites, showing good fit to pore water composition and isotopic profiles.

(a)

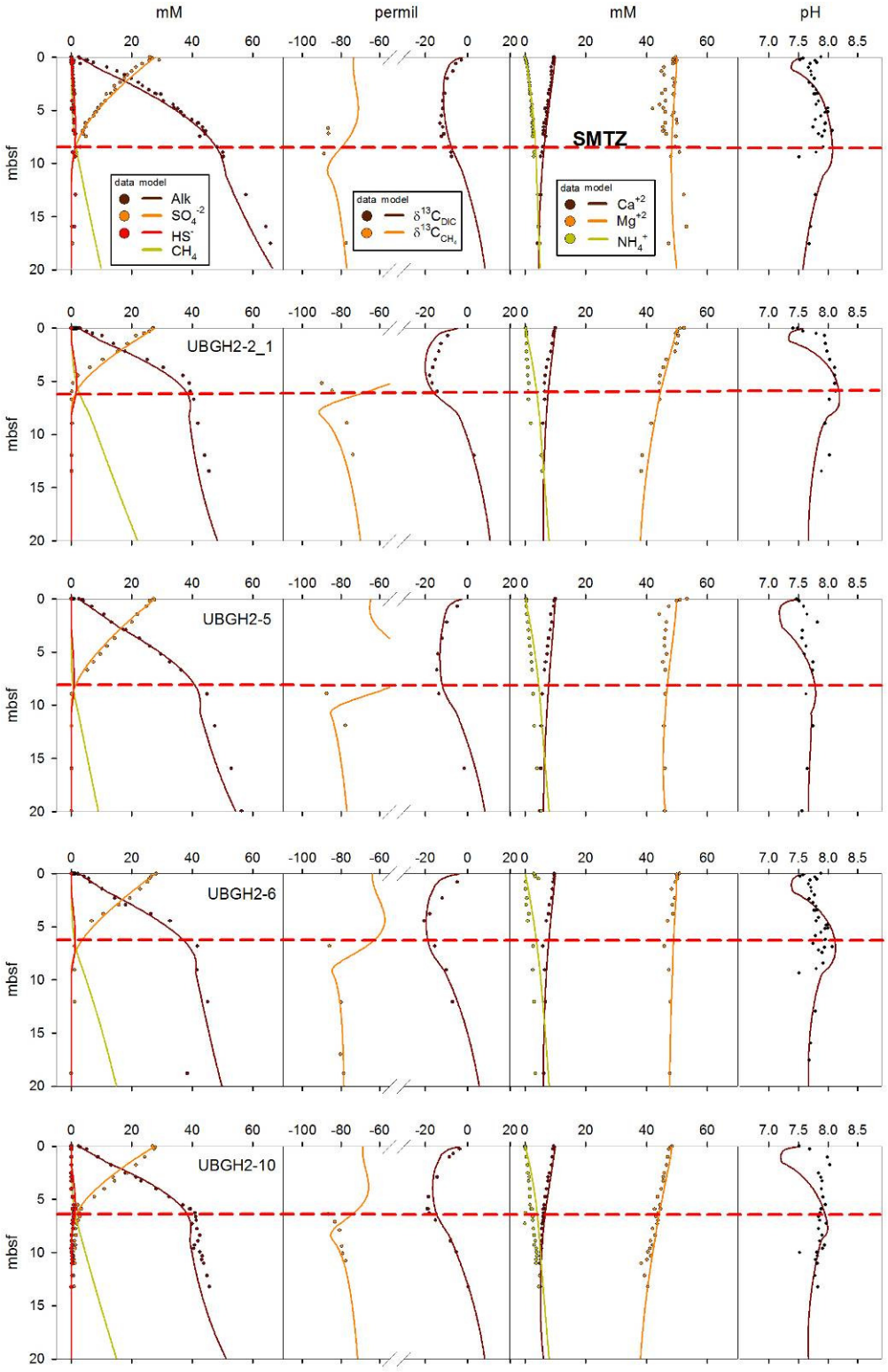

Figure 3-4 (Continued)

(b)

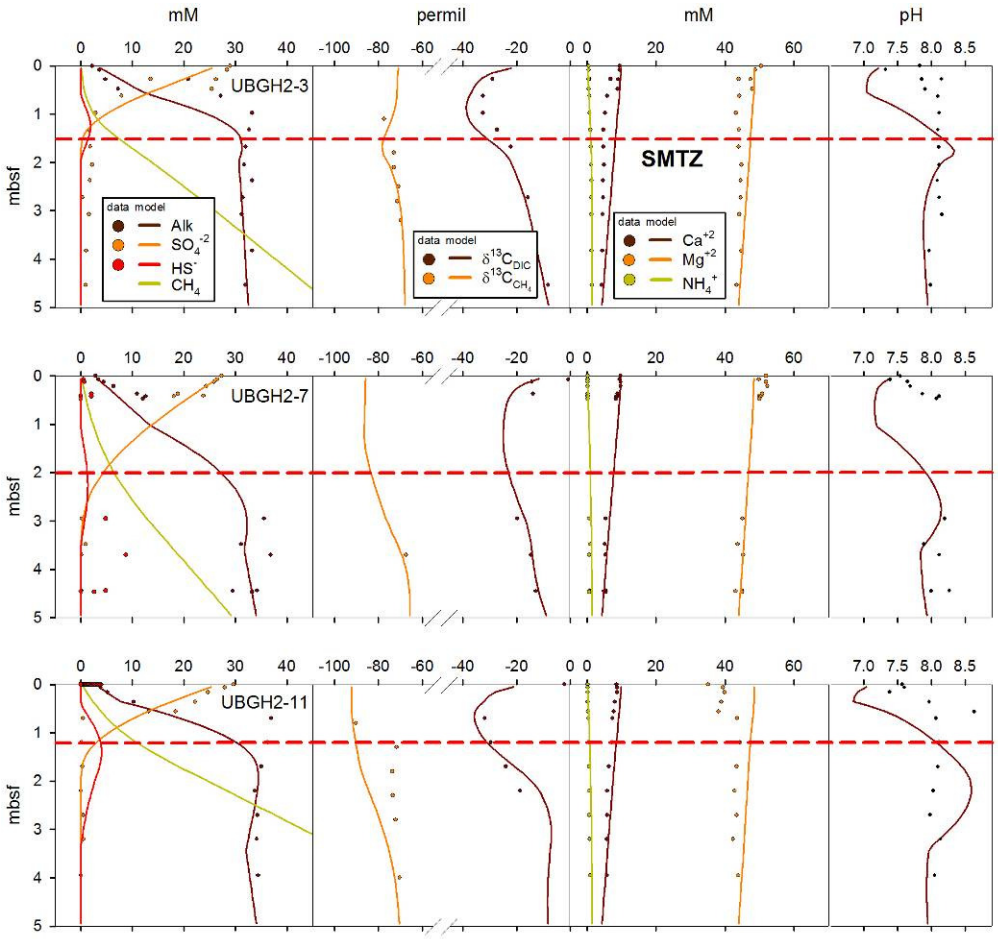

Figure 3-5 Depth-integrated rates estimated from our kinetic model at all sites. Note the different scales between the non-chimney (upper 5 panels) and chimney (lower 3 panels) sites. (a) Rates of the five DIC production/consumption reactions and their percentages relative to the ΔF_{dic}, defined as the flux difference of input and output DIC (negative values represent net outflux). (b) Rates of the three methane sources and their percentages relative to AOM rate. (c) Rates of the four hydrogen sulfide production/consumption reactions and their percentage relative to total hydrogen sulfide production rate (or total sulfate reduction rate, total sulfate influx from seafloor). The very different carbon and sulfur cycles between the chimney and non-chimney sites are apparent from this comparison. See text for details.

(a)

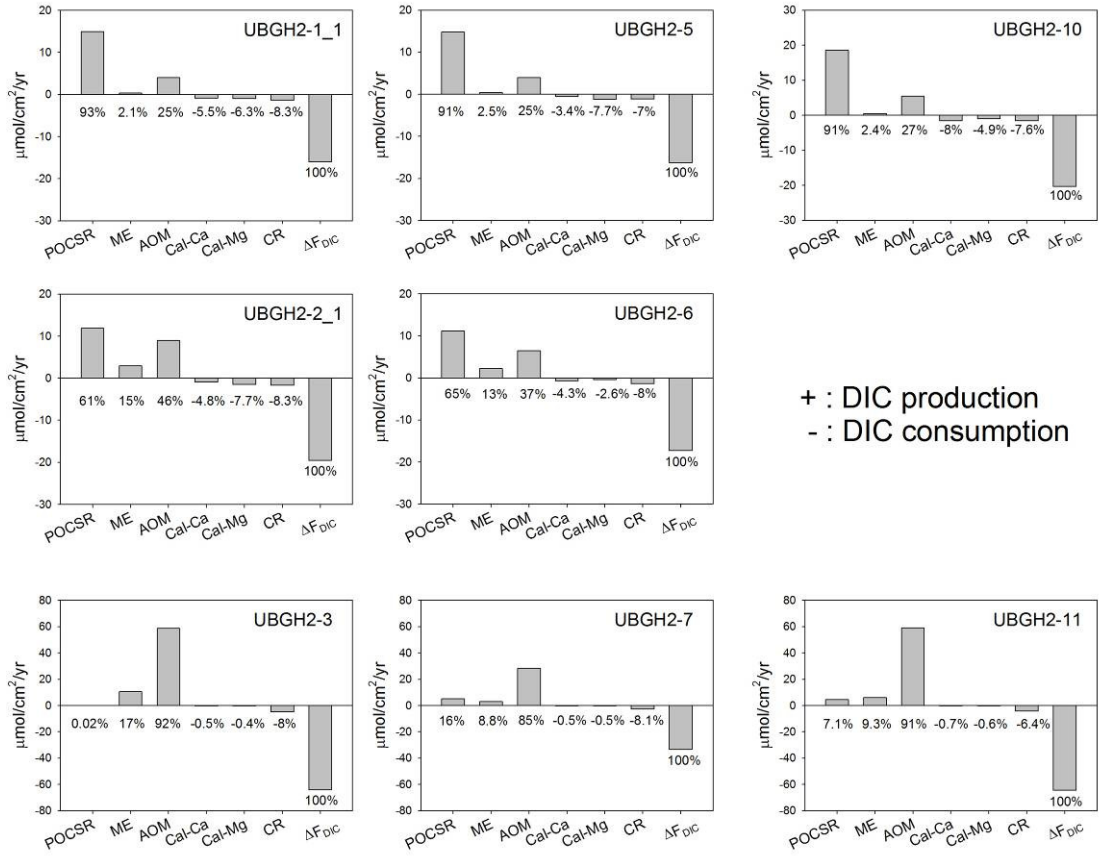

Figure 3-5 (Continued)

(b)

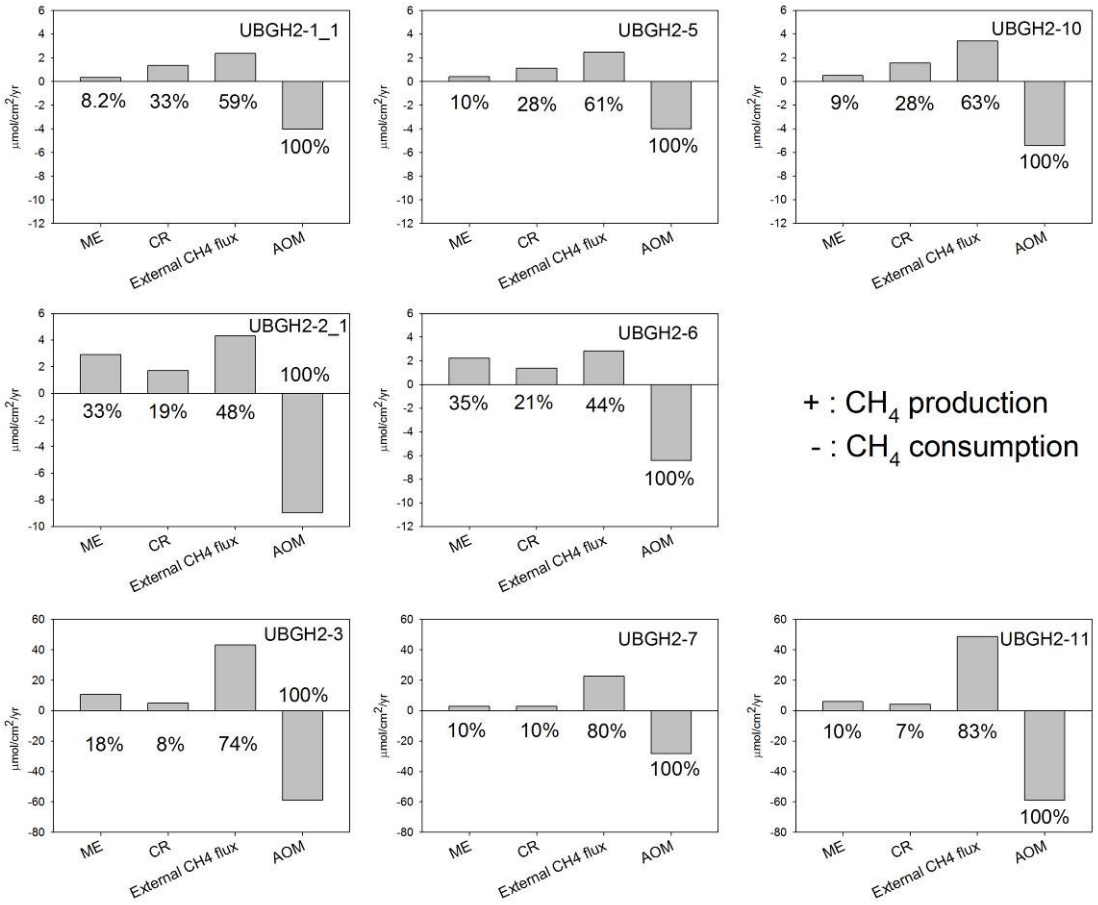

Figure 3-5 (Continued)

(c)

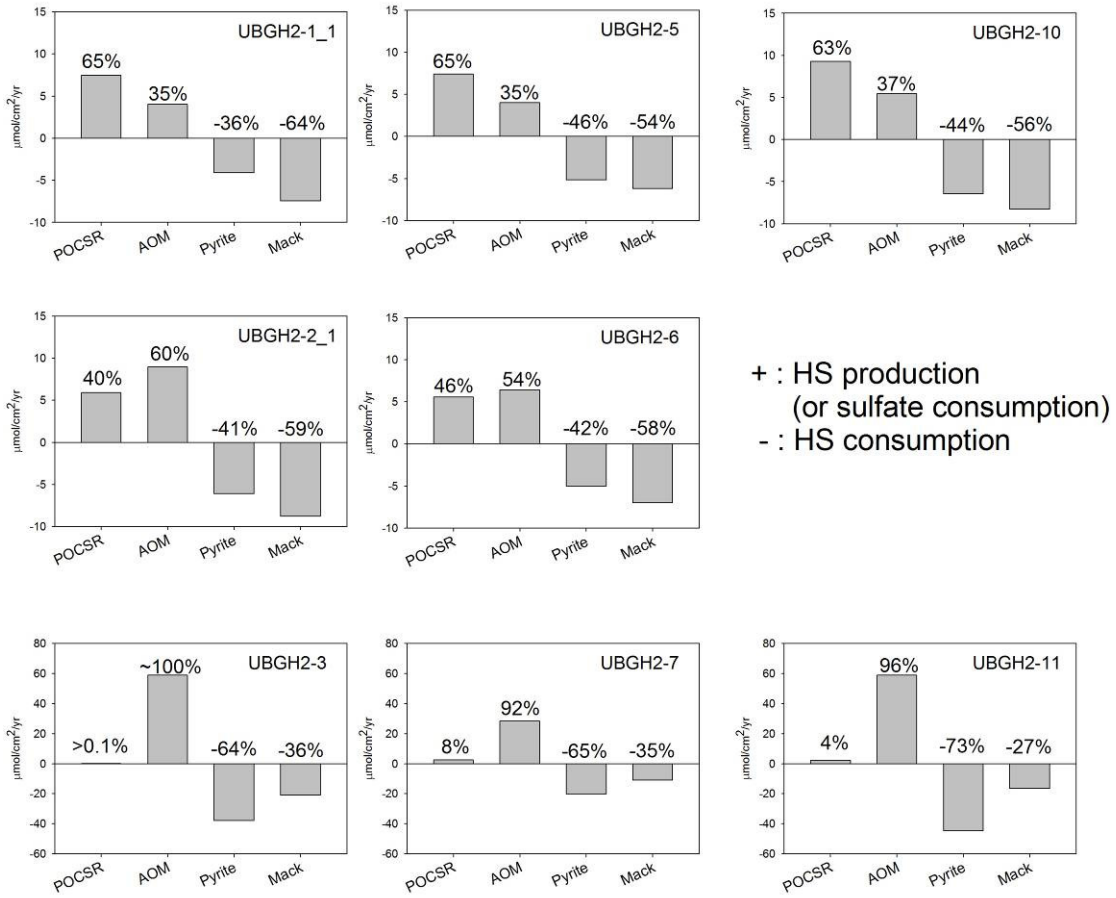

Figure 3-6 Correlations between external methane flux and (a) SMTZ depth and (b) thickness of gas hydrate occurrence zone (GHOZ). Thickness of GHOZ is calculated from the difference between depths of BSR and first gas hydrate occurrence listed in Table 3-2. S The non-linearity in both plots suggests that both the depth of the SMTZ and the thickness of the GHOZ are not solely dependant on the magnitude of an external methane flux. Other factors or processes are may be of the same importance.

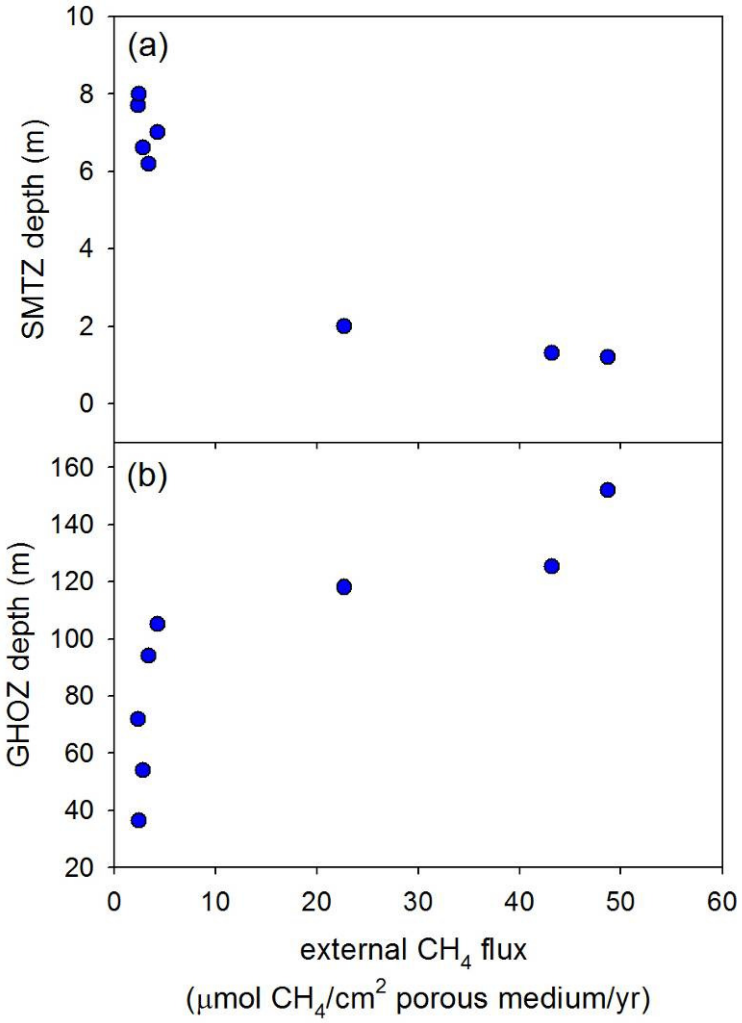

Figure 3-7 Comparisons of reaction rates estimated by the box model (Hong et al., 2013) and the current kinetic model. Error bars show the ranges of box model estimation (the range is smaller than the symbol size for CR and the total OM degradation rate). Both models provide similar estimates for the three rates.

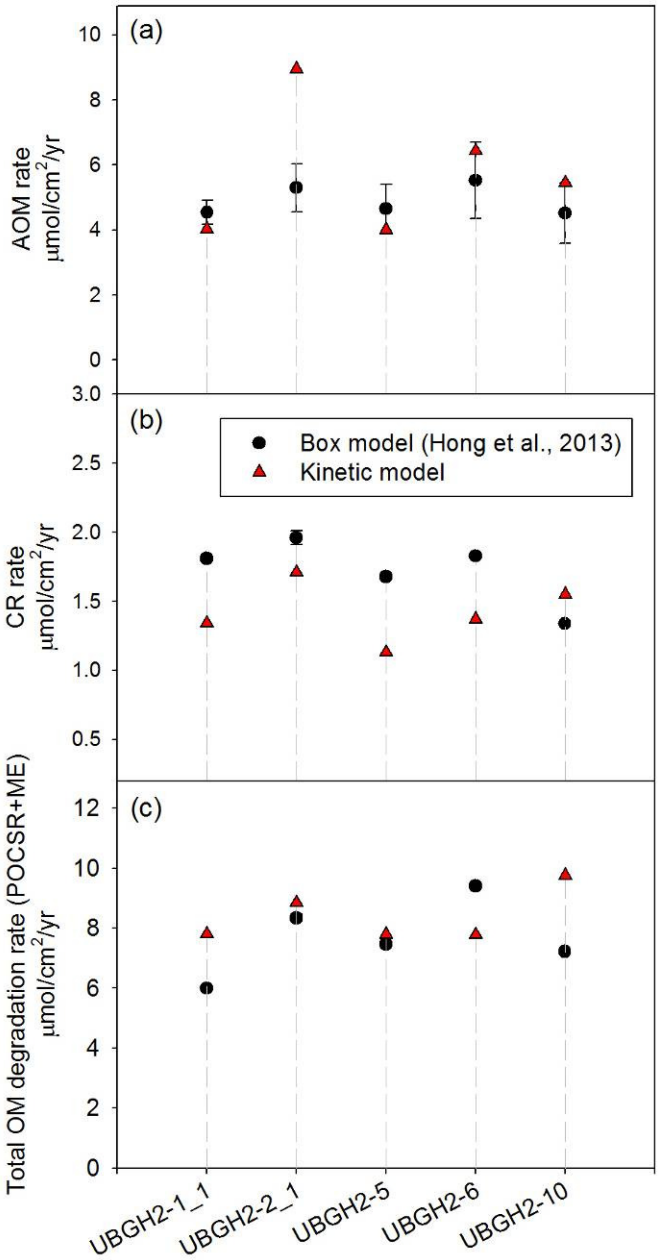

Figure 3-8 Evolution of a system from a low methane flux (red: non-chimney site UHGH2-1_1) to one of high methane flux (blue: chimney site UBGH2-3). In response to an increase in bottom methane supply (17 times larger), the AOM and CR rates increase by two orders of magnitude (note change in x axis scale), but the fraction of AOM fueled by CR drops from 30% in the initial low flux condition to 10% in the final high flux condition. POCSR is the primary organic matter degradation pathway in the initial low flux condition while more organic matter is degraded through ME in the final condition. This change in degradation pathways is related to the shoaling of SMTZ driven by an increase in bottom methane supply and it is an important consideration in estimates of methane-generation potential in marine sediments.

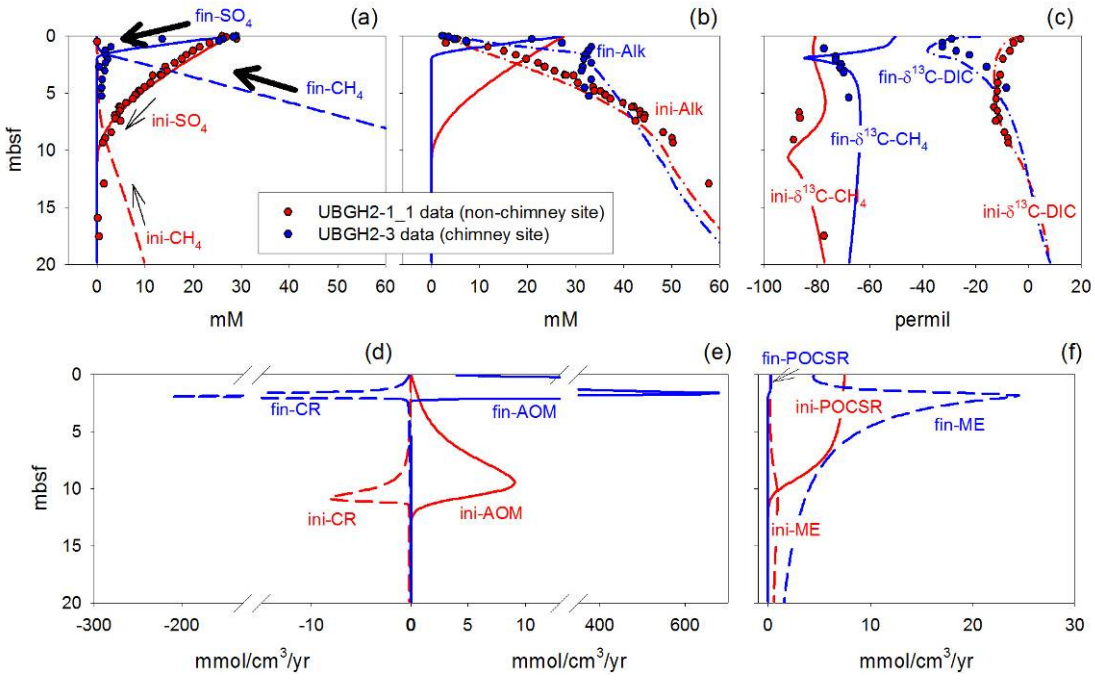

Figure 3-9 Cartoon illustrates the different modes of carbon cycling around SMTZ in the (a) non-chimney and (b) chimney environments in the Ulleung Basin. Size of the arrows represent the strength of fluxes or rates. See text for details.

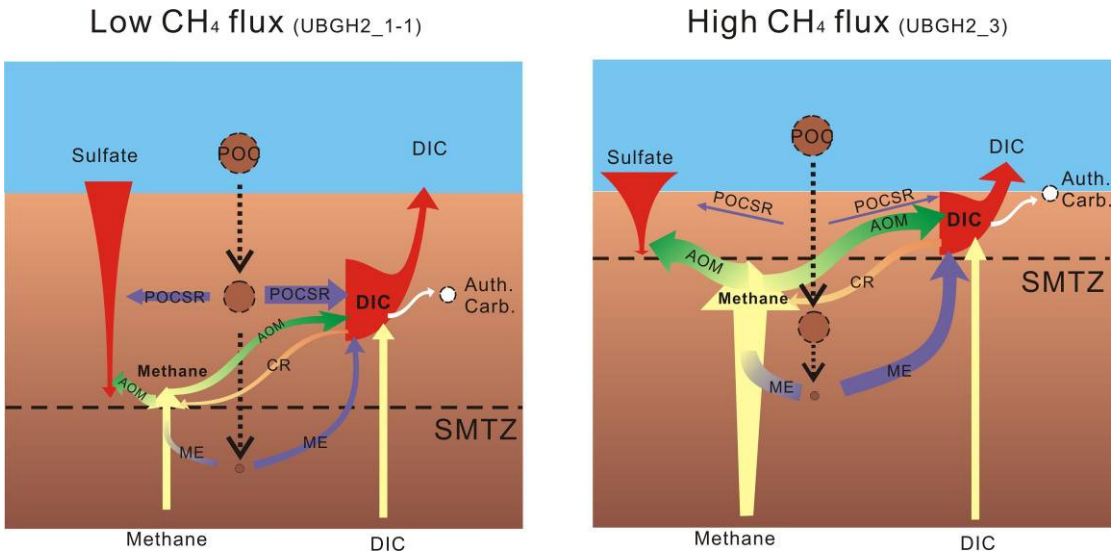

Table 3-1 List of pore water and solid species considered in the model

Primary species	$H^{12}CO_3^-$	$H^{13}CO_3^-$	$^{12}CH_{4(aq)}$	$^{13}CH_{4(aq)}$	NH_4^+
	HPO_4^{-2}	HS^-	SO_4^{-2}	Fe^{+2}	H^+
	$H_{2(aq)}$	Cl^-	Ca^{+2}	Mg^{+2}	Na^+
Secondary species	$^{12}CO_{2(aq)}$	$^{13}CO_{2(aq)}$	$^{12}CO_3^{-2}$	$^{13}CO_3^{-2}$	$NH_{3(aq)}$
	$H_3PO_{3(aq)}$	$H_2PO_4^-$	PO_4^{-3}	$H_2S_{(aq)}$	S^{-2}
Gases	$^{12}CO_{2(g)}$	$^{13}CO_{2(g)}$	$H_2S_{(g)}$	$^{12}CH_{4(g)}$	$^{13}CH_{4(g)}$
Minerals	Calcite-Ca	Calcite-Mg	CH_2O	Pyrite	Mackinawite

Table 3-2 Site-specific information

	BSR (mbsf)	First GH appearance depth (mbsf)	SMTZ depth (mbsf)	POC min/ave/max (%)	$\delta^{13}C_{DIC\text{-}SMTZ}$ (‰)	$\delta^{13}C_{DIC\text{-}BOT}$ (‰)	$\delta^{13}C_{CH4\text{-}SMTZ}$[a] (‰)	$\delta^{13}C_{CH4\text{-}BOT}$ (‰)	ϕ_0 (%)	ϕ_f (%)	γ	Seafloor temperature (^oC)	Geothermal gradient ($^oC/m$)[d]
UBGH2-1_1	165	93	7.7	0.62/1.93/4.03	-13.0	17.0	-88.8	-64.5	86.5	68.0	-0.05	1.3	0.100
UBGH2-2_1	176	71	7.0	0.31/1.59/3.66	-17.8	22.0	-90.0	-62.0	87.0	65.0	-0.03	1.3	0.108
UBGH2-5	189.5	153	8.0	0.16/1.30/3.91	-14.4	18.5	-87.4	-62.0	87.0	68.0	-0.05	1.3	0.096
UBGH2-6	167	113	6.6	0.09/1.23/4.15	-20.4	17.0	-85.9	-63.3	86.5	68.0	-0.05	1.4	0.112
UBGH2-10	171	77	6.2	0.21/1.40/3.44	-18.9	20.0	-86.6	-64.3	86.7	68.0	-0.05	1.3	0.113
UBGH2-3	131.6	6.2	1.3	0.45/1.50 /3.34	-32.5	20.0	-77.3	-62.0	83.5	57.0	-0.01	3.3	0.095
UBGH2-7	124	6	2.0	0.61/1.56 /3.71	-25.0[b]	15.4	-67.4[c]	-62.0	80.0	62.5	-0.015	1.3	0.171
UBGH2-11	159	7	1.2	0.19/1.64 /5.63	-31.9[b]	19.5	-90.2	-62.0	83.0	65.0	-0.015	1.2	0.120

[a] Carbon isotope measurements is extremely difficult for methane at SMTZ due to the low concentration. Therefore, the lightest value was chosen for approximation.

[b] Good measurement around SMTZ was not possible for this site. An estimated value was provided.

[c] This value is ~2 mbsf below the SMTZ which may not be representative to the value at SMTZ.

[d] From Riedel et al. (2013)

Table 3-3 Full list of reactions considered in the model

(a) Homogeneous reactions		*Abbreviation in Figs. 2-9*	*Eq.#*
Acid-base	$H_2O+{}^{12/13}CO_2 \rightarrow H^{12/13}CO_3^- + H^+$		(10)
	$H^{12/13}CO_3^- \rightarrow {}^{12/13}CO_3^{-2} + H^+$		(11)
	$NH_4^+ \rightarrow NH_{3(aq)} + H^+$		(12)
	$H_3PO_4 \rightarrow H_2PO_4^-$		(13)
	$H_2PO_4^- \rightarrow HPO_4^{-2}$		(14)
	$HPO_4^{-2} \rightarrow PO_4^{-3}$		(15)
	$H_2S_{(aq)} \rightarrow HS^- + H^+$		(16)
	$HS^- \rightarrow S^{-2} + H^+$		(17)
Gas-dissolvent	${}^{12/13}CH_{4(g)} \rightarrow {}^{12/13}CH_{4(aq)}$		(18)
	${}^{12/13}CO_{2(g)} \rightarrow {}^{12/13}CO_{2(aq)}$		(19)
	$H_2S_{(g)} \rightarrow H_2S_{(aq)}$		(20)
Aquatic redox	${}^{12/13}CH_{4(aq)} + SO_4^{-2} \rightarrow H^{12/13}CO_3^- + HS^- + H_2O$	AOM	(21)
	$H^{12/13}CO_3^- + H^+ + 4H_{2(aq)} \rightarrow {}^{12/13}CH_{4(aq)} + 3H_2O$	CR	(22)

(b) Heterogeneous reactions			
Calcite	$(Ca, Mg)\ CO_{3(s)} + H^+ \rightarrow (Mg^{+2}, Ca^{+2}) + (1-a)H^{12}CO_3^- + aH^{13}CO_3^-$	CP	(23)
CH_2O-SO_4	$(CH_2O)_{106}(NH_3)_{16}(H_3PO_4) + 53SO_4^{-2} + 14H^+ \rightarrow 53H_2S + (106-b)H^{12}CO_3^- + bH^{13}CO_3^- + 16NH_4^+ + HPO_4^{-2}$	POCSR	(24)
CH_2O-ME	$(CH_2O)_{106}(NH_3)_{16}(H_3PO_4) + 14H_2O \rightarrow (53-c)^{12}CH_4 + c^{13}CH_4 + (39-d)^{12}CO_2 + d^{13}CO_2 + (14-e)H^{12}CO_3^- + eH^{13}CO_3^- + 16NH_4^+ + HPO_4^{-2}$	ME	(25)
Pyrite ($FeS_{2(s)}$)	Pyrite + $H_{2(aq)} \rightarrow$ Mackinawite + $H_2S_{(aq)}$		(26)
Mackinawite ($FeS_{(s)}$)	Mackinawite + $H^+ \rightarrow Fe^{+2} + HS^-$		(27)
Ammonium adsorption	$NH_4^+ + MX \rightleftarrows NH_4X + M^+$		(28)

Table 3-4 Model input parameters

	UBGH2 -1-1	UBGH2 -2-1	UBGH2 -5	UBGH2 -6	UBGH2 -10	UBGH2 -3	UBGH2 -7	UBGH2 -11
$^{12}k_{max}$ (AOM)	5.00E-5	1.05E-4	1.90E-4	1.00E-04	1.00E-4	2.00E-3	3.00E-4	9.00E-4
$^{13}k_{max}$ (AOM)	3.96E-7	7.92E-7	1.20E-6	7.92E-07	7.92E-7	1.97E-5	2.97E-6	8.91E-6
$^{13}K_{half\text{-}CH4}$ (AOM)	4.00E-5	3.81E-5	3.19E-5	4.00E-05	4.00E-5	4.97E-5	5.00E-5	5.00E-5
$^{12}k_{max}$ (CR)	2.35E-5	5.00E-5	5.00E-5	5.00E-05	5.00E-5	2.00E-3	5.00E-2	5.00E-2
$^{13}k_{max}$ (CR)	2.00E-7	2.73E-7	4.10E-7	3.60E-07	4.00E-7	1.28E-5	1.82E-4	5.00E-5
$^{12}K_{half\text{-}HCO3}$ (CR)	1.00E-2	1.00E-2	1.00E-2	1.00E-02	1.00E-2	1.00E-2	1.00E-2	1.00E-2
$^{13}K_{half\text{-}HCO3}$ (CR)	9.34E-5	6.00E-5	9.00E-5	7.91E-05	8.78E-5	7.00E-5	4.00E-5	1.10E-5
K_{in} (CR)	1.00E-4	5.00E-5	1.00E-5	5.00E-05	5.00E-5	1.00E-5	2.00E-5	1.00E-5
$k_{CH2O\text{-}SO4}$	1E-9.6	1E -9.6	1E -9.6	1E -9.7	1E -9.4	1E -11	1E -9.6	1E -9.4
$k_{CH2O\text{-}ME}$	1E -9.8	1E -9.1	1E -9.8	1E -9.5	1E -9.6	1E -8.1	1E -8.7	1E -8.3
$k_{Calcite\text{-}Ca}$	1E -9.7	1E -9.6	1E -9.7	1E -9.7	1E -9.2	1E -9.4	1E -9.4	1E -9.4
$k_{Calcite\text{-}Mg}$	1E -10.7	1E -10.3	1E -10.3	1E -10.9	1E -10.4	1E -10.4	1E -10.4	1E -10.4
k_{Pyrite}	1E -14.8	1E -14.8	1E -14.8	1E -14.8	1E -14.8	1E -15	1E -18	1E -18
$k_{Mackinawite}$	1E -8.9	1E -8.9	1E -8.9	1E -8.9	1E -8.9	1E -8.9	1E -8.9	1E -8.9
$\delta^{13}C$ of methanogenic CH_4	-75	-75	-75	-75	-75	-55	-55	-55
$\delta^{13}C$ of methanogenic DIC	30	30	30	30	30	50	50	50
$\delta^{13}C_{OM}$	-23	-23	-23	-23	-23	-19	-19	-19
OM content	4	4.5	4	4	5	5.5	5	5
$\delta^{13}C_{CH4}$ lower boundary condition	-77	-70	-77	-78.6	-71.5	-67.9	-65.8	-70.3
$\delta^{13}C_{DIC}$ lower boundary condition	7.6	10.0	7.6	5.0	7.5	-8.0	-8.5	-8.5

Units are as follow: k_{max} in mol/kg water/yr, K_{half} in mol/kg water, K_{in} in mol/kg water, k in mol/m^2/sec, isotopic values in ‰, and OM content in %.

Table 3-5 Values of Gibbs free energy used to calculate the equilibrium constants of AOM and CO_2 reduction (source: Benjamin, 2002).

Species	G_f^0 (kJ/mol)
$CH_{4(aq)}$	-34.39
HCO_3^-	-586.8
$H_{2(aq)}$	17.57
H^+	0
$H_2O_{(l)}$	-237.18
HS^-	12.05
SO_4^{-2}	-744.6

Table 3-6 Depth integrated rates for all study sites

(A) μmol DIC/cm^2 porous medium/yr

	UBGH2-1_1	UBGH2-2_1	UBGH2-5	UBGH2-6	UBGH2-10	UBGH2-3	UBGH2-7	UBGH2-11
Cal-Ca	-0.9	-0.9	-0.6	-0.7	-1.6	-0.3	-0.2	-0.5
Cal-Mg	-1.0	-1.5	-1.3	-0.4	-1.0	-0.3	-0.2	-0.4
POCSR	14.9	11.9	14.8	11.1	18.5	0.1	5.2	4.6
ME	0.3	2.9	0.4	2.2	0.5	10.7	2.9	6.0
AOM	4.0	9.0	4.0	6.4	5.5	58.8	28.3	58.9
CR	-1.3	-1.7	-1.1	-1.4	-1.6	-4.9	-2.7	-4.1
DIC flux	-16.1	-19.6	-16.3	-17.2	-20.3	-64.1	-33.4	-64.5

(B) μmol CH_4/cm^2 porous medium/yr

	UBGH2-1_1	UBGH2-2_1	UBGH2-5	UBGH2-6	UBGH2-10	UBGH2-3	UBGH2-7	UBGH2-11
ME	0.3	2.9	0.4	2.2	0.5	10.7	2.9	6.0
AOM	-4.0	-9.0	-4.0	-6.4	-5.5	-58.8	-28.3	-58.9
CR	1.3	1.7	1.1	1.4	1.6	4.9	2.7	4.1
CH_4 flux	2.4	4.3	2.5	2.8	3.4	43.2	22.7	48.7

(C) μmol HS^-/cm^2 porous medium/yr

	UBGH2-1_1	UBGH2-2_1	UBGH2-5	UBGH2-6	UBGH2-10	UBGH2-3	UBGH2-7	UBGH2-11
Pyrite	-4.9	-6.1	-5.2	-5.0	-6.5	-37.9	-20.1	-44.6
Mack	-7.4	-8.8	-6.2	-7.0	-8.3	-20.9	-10.8	-16.6
POCSR	7.5	5.9	7.4	5.6	9.3	0.1	2.6	2.3
AOM	4.0	9.0	4.0	6.4	5.5	58.8	28.3	58.9
Tot SO_4 reduction	11.5	14.9	11.4	12.0	14.7	58.9	31.0	61.2

CHAPTER 4

A kinetic-model approach to quantify the effect of mass transport deposits on pore water profiles in the Krishna-Godavari Basin, Bay of Bengal

Wei-Li Hong, Evan A. Solomon, Marta Torres

Marine and Petroleum Geology

in review

4.1 Abstract

Mass transport deposits (MTDs) in the Krishna-Godavari Basin from the eastern Indian margin are common sedimentary features over the modern continental slope. Quantitative understanding of the scale and age of these MTDs is relevant to understanding their triggering mechanisms and environmental feedbacks, as well as for interpreting pore water chemical profiles. Pore water profiles in sediments recovered during the 2006 Indian National Gas Hydrate Project (NGHP-01) expedition suggest that MTDs are present at seven of the ten sites cored in the Krishna-Godavari Basin. Kinetic modeling of the S-shaped pore water sulfate and ammonium profiles from these sites provides quantitative estimates of the individual MTDs thickness, time elapsed after the event, rate of organic matter-fueled sulfate reduction, and time required to reach a new steady state. Model results suggest that the MTDs at the seven study sites are 8 to 25 meters thick and are 300 to 1600 years old. Within the MTD sections, the organic matter-fueled sulfate reduction rates are 130 to 1200 mmol/m^2/yr and the time needed to reach a new steady state ranges from 2000 to 3800 years. In comparison to depth-integrated sulfate reduction rates estimated in other regions, our estimates are relatively high reflecting a much thicker sulfate reduction zone that results from the MTDs. A positive correlation is observed between water depth and the sedimentation rate in the MTD sections (i.e., thickness of MTD divided by its age), which agrees with previous studies of MTDs in this region. Our results confirm the remarkable influence of transient MTDs on pore water profiles. Any inference of metabolic processes and quantification of their steady-state reaction rates should take such effect into consideration.

4.2 Introduction

The Krishna-Godavari (K-G) Basin on the eastern Indian margin is characterized by extensive mass-transport deposits (MTDs) formed by sliding/slumping of river-delivered sediments (Forsberg et al., 2007; Ramana et al., 2009: Shanmugam et al., 2009; Ramprasad et al., 2011). MTDs in the K-G Basin may be related to variations in regional climate and changes in sediment discharge from the Krishna and Godavari rivers (Forsberg et al., 2007; Ramana et al., 2009; Ramprasad et al., 2011). However, the regional variability, magnitude, and age of the individual events are poorly constrained. Furthermore, sediments deposited by these abrupt events likely alter the pore water geochemical records in the shallow sediments, and hinder development of quantitative models for early diagenetic processes in this margin.

Pore water composition is very sensitive to localized and recent slumping events, as previously shown by Hensen et al. (2003) and Holsein and Wirtz (2010). The pore water profiles sampled during the recent Indian National Gas Hydrate Project (NGHP-01) expedition (Figure 4-1) provide a unique opportunity to quantify the timing and magnitude of these deposits. In this study, we apply a transport-reaction model to pore water data from seven sites drilled in the K-G basin (Table 4-1) to quantify the thickness of the deposits and the time elapsed after each event. This information is potentially important for future studies focusing on the control and/or feedback mechanisms of these episodic sediment transport events. Our work also highlights the importance of these events on the shape of pore water solute profiles and on their interpretation.

4.3 Study region

The modern K-G Basin in the eastern passive margin basin of India receives large sediment inputs from the Krishna and Godavari Rivers. The delta fronts exhibit MTDs, scars and irregular topography over the modern upper continental slope formed by sliding/slumping (Forsberg et al., 2007; Ramana et al., 2009; Ramprasad et al., 2011). Sediments transported through large canyons also contribute to the total sediment accumulations (Kotha, 2002; Bastia, 2004; Murthy, 1999). Recent seismic and

bathymetric surveys in this area imaged widespread MTDs (Solheim et al., 2007; Forsberg et al., 2007; Shanmugam et al., 2009; Ramprasad et al., 2011), and were used to guide drilling during the NGHP-01 expedition in 2006.

Sediment thickness in the K-G basin varies from 3 to 5 km and may exceed 8 km in the offshore region (Prabhakar and Zutshi, 1993). Drilling during NGHP-01 sampled the upper 200-300 meters at 10 sites, aimed at characterizing the gas hydrate potential of this region (Figure 4-1). In this study, we focus only on the first 40-60 meters of the sediment column (Table 4-2), in an effort to unravel the relative magnitude and age of MTD events, as their effect on pore water profiles impact ongoing efforts to quantify organic carbon cycling and methane dynamics in this passive margin (Solomon et al., 2014). The sediments studied all correspond to the same Quaternary lithostratigraphic unit primarily composed of clay with variable amounts of carbonates (4-60%), and trace amounts of quartz, feldspar, mica, and iron sulfide (Collett et al., 2008). Frequent silt/sand beds are observed at each site (Collett et al., 2008). The distribution of authigenic carbonate is not necessarily correlated with the current sulfate-methane-transition-zone (SMTZ), defined by the pore water sulfate and methane profiles, suggesting migration of the SMTZ in the past (Collett et al., 2008) or simply burial of authigenic carbonates produced at the SMTZ through time, perhaps punctuated by sediment slumping.

4.4 Effect of MTDs on the pore water data

Shipboard pore water analyses, including sulfate concentration, were reported in Collett et al. (2008). Shorebased pore water ammonium analyses were reported in Solomon et al. (2014). Pore water profiles in seven of the 15 sites drilled in the K-G Basin suggest a non-steady-state condition (Figure 4-2). The concentration of all pore water species, especially sulfate, at these seven sites changes rapidly over relatively short depth intervals, indicating the importance of non-diffusional processes. A rapid drop in sulfate content and the concordant increases of both ammonium and dissolved inorganic carbon (DIC) concentrations at the first ~5 meters in the sediments (Collett et al., 2008; Solomon et al., 2014) are indicative of sulfate consumption due to organic matter degradation

(abbreviated as POCSR, particulate organic carbon sulfate reduction, hereafter). As no methane is present in this interval, POCSR should be the only reaction consuming sulfate. Between 15 to 25 meters below seafloor (mbsf), sulfate content remains constant until it is again consumed by methane through anaerobic oxidation of methane (AOM) and POCSR at greater depths (Figure 4-2). We hypothesize that these sulfate profiles reflect recent mass transfer events at each site, and that the MTD too recent for diffusion to smooth the dissolved sulfate distribution between the two sulfate reduction zones.

In this work, we define MTD as a fluidized sediment block whose pore water is well mixed with sea water during sediment transport. The pore water composition in the MTD section is set to be sea water value to reflect the homogenization process. Before a MTD event, sulfate supplied by diffusion from overlying seawater is consumed by both POCSR and AOM, which forms a distinct SMTZ (Figure 4-2A). In environments devoid of MTD these processes act together to generate a smooth decrease in dissolved sulfate with depth (e.g., Claypool and Kaplan, 1974; Froelich et al., 1979; Borowski et al., 1999; Hong et al., 2013; Figure 4-2A). If then a layer of MTD with fresh organic matter tops the original sediment surface (Figure 4-2B), the SMTZ is buried deeper while the reactive organic matter in the newly deposited sediments also consumes sulfate, leading to the shallow-most drop in sulfate content and effectively separating both sulfate consuming processes (Figure 4-2C). This produces the S-shaped profiles observed and clearly indicates that the system is out of steady state. Eventually, the persistent bottom methane supply will move the SMTZ upward until a new steady state is reached (Figure 4-2D). We use a kinetic modeling approach to explore the conditions leading to the S-shape of sulfate profiles from these seven sites to unravel the effects of MTDs on pore water geochemistry.

4.5 Model architecture

4.5.1 Reaction formulation

In these simulations we use the FORTRAN routine CrunchFlow, as described in Steefel (2009). Hong et al. (2013; 2014) has listed the various reactions involved around the

SMTZ, among which we focus only on POCSR and AOM. Above the SMTZ, where there is no methane present, POCSR is responsible for all of the sulfate consumption; AOM becomes more significant closer to the SMTZ. These two reactions can be summarized as:

$$(CH_2O)(NH_3)_{\frac{x}{106}}(H3PO4)_{\frac{1}{106}} + 0.5SO_4^{-2} + (0.01886 - \frac{x}{106})H^+ \rightarrow 0.5H_2S + HCO_3^- + \frac{x}{106}NH_4^+ + 0.00943HPO_4^{-2} \quad (4.1)$$

$$CH_4 + SO_4^{-2} \rightarrow HS^- + HCO_3^- + H_2O \quad (4.2)$$

where x is the stoichiometry of nitrogen in the organic matter and was calculated from the C/N ratio at each site (Table 4-3; data from Phillips and Johnson, 2014). We are aware that such a calculation maybe an oversimplification, as the amount of ammonium released from organic matter degradation depends on the C/N ratio in the pool of reactive carbon instead of the bulk organic matter. However, the good agreement with the NH_4 data, as we will show later, indicates that this is still a reasonable approximation.

In order to constrain the rate of organic matter degradation in the first sulfate reduction zone (Figure 4-2C), we simulate pore water ammonium, which can be described as a function of both organic matter degradation and ion exchange on mineral surfaces (Von Breymann et al., 1988a, 1988b, 1990; Wallmann et al., 2006; 2008). To formulate ion exchange with CrunchFlow, we chose the *Gaines-Thomas* activity convention and specify a cation exchange capacity for the bulk sediment. Solid density is calculated based on the sum of mineral volume fractions. In the K-G Basin, ~80-90% of the sediment is composed of clay minerals (Collett et al., 2008), ~50-80% of which is smectite (Venkatarathnam and Biscaye, 1973; Pattan et al., 2008; Underwood, pers. comm.). Using a CEC for smectite of 80-150 meq/100 g of sediment (Hang and Brindley, 1970; Jaynes and Bigham, 1986), we estimated the CEC of K-G Basin sediments to range

from 32 to 80 meq/100 g of sediment. The values used at each site were further constrained by data fitting using pore water measurements, and are specified for each site in Table 4-2.

POCSR was formulated as a Monod-type reaction with one Monod term (half saturation constant of 100 μM for sulfate was adopted; Wegener and Boetius, 2009). AOM was formulated as a double-Monod-type kinetic reaction with (half-saturation constants of 500 μM were used, Wegener and Boetius, 2009). Detailed formulation for the reactions is given in Hong et al. (2014). The *Dirichlet*-type boundary conditions were used for all species, including methane. A fixed concentration of methane was assigned at the bottom of the simulation frame at each site (L in Figure 4-2 and Table 4-2). This concentration is constrained by the observed methane and sulfate profiles as this bottom supply of methane induces AOM at a rate, together with POCSR, that leads to the observed methane and sulfate profiles. It is important to notice that the observed methane concentration can only partly constrain (i.e., as minimum constraint) the model, as the shipboard measurements of gas concentrations are impacted by degassing during core recovery.

4.5.2 Model logistics

The sediment depth modeled (L in Figure 4-2) varies from site to site and was determined based on its dissolved sulfate profile (Table 4-2). In order to constrain the thickness of each MTD (Δx in Figure 4-2B) and the time elapsed since deposition (Δt_1 in Figure 4-2C), we evolved the model simulation in two steps. In the first step (Figure 4-2A), we used bottom seawater composition as the initial condition. We used a sediment deposition rate at all sites of 0.15 meter per thousand years, based on estimates listed in Collett et al., (2008) and Mazmudar et al. (2009). Giosan (pers. comm., 2009) has reported variations in sedimentation rates among the different sites ranging from 0.15 m/kyr at Site 10 to 0.85 m/kyr at Site 5. A range of sedimentation rates was therefore used to test its influence on the model results. We observed no significant effect when varying sedimentation rates from 0.15 to 0.85 m/kyr, which is not surprising since the time scale

considered in this study is only on the order of several thousand years. The time length for the first step was calculated by dividing the modeled depth of each sediment column, L, by the sedimentation rate of 0.15 m/kyr. The resulting time spans (200 to 400 kyrs) are long enough for sulfate profiles to reach steady state. The assigned reactivity for organic matter and minerals (e.g., calcite and pyrite) were kept constant among all sites. We adjusted bottom methane flux to match the observed sulfate and methane gradients at the lower sections of the profiles. After this time span, when the system has reached steady state, we add an instantaneous sediment layer with a thickness denoted as Δx (Figure 4-2B).

The second step of model was initiated from the steady state conditions and SMTZ depths established during the first step with a new instantly deposited layer of sediments (i.e., the MTD) bearing fresh and reactive organic matter and sea water sulfate content of 28 mM (Figure 4-2B). From these initial conditions, we let the model evolve until it fits the observed pore water profiles. The thickness of this organic matter-rich layer (Δx in Figure 4-2B) can be estimated by simulating the pore water sulfate profiles. The amount of time required to reach the current observed profile (Δt_1 in Figure 4-2C) provides an indication of the time spanned since the MTD at each site. The assigned bottom methane supply was kept constant between the two steps.

4.5.3 Porosity, formation factor, and formation temperature

Diffusion rates of sulfate and ammonium are the most important parameters in this model assessment. To provide a realistic estimate of the diffusion rates, the porosity, tortuosity and the in-situ temperature of sediments need to be thoroughly considered. The porosity profile at each site was obtained by fitting the observed profiles (Collett et al., 2008) with the equation for depth-dependent porosity (Boudreau, 1997):

$$\phi(z) = \phi_f + (\phi_0 - \phi_f)\exp(\gamma z) \quad (4.3)$$

where ϕ_f and ϕ_0 are the asymptotic porosity and porosity at the water-sediment interface, respectively. γ is an empirical constant obtained from data-fitting of the depth interval that covers the modeled depth (i.e., L in Figure 4-2). The best fitted parameters are reported in Table 4-2.

In order to account for the different diffusivities of solutes in pure fluid and porous media, a tortuosity value is required to adjust the diffusion coefficients in non-porous medium. One way to quantify the effect of tortuosity is by calculating the formation factor (FF) from a resistivity log data. Logging of the electrical resistivity tracks the electrical current, which is assumed to be analogous to fluid transport, in the porous medium. In CrunchFlow, this can be included by providing a parameter named cementation factor (*m*). This value can be calculated using the FF data calculated from resistivity logs obtained from logging while drilling (LWD) and shipboard laboratory measurements with a four-pin Wenner array and a temperature probe (Collett et al., 2008). The *m* values calculated for each site through Archie's law (Steefel, 2009):

$$FF = \phi(z)^{-m} \quad (4.4)$$

and are listed in Table 4-2.

In-situ temperatures were measured at each site during coring operations with the APCT-3 (advanced piston corer temperature tool 3) (Collett et al., 2008). Several temperature measurements, which include seafloor temperature, were made at each site to determine the geothermal gradient. This information is also included in Table 4-2.

4.5.4 Sensitivity tests

We performed a sensitivity test to constrain the variability of Δx, Δt_1 and k_{OM} using data from Site 5C. Δx and Δt_1 are primarily estimated with the sulfate profile whereas k_{OM} was estimated with both sulfate and ammonium profiles. In this exercise we used the best fit

values for Δx, Δt_1 and k_{OM}, which are 13m, 1600 years and $10^{-9.3}$ mol/m^2/sec (blue lines in Figure 4-3), and run the model by varying these parameters from 8 to 18m (Figure 4-3A), 1300 to 1900 years (Figure 4-3B) and from $10^{-9.5}$ to$10^{-9.1}$ mol/m^2/sec (Figure 4-3C). The results of this exercise indicate that our model is able to estimate the three parameters with good sensitivity and therefore provide a reliable quantification of the magnitude and timing of the most recent MTDs, as well as provide information on the k_{OM} in KG basin sediments.

4.6 Results and discussion

4.6.1 Model-estimated MTD scale and age

Our model assessment, in light of the geological background of this area, confirms our hypothesis that the S-shape sulfate profiles result from organic matter degradation driven by a rapid and recent input of fresh organic matter associated with MTDs. Our model reproduces the observed sulfate and ammonium profiles at the seven sites where sulfate profiles indicate that the system is out of steady-state (Figure 4-4). The MTD thickness (Δx) and the time elapsed (Δt_1) since the mass transfer event are summarized in Table 4-3. We also ran the model until it reached a new steady state after the MTD event (Figure 4-2D) to estimate the maximum time the anomalous sulfate profiles can survive (Δt_2). These values were listed in Table 4-3 as well.

The thickness of the MTDs estimated from the model ranges from 8 to 25 meters. Seismic profiles at Sites 10 and 12 image a shallow debris flow (Collett et al., 2008), which supports our results, although the resolution is different from what we infer here (<25 m). High resolution multibeam bathymetry profiles also document prevalent and widespread distribution of mass transfer deposits in the upper and midslope areas of the K-G basin (Ramprasad et al., 2011) with a thickness similar in magnitude to what we estimated with our model. Frequent observations of silt/sand laminae in the cores were also attributed to the influence of MTDs in the basin (Collett et al., 2008). However, our

results show no correlation between the magnitude of the model-derived Δx and the frequency of laminae (Figure 4-4), suggesting processes other than MTD may have led to the formation of these laminae.

Using ^{14}C dating, Ramprasad et al. (2011) estimated the sediment deposition rate in one MTD to be 40 m/kyr, which is much faster than the sedimentation rate for the other hemipelagic sequence in their study (2.1 m/kyr). ^{14}C dating from Mazumdar et al. (2012) also revealed a dramatic change in sedimentation rate between two deposition modes (i.e., hemipelagic sediment rain vs. MTDs). We can estimate an average deposition rate for each mass transfer event by dividing the thickness of the MTD by the time elapsed since deposition ($\Delta x/\Delta t_1$) (Table 4-3). Our values are similar to those of Ramprasad et al. (2011) and similar or higher than those of Mazumdar et al. (2012). We also observe a positive correlation between the average deposition rate of each mass transfer event with water depth (Figure 4-5), if we excluded Site 15A. This correlation suggests that sites in deeper water receive more sediments than those on shallower sections of the slope, which agrees with the previous observations in this region (Ramprasad et al., 2011).

4.6.2 Sulfate reduction dynamics in the MTD sections

At all sites except for Site 15A, the model is able to reproduce the observed ammonium and sulfate profiles using k_{OM} values ranging from $10^{-9.1}$ to $10^{-9.5}$ moles /m^2/sec. These values result in a depth-integrated POCSR rate (R_{POCSR}), which equals to the total sulfate reduction rate in the MTD section, of 149 to 623 mmol $SO_4^{-2}/m^2/yr$ (Table 4-3). POC (particulate organic matter) degradation rates estimated by Wallmann et al. (2006) from the sediments of the Sea of Okhotsk and Blake Ridge range from 2.8 to 122 mmol $SO_4^{-2}/m^2/yr$. Dale et al. (2008) estimated the organoclastic sulfate reduction rate from the coast of Denmark to be as high as 1150 mmol $SO_4^{-2}/m^2/yr$. Chuang et al. (2013) recently estimated the contribution of sulfate reduction from organic matter degradation to be 4.2 to 47 mmol $SO_4^{-2}/m^2/yr$ in southwestern offshore Taiwan. Hong et al. (2014) estimated the rates of POCSR in the sediments of Ulleung Basin to be in the range of 0.5 to 74.7 mmol $SO_4^{-2}/m^2/yr$. The rates we estimated for the K-G basin are on the high end of these

estimates, which may be due to the fact that we estimated the R_{SR} by integrating over the 8 to 25 m-thick MTD sections. These depth sections are two to five times thicker than the typical thickness of the sulfate reduction zone, which are only a couple meters at these other sites.

The sulfate profile from Site 15A is distinctly different from the other six sites in two ways. First, the first measurement at 1.4 mbsf yielded only 8.27 mM of sulfate (Figure 4-4), which is significantly lower than the bottom seawater value (28 mM). Such low sulfate content together with the low initial porosity measurement (69.75% at 0.78 mbsf, Figure 4-6A) suggests that the top of the sediment column at this site may have been removed by a recent erosional event. Second, the drop of sulfate concentration in the upper 9 m of the hole is more dramatic compared to other sites (Figure 4-4). In order to match the observed, unique sulfate and ammonium profiles at Site 15A, we have to assign a distinctly higher k_{OM} that results in a higher R_{POCSR} (1215 mmol $SO_4^{-2}/m^2/yr$; Table 4-3) at this site. This difference may suggest that the organic matter at this site is more labile than other sites; however, the characterization of organic matter composition and provenance (Phillips and Johnson, 2014) at this site does not support this inference.

Another explanation for the higher R_{POCSR} is that the initial sulfate concentration when MTD deposited at Site 15A was not sea water value as what we assigned in the model (Figure 4-2B). Therefore, a R_{POCSR} similar to other sites and lower initial sulfate content can result in the current pore water profile observed at Site 15A. We hypothesized that the pore water composition of the MTD was unaltered while the sediment deposited at Site 15A. The upper portion of this MTD may continue the down slope transport during the same event or was later removed by another erosion event. The removal of this part of sediments result in the lower porosity currently observed (Figure 4-6A). The remaining sulfate in the intact part of the MTD was consumed by POCSR at a rate similar to other sites (Figure 4-6B). These combined processes result in the different sulfate profile observed at Site 15A (Figure 4-6C). This inference, however, assumes unchanged pore water profiles during mass transport, which does not seem to be very realistic. Although

no satisfactory conclusion is arrived at this point, the combined data reveal the very dynamic conditions at Site 15A.

4.6.3 Influence of MTDs on pore water profiles

Although only sulfate and ammonium profiles are modeled in this study, we expect MTDs to influence the distribution of all pore water species as the entire system is still in a transient state. Therefore, any inferred reaction that assumes a steady state condition will result in erroneous conclusions and rate estimates. For example, our model results question the postulated new metabolic pathway by Schrum et al. (2009). These authors explain the low ammonium concentration observed within the first sulfate reduction zone at Site 14A as indicative of a sulfate-reducing ammonium oxidation reaction. Although their estimates of Gibbs energies for the reaction support the potential role of this metabolic process, our model clearly demonstrates that the sulfate and ammonium profiles of the K-G basin can be well explained by rapid deposition of sediment (Figure 4-2B), and do not necessarily require a sulfate-reducing ammonium oxidation reaction.

S-shape sulfate profiles have been reported by Hensen et al. (2003) in the west Argentine Basin. They explained such profiles as resulting from two independent slides, each of which brought a sediment package with distinct pore water compositions. The different pore water compositions from these two sediment packages, which are also different from the bottom water composition, reflect the different origins of the sediment sections. By numerically simulating this scenario, Hensen et al. (2003) concluded that the sedimentary process leading to the observed sulfate profile must have happened very recently (i.e., several tens of years). Holstein and Wirtz (2010) observed similar sulfate profiles on a tidal sand flat sediment along the northern Germany coast. They explained this observation as resulting from a rapid organoclastic sulfate reduction fueled by a downward transport of labile organic matter during flat progression. In both cases, the authors agreed upon the transient nature of the observed S-shape profiles, and propose episodic sediment pulses as their causal mechanisms. The fast sedimentation in the shallow part of sediment column rapidly buries sulfate before it diffuses out or it is

entirely consumed. Such sulfate burial results in a section with almost constant sulfate concentration. If this is the only process altering sulfate profile, then "kink type" profiles of sulfate (Zabel and Schulz, 2001; Hensen et al., 2003) may be expected. Consumption of sulfate through POCSR in the section with rapid sedimentation is required for the s-shape profiles, as were observed in the K-G Basin, Argentine Basin, northern Germany coast, and potentially elsewhere along continental margins worldwide.

The MTDs inferred from our analyses of pore water data from the K-G basin are much larger in scale and significantly older than those discussed previously, which span only 2-8 meters in thickness and are thought to reflect events that occurred several tens of years before sampling (Hensen et al., 2003 and Holstein and Wirtz, 2010). By simulating the profiles until they reach a new steady state (Figure 4-2D), we estimated the maximum amount of time (Δt_2) that these anomalous sulfate profiles can survive to range from 2000 to 3800 years (Table 4-3). Mazumdar et al. (2009) observed the similar s-shape sulfate profile from a site close to the Site 10D in our study. The rapid sedimentation for the first 6 meters of their sediment core suggests influence from MTDs which were dated as ~5 kyr old. Collectively, our results and the dating from Mazumdar et al. (2009) suggest that such S-shape sulfate profiles may survive longer than previously assumed, if MTDs are large enough in scale. The fact that we observed the influence of MTDs from the seven sites over 90 km in the basin is consistent with the observations of the widespread occurrence of MTDs in the K-G Basin. However, our modeling approach identified the influence of MTDs at some sites that were not recognized by geophysical or core observations, and points to the value of this technique in identifying MTDs and quantifying their magnitude and age.

4.7 Conclusions

By simulating the pore water sulfate and ammonium concentrations measured at seven sites drilled in the K-G Basin during the NGHP-01 expedition, we provide a quantitative description of how the MTDs can affect the geochemistry profiles. Our model provides reliable estimates of the MTDs thickness (Δx=8-25 meters), the time elapsed after the

most recent event (Δt_1=450 to 1600 years), and the organoclastic sulfate reduction rate (R_{POCSR}=126 to 1215 mmol $SO_4^{-2}/m^2/yr$) at these seven sites. We also estimated the time required for the system to reach a new steady state after the MTD events (Δt_2=2000 to 3800 years).

If we exclude site 15A, we observe a positive correlation between water depth and the average depositional rate ($\Delta x/\Delta t_1$), in agreement with the previous observations of mass transport processes in this basin. The depth-integrated sulfate reduction rates estimated here are higher than published values from other sites. This is because the rates in the K-G basin were estimated by integrating over sediment depths that correspond to the thickness of the MTDs, and are two to five times thicker than the sulfate reduction zone in other studies. Site 15A is anomalous in its sulfate and porosity data which suggest that sediment deposition at this site may be more dynamic than the other study sites.

We caution against using the pore water profiles of sites experiencing significant MTDs to infer metabolic processes before considering the role that sediment transport can have on the pore water distributions. In particular, we question the postulated sulfate-reducing ammonium oxidation pathway by Schrum et al. (2009), based on the low ammonium concentration observed within the first sulfate reduction zone at Site 14A. The results from our model show that the data at Site 14A reflects a non-steady state condition triggered by a MTD in this basin.

4.8 Acknowledgement

The authors would like to thank co-chief scientists, captain, crew members and science party during the NGHP-01 expedition for their assistance with sample collection and onboard analyses. Funding support from Department of Energy (DE-FOA-0000668, DE-FE-0010496) for this work is also greatly appreciated.

Figure 4-1 map of the study area

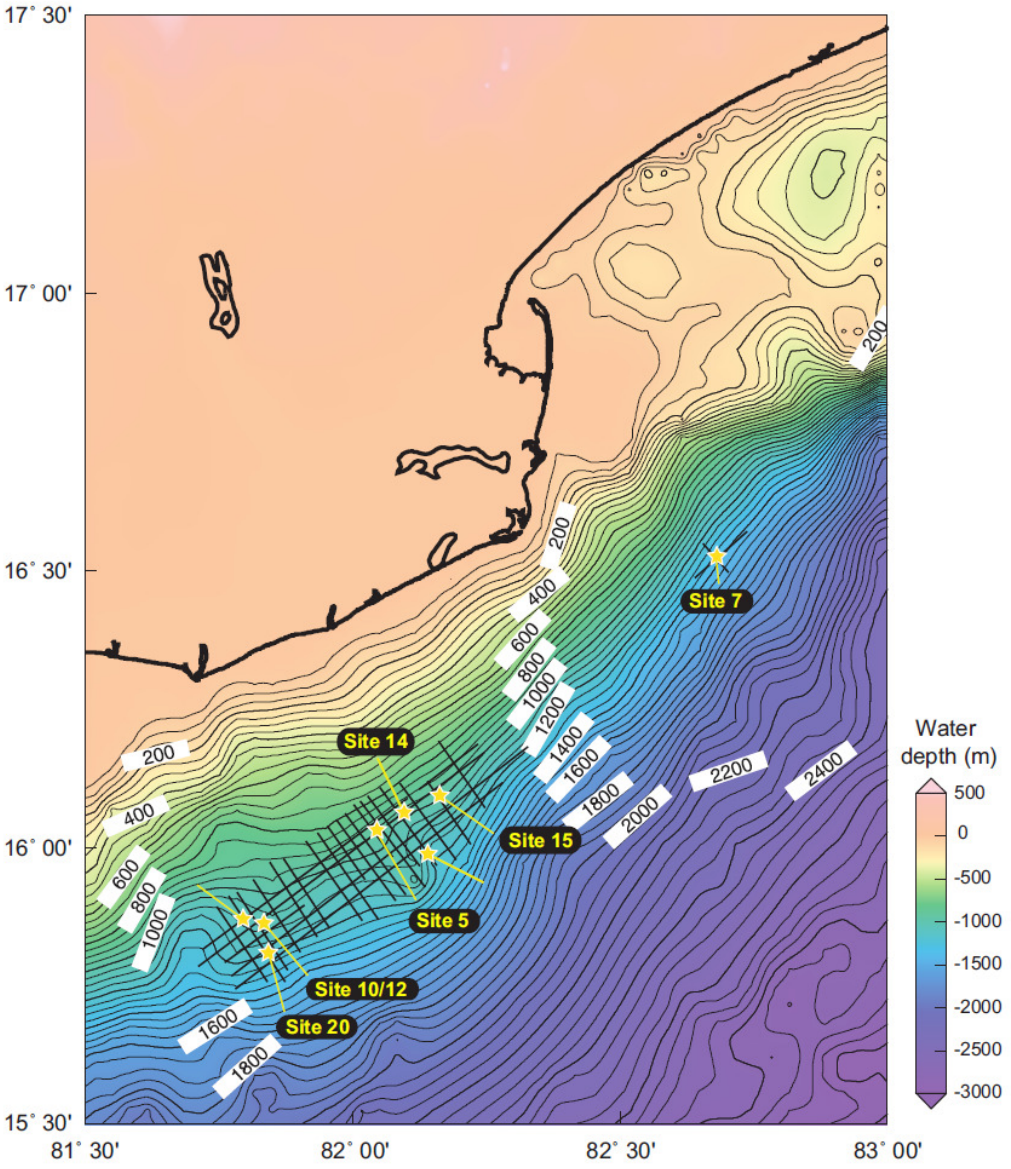

Figure 4-2 Schematic diagram showing the steps involved in the transport-reaction model to simulate the effect of MTDs on pore water sulfate profiles. (A) The pre-MTD pore water profiles (step 1) were set by simulating a L-meter long sediment column to steady state using sea water composition as the initial condition. Methane flux assigned here is constrained by the both sulfate and methane profiles (i.e., the assigned methane flux has to be at least higher than the observed flux). (B) The MTD (the grey rectangle) with fresh labile organic matter is deposited instantaneously onto the sediment column and buries the SMTZ to a greater depth. (C) In step 2, the pore water profiles and methane flux resulting from step 1 are used as the initial condition. Due to the addition of reactive labile organic matter in the MTD, sulfate is consumed at shallow depth through POCSR only (the first sulfate reduction zone) whereas methane exhausts sulfate from below by AOM and POCSR (the second sulfate reduction zone). The SMTZ in (B) and (C) illustrate this non-steady-state condition, which is observed at seven KG basin sites. The Δx (thickness of MTD) and Δt_1 (time required to reach present observed profile) are estimated by fitting data at each site and are reported in Table 4-3. (D) The system is expected to reach another new steady state condition after Δt_2 years (Table 4-3).

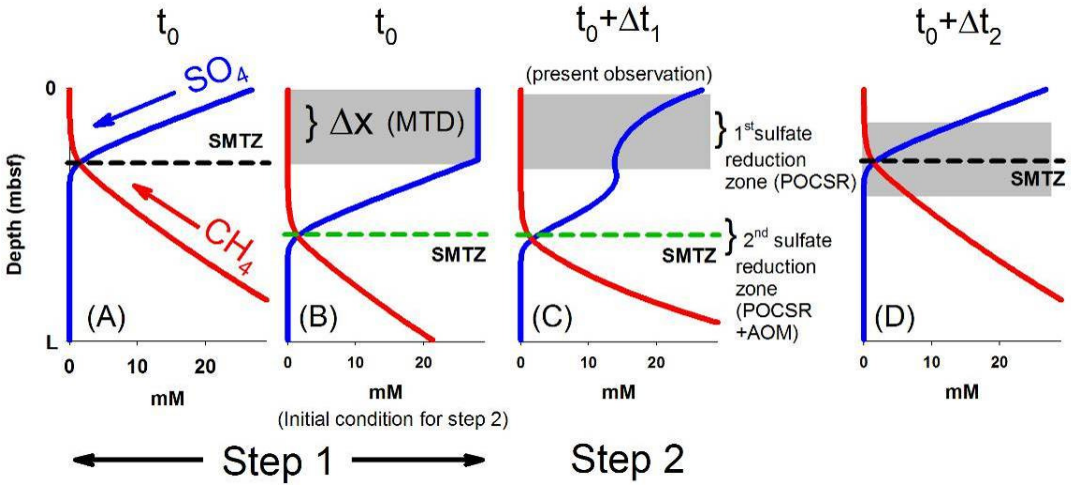

Figure 4-3 Simulation conducted at Site 5C to test the sensitivity of the model to the Δx, Δt and k_{OM} parameters. Blue lines in each panel indicate the best fit to the data, and red lines show changes that would result from small variations in the values assigned to these parameters As the results indicate, the three parameters can be well constrained by fitting the observed sulfate and ammonium profiles.

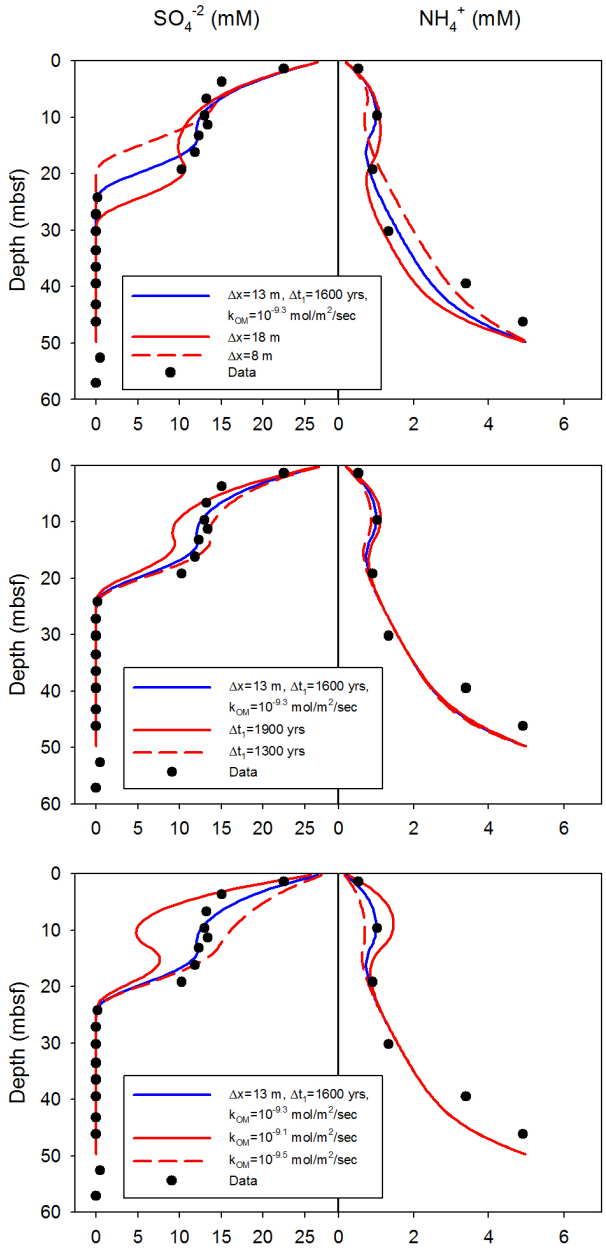

Figure 4-4 Model results and the observed sulfate (blue lines and circles), methane (red lines and squares), and ammonium (pink lines and diamonds) profiles at the seven study sites. The depths where thin silt laminae and beds (grey lines) were observed at each site were also plotted for comparison although no apparent correlation was observed between the frequency of laminae and the thickness of MTDs (Δx, Green lines).

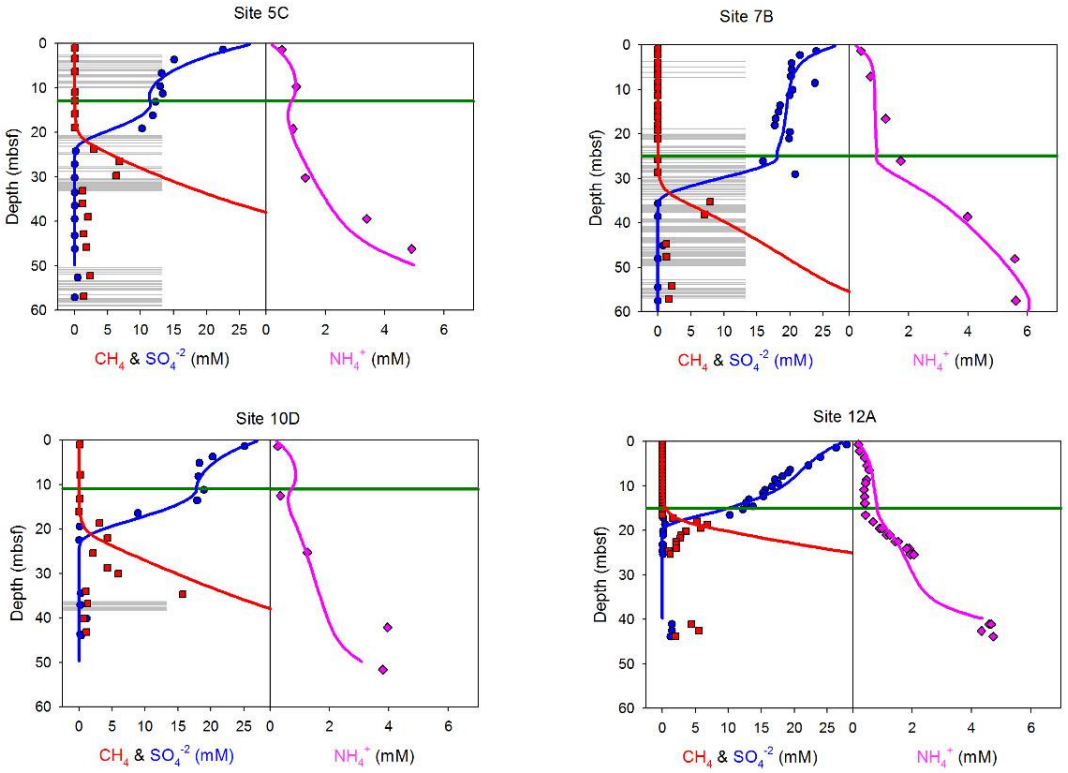

Figure 4-4 (Continued)

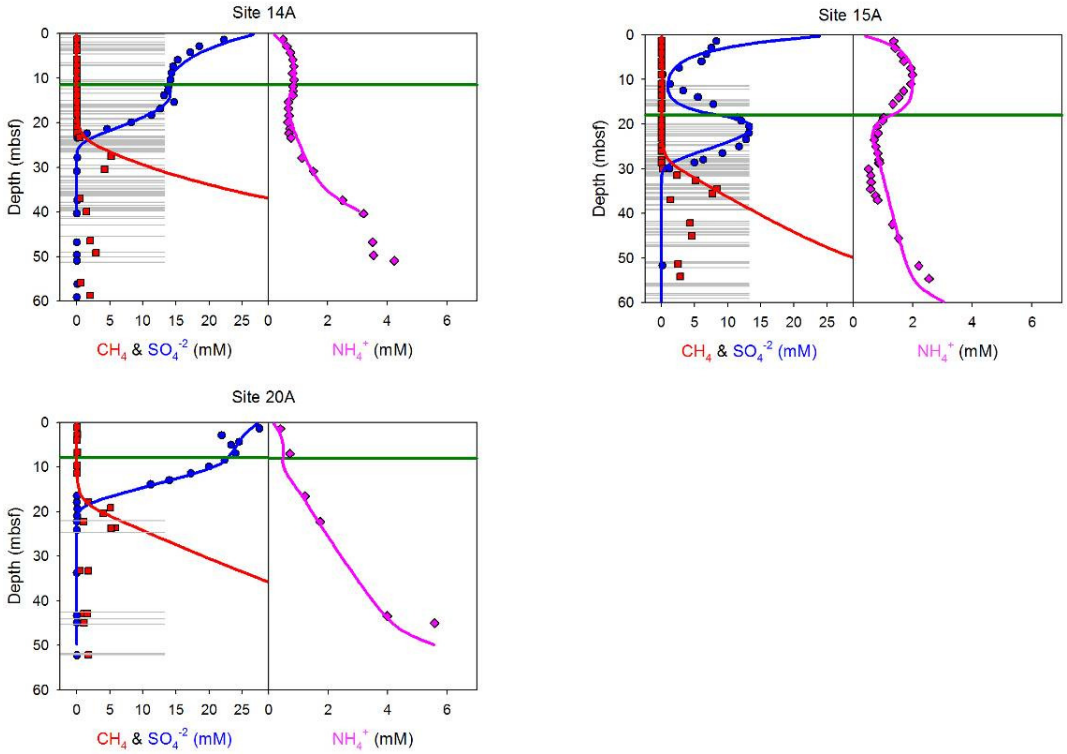

Figure 4-5 Correlation between water depth and the average depositional rate ($\Delta x/\Delta t$). The positive correlation, if Site 15A is excluded, suggests that sites at greater water depth receive more sediments than those located in shallower water which agrees with previous observation in this region (Ramprasad et al., 2011). In order to fit the sulfate profile in Site 15A, a higher k_{OM} is required which may suggest more dynamic conditions at this site as described in the text.

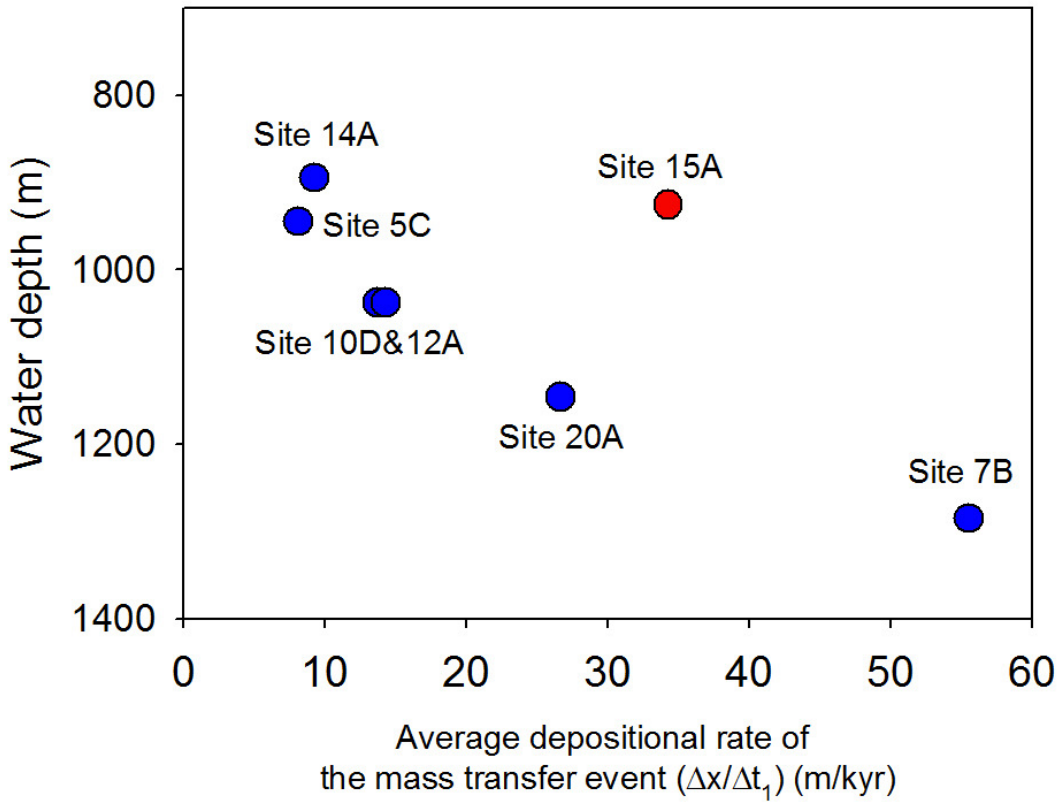

Figure 4-6 Conceptual model to exaplain the sulfate profile at Site 15A. (A) Comparison of porosity profiles between Site 14A and 15A, the two adjacent sites. The first measurement at Site 15A is ~5% lower than that at Site 14A suggesting that the MTD section in Site 15A may have undergone recent erosion. The two red lines mark our estimated thickness of MTD at Site 15A. In contrast to the initial homogenous sulfate content in the MTD sections at all other sites (Figure 2B), the intial sulfate profile in the MTD section at Site 15B may already be low in sulfate and the total depletion of sulfate within the MTD suggests that this sediment column had experienced POCSR for a period of time before the emplacement at Site 15A. Such that immediately after emplacement, the system had a sulfate distribution as shwon in (B) The continuous consumption of sulfate by POCSR in the MTD section after depositing result in the present observed sulfate profile at Site 15A, as shown in (C)

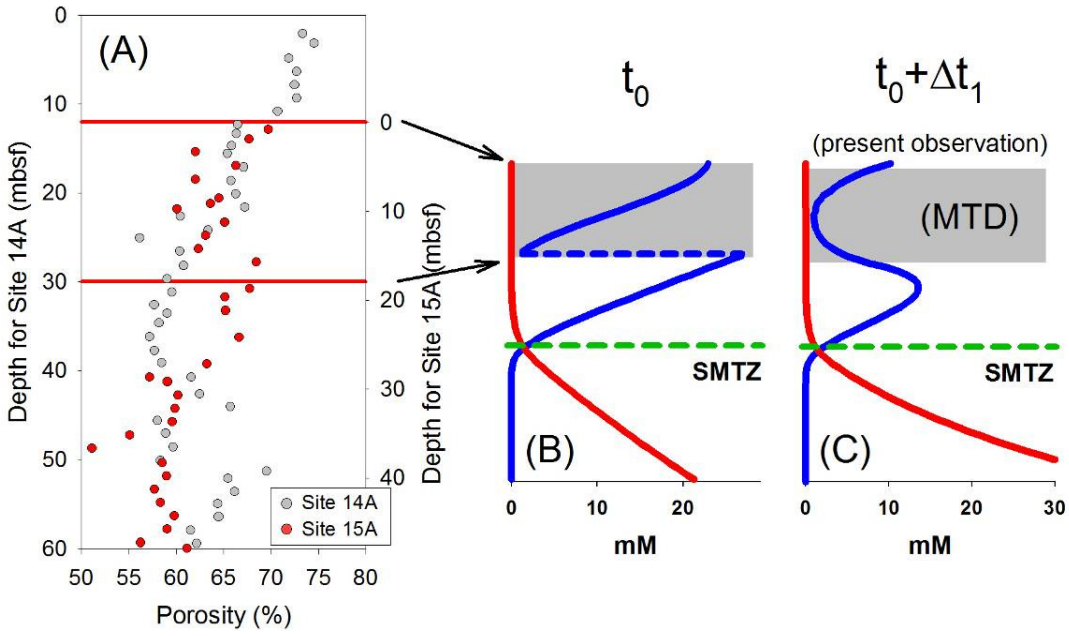

Table 4-1 Water depth and the location of the seven study sites.

	Water Depth (m)	latitude	longitude
Site 5C	945	16° 01.722N	82° 02.677E
Site 7B	1285	16° 31.2785N	82° 40.8672E
Site 10D	1038	15° 51.8609N	81° 59.0749E
Site 12A	1038	15° 51.8609N	81° 59.0749E
Site 14A	895	16° 03.5577N	82° 05.6218E
Site 15A	926	16° 05.6983N	82° 09.7467E
Site 20A	1146	15° 48.5671N	81° 50.5760E

Table 4-2 Input parameters for model simulations.

	L (m)	Sea floor Temperature (^oC)	Geothermal gradient (^oC/m)	m	ϕ_0[b] (%)	ϕ_f[b] (%)	γ[b]	C/N	CEC[c] (meq per 100 g sed.)
Site 5C	50	7.1	0.044	2.75	77.5	57.5	-0.04	13	80
Site 7B	60	5.3	0.052	2.75	77.5	52.5	-0.04	8.5	80
Site 10D	40	6.5	0.045	3.5	77.5	63	-0.1	8.5	80
Site 12A	40	6.5[a]	0.045[a]	3.5[a]	80	60	-0.07	12	80
Site 14A	40	7.9	0.038	2.5	77	50	-0.03	13	80
Site 15A	60	7.7	0.04	2.5	70	57.5	-0.05	14	50
Site 20A	50	5.5	0.049	2.25	80	55	-0.12	10	70

[a] Assuming the same as Site 10.

[b] These parameters were estimated from the first 40 to 60 meter of the core sediments

[c] cation exchange capacity

Table 4-3 Model-derived results (Δx: thickness of MTD; $\Delta t1$: time elapsed after the MTD event; $\Delta t2$: times requires to reach a new steady state; k_{OM}: kinetic constant for POCSR; R_{SR}: depth-integrated sulfate reduction rate)

	Δx (m)	Δt_1 (yr)	Δt_2 (yr)	k_{OM} (10^x moles/m^2/sec)	$\Delta x/\Delta t_1$ (m/kyr)	R_{POCSR} in Δx (mmol SO_4^{-2}/m^2/yr)
Site 5C	13	1600	3350	-9.3	8.1	200
Site 7B	25	450	2200	-9.1	55.6	620
Site 10D	11	800	3800	-9.3	13.8	170
Site 12A	15	1050	2100	-9.5	14.3	150
Site 14A	13	1400	3800	-9.3	9.3	20
Site 15A	18	525	2000	-8.65	34.29	1220
Site 20A	8	300	3800	-9.3	26.67	130

CHAPTER 5

Diagenetic formation and dissolution of silica in sediments approaching the Nankai margin subduction zone

Wei-Li Hong, Marta E Torres, and Glenn A Spinelli

Geochemistry, Geophysics, Geosystems
in review

5.1 Abstract

We develop a transport-reaction model to investigate the critical reactions that control the silica diagenesis in the incoming sediments to the Nankai Trough. We present a silica reaction network and validate our results with existing pore water and sediment geochemical data at four sites of different sedimentary and thermal conditions, drilled during ODP and IODP expeditions. Our model reproduces a silica diagenetic boundary (SDB) at each site, which is defined by marked decreases in reactive volcanic ash, pore water silica and potassium. Volcanic ash alteration, was constrained by modeling pore water $^{87}Sr/^{86}Sr$ profiles, and the derived reaction rate of $10^{-12.13}$ to $10^{-11.75}$ mol of $Si/m^2/sec$ provides the $SiO_{2(aq)}$ at rates required to form authigenic amorphous silica phase above the SDB. Below the SDB, formation of clinoptilolite consumes potassium and regulates the extension of amorphous silica by consuming $SiO_{2(aq)}$. The observed low $SiO_{2(aq)}$ and dissolved potassium in these deep sequences require continuous precipitation of clinoptilolite; however in order to maintain oversaturation of this mineral at the low $SiO_{2(aq)}$ in sediments below the SDB, an increase in pH is required, consistent with pore water observations. Thermal history, rather than temperature alone, controls the inferred reaction network as shown by the convergence of the thermal maturity of sediments at the SDB from all sites (ΣTTI ranges from 0.0053-0.0124), consistent with other locations documented onshore Japan. Our study results are valuable as we move forward in understanding the mechanisms and consequences of ash alteration in convergent margins worldwide.

5.2 Introduction

A series of diagenetic processes involving silica phases modify the composition of sediment pore water (Kastner, 1981) and have been shown to induce local precipitation of silica and calcium carbonate cements, which in turn can alter sediment elastic properties (e.g., sonic velocity) (Eberli et al., 2003; Spinelli et al., 2007; Saberi et al., 2009). Additionally, cementation may influence the mechanical and hydrogeologic behavior of the sediment in ways that may affect the distribution of seismicity (Kameda et al., 2012), development of fault systems (Cartwright, 2011), and stability of sediments prior to or during subduction (Spinelli et al., 2007; White et al., 2011).

Due to the proximity of volcanic sources, sediments accumulating near active continental margins commonly contain volcanic ash. The ash may be disseminated throughout the sediment and/or be present in discrete layers (e.g., Peters et al., 2000; Scudder et al., 2009). The reactions involving volcanic ash drive many silica diagenetic processes in hemipelagic sediment sections (Kastner, 1981; Wallmann et al., 2008; Schulz and Zabel 2006). There is an increasing awareness of the fundamental role that the silica, calcium and bicarbonate ions released during volcanic ash weathering plays in facilitating authigenic mineral precipitation (Huggett, 1993; Jeans et al., 2000; Mork et al., 2001). Ash alteration can increase the dissolved Si concentration in pore fluids, leading to the formation of amorphous silica cements and may drive subsequent formation of clays and zeolites (Kastner, 1981). The increase in calcium and bicarbonate that result from ash alteration reactions can induce carbonate precipitation, and may play a role in global CO_2 budgets (Wallmann et al., 2008).

The processes summarized above have been predicted to occur along the Nankai margin based on pore water profiles; however the reaction network involved has not been defined. Offshore of the Nankai margin, Deep Sea Drilling Project (DSDP) Site 297 and Ocean Drilling Program (ODP) Site 1173 and 1177 recovered small amounts of glass disseminated throughout hemipelagic sediment which was converted to an amorphous silica phase upon burial (Spinelli et al., 2007). The resulting amorphous silica can form

grain-coating cements, and may be responsible for changes in porosity, seismic velocity, and shear rigidity of sediments across the upper and lower Shikoku Basin facies (Moore et al., 2001; Spinelli et al., 2007). Sample et al. (2013) have shown that while carbonate cements begin to form very early in the burial history, calcite also forms deep within the Shikoku Basin sediments, and postulate that these reactions are driven by alteration of volcaniclastic material within the sediment and ocean crust. Ash-derived authigenic carbonates can be significant in the global carbon isotopic mass balance, and in global CO_2 budgets (Schrag et al., 2013; Wallmann et al., 2008), as well as impact the mechanical properties of the sediment prior to subduction.

We take advantage of pore water strontium isotope data to estimate the ash alteration rates and use these results to develop a transport-reaction model to simulate the reactions that control the location and extent of the amorphous silica zone in the Shikoku Basin. Our multicomponent reactive transport simulation includes key pore water species and mineral phases, for sediments typical of Shikoku Basin and elsewhere. We evaluate our simulations against pore water data from four sites drilled in the incoming sediments to the Nankai subduction zone, which are characterized by a range of sediment accumulation rates and thermal histories. Because ash alteration is prevalent in active margins, our results not only provide insights on the Nankai margin system but may be extended to understand the systematic and progressive changes in sediment composition and physical properties prior to subduction in convergent margins worldwide.

5.3 Background and Hypothesis

Nankai Trough is a convergent plate boundary that formed during the northwest subduction of Philippine Sea plate beneath the Euroasian plate. This seismically active area has been intensively sampled by ODP and IODP expeditions (Figure 5-1). The incoming sediments of the Shikoku Basin have been cored along three transects perpendicular to Nankai Trough to characterize the sediment inputs prior to subduction (Underwood et al., 2010). Sediment within the Shikoku Basin varies in thickness and deposition rate, and the facies architecture is controlled largely by variations in basement

topography (Underwood, 2007; Ike et al., 2008). In the simplest view, the strata can be grouped into two units, upper and lower Shikoku Basin facies, which are overlain by Quaternary turbidites of the Nankai trench wedge.

There is a long history of ash accumulation, burial, and alteration within the sediments of the Shikoku Basin. The relative ash content of the sediment sequences in the incoming plate likely reflect the regional and time-dependent volcanic activity of the surrounding arcs (e.g., Kennett et al., 1977; Ledbetter and Sparks, 1979; Cambray et al., 1995); therefore, ash content may be used to define lithologic boundaries. In some cases, lithologic and diagenetic boundaries within the Shikoku Basin sediments coincide. As originally defined, one of the key distinctions between the upper and lower Shikoku Basin facies is the presence or absence of unaltered volcanic glass (Shipboard Scientific Party, 1991). However, facies boundaries in the Shikoku Basin are time-transgressive, and some units/subunits do not extend across the entire basin (e.g., Moore et al., 2001; Underwood et al., 2010). Thus, we focus on the factors controlling silica diagenesis, regardless of whether or not the resulting diagenetic boundaries coincide with broader lithologic boundaries. Evidence from Sr isotopic data (Joseph et al., 2013), detailed X-ray diffraction analyses (Masuda et al., 1996), backscatter electron and scanning electron microscope images (White et al., 2011) and thin section observations (Expedition 333 Scientists, 2012b, 2012c) all document intensive alteration of disseminated ash within the Shikoku Basin sediments. We refer to the zone that separates unaltered from significantly altered ash as the silica diagenetic boundary (SDB). At Sites 1173 and 1177, the SDB coincides with the lithologically-defined boundary between upper and lower Shikoku Basin facies (Shipboard Scientific Party, 2001). At Sites C0011 and C0012 the SDB occurs within the upper Shikoku Basin facies (Underwood et al., 2010; Expedition 333 Scientists, 2012a). By defining the boundary in terms of diagenetic changes, we believe our observations may be generally applicable to subduction zones where ash alteration reactions control sediment geochemical properties.

We examine key pore water species in the incoming Shikuko Basin in the context of the reaction sequence proposed by Masuda et al. (1993, 1996), whose observations provide an important foundation for the aluminosilicate mineral diagenesis in Nankai Trough area. From studies of mineral assemblages and the composition of aluminosilicate minerals (Masuda et al., 1993; 1996) at ODP Site 808, these authors concluded that ash alteration, smectite, clinoptilolite, illite, and analcite formation control the abundance of $SiO_{2(aq)}$ and K, in the pore water (Figure 5- 2).

Among all reactions, ash alteration is the engine driving the reaction network as reflected by the pore water Sr isotopic profiles (Figure 5- 3). Ash alteration releases enough $SiO_{2(aq)}$ to sustain formation of amorphous silica above the SDB, which have been documented by SEM analyses (White et al., 2011). The excess $SiO_{2(aq)}$ released should also trigger the precipitation of aluminosilicate minerals that sequester pore water K, as observed by Masuda et al. (1993). The precipitation of aluminosilicate minerals regulates the growth of the amorphous silica and eventually leads to its dissolution. To quantify these processes and elucidate their roles in controlling the pore water profiles across the SDB, we examined the most likely aluminosilicate sinks (clinoptilolite, smectite, and illite) and implemented a kinetic model that tracks the progressive diagenetic changes of various silica phases and the key controlling parameters such as sedimentation rates and geothermal gradients. We then verified the model outputs against sediment and pore water geochemical measurements available from four drilled sites in the incoming plate sediments.

5.4 Methods

5.4.1 Modeling Scheme

For our simulations we adapted CrunchFlow (Steefel and Maher, 2009), a numerical code that uses a global implicit scheme (Steefel and Yabusaki, 1996) to solve reaction-transport equations. This code allows us to simulate the chemical profiles by incorporating transport parameters of solid phases and dissolved species, as well as the

thermodynamics and kinetics of the sediment-water interactions (e.g., mineral precipitation/dissolution).

CrunchFlow was previously used to estimate fluid seepage rates and reactions in the hemipelagic sediment on the flank of Juan de Fuca Ridge (Giambalvo et al., 2002). We modified their approach to describe the sedimentary context of a heterogeneous domain (i.e., sediment plus basement). The model simulates changes in a sediment column that overlies a basement aquifer with a distinct pore fluid chemical composition that is independent of the chemistry of the sedimentary system but is in diffusive communication with the bottom sediment. In our approach, the sediment column is allowed to grow with time so that the contact between sediment and basement is progressively buried; this burial occurs by discrete sediment inputs in a stepwise fashion. In the first time-step, a five-meter thick sediment package is allowed to evolve chemically for a time period equivalent to that needed for the sediment to accumulate (i.e., 5 m divided by the sedimentation rate). Distinct initial chemical conditions are defined to represent the composition over (i.e., bottom seawater composition), and under (i.e., composition in the uppermost basement aquifer) the 5-m sediment column. Because of the challenges associated with measuring pore fluid composition of a permeable basement, there is no data available for the composition of fluids in the upper igneous Phillippine Sea crust. Therefore, we used the deepest pore water measurements to represent the composition of the fluid in the underlying oceanic lithosphere (Table 1). In time-step two, an additional five-meter thick sediment package is added to the top, and the entire sediment column is allowed to evolve chemically for the period of time it took to accumulate that second package. We use the output from time-step one to set up the initial conditions for the following time-step two. Sequential sediment packages are added using this stepwise approach, until the full sediment column is accumulated. See Figure S1 in supporting information for the graphical presentation of this stepwise approach.

The chemical and properties of the basement fluid as well as the physical properties of basement are assumed to remain constant throughout the entire simulation. We acknowledge the simplification inherent in this assumption, but, since there are no direct data on the present or past fluid composition of this aquifer, more elaborated assumptions are not warranted without further constraints on the evolution of basement fluid composition. However, to test the effect of our constant boundary condition assumption, we ran two simulations to determine the sensitivity of the pore water Sr isotopic profiles to the lower boundary condition chosen, as our Sr isotopic profiles reflect mixing among fluids from bottom seawater, volcanic ash, and volcanic basement. In one simulation, the lower boundary condition was set to evolve from the composition of ocean bottom water to the volcanic basement fluid as the sediment column grows (Table S1). In a second simulation, the lower boundary condition is fixed to basement fluid composition throughout the simulation (Table S1). Because chemical diffusion is fast relative to sedimentation throughout most of the history of these sites, the composition of sediment pore water rapidly responds to an evolving lower boundary condition. The Sr isotopic profiles at the end of simulation for both cases are almost identical (Figure S2) as well as the ash alteration rates. The ash alteration rate result from a evolving lower boundary condition is only 3.6% higher than the rate determined with a fixed basement fluid composition. Based on this sensitivity analyses, we are satisfied that a constant composition for the basement aquifer is a proper assumption.

5.4.2 Temperature and porosity

Temperature and porosity gradients at the four sites were estimated from shipboard measurements (Shipboard Scientific Party, 2001; Expedition 333 Scientists, 2012a). The bottom water temperature and geothermal gradients are listed in Table 1. The porosity profile is described by an exponential function:

$$\phi(z) = Ae^{\gamma z} \quad (5.1)$$

where ϕ is porosity, z is depth (m) below seafloor, and A and γ are parameters used to fit the porosity profiles to the available data (Table 1).

5.4.3 Chemical transport parameters

Diffusion coefficients of all primary species at 25°C are from Li and Gregory (1974) and Boudreau (1997) and were adjusted for temperature and for tortuosity by specifying a "cementation-exponent" parameter that calculates the porosity-dependent tortuosity. This parameter is derived from the borehole logging measurements and the correlation between formation factor and porosity (Tudge et al., 2013). Burial rates for the solids were estimated from the reduction of porosity assuming steady state compaction (Berner, 1980). We used a constant value for fluid burial rate, assumed to be 75% of the solid burial rate at the sediment/basement interface.

5.4.4 Chemical species

We included 12 primary dissolved species (Table 1) and no secondary or gas species. The initial and boundary conditions for each of the dissolved species as well as the kinetic constants used for each of the solid phases are listed in Table 1. We used the thermodynamic parameters for each reaction given in the CrunchFlow database, adjusted with SUPCRT (Johnson et al., 1992) to account for pressure effects. The kinetic constant for ash decomposition is constrained by dissolved Sr isotopic profiles, as detailed in the following paragraphs. The kinetic constants for other minerals are either from the default CrunchFlow database or constrained from data-fitting, as indicated in Table 1.

5.5 Results and discussion

5.5.1 Silica release above the SDB: Amorphous silicate precipitation and ash decomposition rate

White et al. (2011) showed a genetic relationship between volcanic ash and silicate cement in sediments from DSDP Site 297, where the amorphous silica profile is similar

to that observed at our four sites. We therefore include both amorphous silica and volcanic ash in the model to quantify their interaction. Precipitation/dissolution of amorphous silicate is described by:

$$SiO_{2(am)} \rightarrow SiO_{2(aq)} \qquad (5.2)$$

This is a well-defined reaction in CrunchFlow with all the required thermodynamic properties in its database.

Ash alteration is implemented by using the following stoichiometry:

$$\text{Ash} + 0.9686\ H^{+} + 0.91146\ H_2O \rightarrow 1\ SiO_{2(aq)} + 0.2681\ Al^{+3} + 0.0722\ Ca^{+2} + 0.0188\ Mg^{+2} + 0.1023\ Na^{+} + 0.12\ HCO_3^{-} \qquad (5.3)$$

This stoichiometry comes from chemical analysis of volcanic glass shards disseminated in the hemipelagic sediments in the Shikoku Basin (White et al., 2011). We derived the ash stoichiometry by dividing the weight percentages of oxides (SiO_2, Al_2O_3, Fe_2O_3, CaO, MgO, Na_2O, and H_2O) measured in glass shards (White et al., 2011) by their molecular weights. Bicarbonate is a product of reactive silicate weathering (Wallmann et al., 2008), but it is not possible to constrain the carbon content of the Shikoku Basin glass shards with the analytical techniques used by White et al. (2011). Following the general consideration of reactive silicate weathering (e.g., Wallmann et al., 2008), we allow bicarbonate to be released during ash dissolution; its stoichiometry was arbitrarily set to best fit the pore water profiles. Consumption of CO_2 during ash dissolution is ignored in our expression to avoid further complication, although we do acknowledge the significance of this reaction to overall carbon cycling (e.g., Scholz et al., 2013).

We estimated the rate of ash decomposition using pore water Sr isotopic profiles available for Sites C0011 and C0012 (Figure 5- 3, data from Joseph et al., 2013). The Sr systematics in the upper sediments at these sites reveal a two end-member system

characterized by mixing of seawater with a fluid that has interacted with an ^{87}Sr depleted volcanic ash layer ($^{87}Sr/^{86}Sr$ ratio for ash ~0.7063; Joseph et al., 2013), consistent with major ion distributions (Underwood et al., 2010; Expedition 333 Scientists, 2012a). At both sites the foci of ash alteration inferred from the dissolved Sr isotopic profiles match the observations made by ship-based sedimentologists based on smear-slide analyses (Figure 5- 3; Expedition 333 Scientists, 2012c).

Drilling at Site C0011 terminated before reaching basement due to technical difficulties (Underwood et al., 2010), so at this site there is no data to estimate the effect of basement aquifer on sediment pore fluid (Torres et al., in review). In the sediments below 450 mbsf at Site C0012, pore-water $^{87}Sr/^{86}Sr$ data show a decrease to a more depleted value of 0.70436, indicating fluid interaction with a basaltic end-member ($^{87}Sr/^{86}Sr \sim 0.703$ to 0.705; Staudigel et al., 1981) (Figure 5- 3). Boundary conditions were set based on total Sr concentration in pore fluid data from the shallowest and deepest sediments recovered. ^{86}Sr was assumed to be 9.86% of the total Sr content (mole fraction) in the fluid (De Laeter et al., 2003), and the ^{87}Sr was calculated from the estimated ^{86}Sr and the measured Sr isotopic ratios. The ash alteration rates obtained from Sr isotopic profiles for Sites C0011 and C0012 were further constrained by comparison with the amorphous Si. For Site 1173 and 1177, where pore water Sr isotopic data were not available, ash alteration rates were solely constrained by their volcanic ash content.

The reactiveness of ash is controlled by its surface area. For the surface boundary condition we chose a value of 0.2 m^2 per m^3 of porous media, based on Giambalvo et al. (2002), and 0 m^2 per m^3 of porous media at the basement boundary. The Sr to SiO_2 ratio in ash was determined from the pore water profiles between 200 to 450 mbsf where the Sr isotopic profile indicates ash dissolution to be most significant. The ratio 0.0075 was chosen to roughly match the observed $SiO_{2(aq)}$ and Sr profiles. The thermodynamic and kinetic properties of the ash were defined to satisfy the depths of maximum ash dissolution and strontium isotope data. Because the sediments at Site C0012 have

undergone significant recent erosion, we modeled the profile only until the onset of erosion, which started ~1 Myr before present (Expedition 333 Scientists, 2012a).

The good agreement between the model results and observations gives credence to this approach (Figure 5- 3). We also conducted sensitivity tests using ash alteration rates arbitrarily set to be higher and lower than the model-predicted rates by a factor of two (Figure S3). Results of such test show that both Sr isotopes and volcanic ash profiles are very sensitive to the chosen ash alteration rate and therefore these data provide good constraints on reaction rates. The kinetic rate constant for ash decomposition at 25 ^{o}C derived from this approach ranges from $10^{-12.13}$ to $10^{-11.75}$ mol of Si/m^2/sec (Table 2). Our estimates are at the low end of a wide range of previously published rates. For example, estimates for the dissolution rate of ash in the Mt. Fuji area at ~12 ^{o}C and neutral pH range from $10^{-9.0}$ to $10^{-8.8}$ mol of Si/m^2/sec (Shikazono et al., 2005). Valle et al. (2010) reports an experimentally determined dissolution rate of $10^{-7.3}$ mol of Si/m^2/sec, at 90 ^{o}C and pH=8.3-7.8, whereas the estimated of Declercq et al. (2013) range from $10^{-9.28}$ to $10^{-9.73}$ mol of Si/m^2/sec, using 80 ^{o}C and a more basic environment (pH=8.8-10.1). Yokoyama and Banfield (2002) performed experiments at 20 ^{o}C and pH=6-7 using rhyolite samples collected from Kozushima (offshore Japan), and estimated the dissolution rate to range $10^{-12.3}$ to $10^{-14.2}$ mol of Si/m^2/sec. The wide range of values reflects the complex nature of ash decomposition. Nonetheless the approach proposed here highlights the importance of quantifying ash alteration at the particular sites of interest, and documents the feasibility of using geochemical data to arrive at good in situ rates.

5.5.2 Dissolved silica uptake below SDB: Role of aluminosilicate minerals

Pore water profiles indicate the need for reactions that consume $SiO_{2(aq)}$ below the SDB (Figure 5- 2). Under the mineral assemblage observed by Masuda et al. (1993), we examine the solubility of several key aluminosilicate minerals to determine the most likely mineral(s) that serve as the sink of pore water potassium and $SiO_{2(aq)}$ and regulate the growth of amorphous silica. In Figure 5- 4 we show the solubility (K_{eq}) of the 3 target

aluminosilicate minerals (illite, smectite, and clinoptilolite) and the pore water activity products (Q) as a function of temperature. The stoichiometry of these minerals was taken from the default CrunchFlow database, and the solute activity was calculated by CrunchFlow, using extended Debye-Huckel model for activity coefficients (Steefel, 2009).

The Q of these minerals is controlled by the activities of pore water constituents including $SiO_{2(aq)}$, Na^{+}, Ca^{+2}, Mg^{+2}, K^{+}, Al^{+3} or Fe^{+2} and H^{+}. Whereas we have access to major ions, the trace metals (Fe^{+2} and Al^{+3}) are not commonly measured in pore fluids. The concentration of Al^{+3} was set to 0.1 μM (Brumsack and Gieskes, 1983; Mackin and Aller, 1984); for Fe^{+2} we chose a concentration of 1 μM, based on measurements at Site C0011 and C0012. The fixed activities assigned ensure that the changes in Q reflect the fluctuation of other pore water constituents that are well-constrained by pore water data. Our solubility analysis shows that all minerals except clinoptilolite are highly oversaturated at all depths with respect to the current pore water composition, even when both pore water $SiO_{2(aq)}$ and potassium content are low. Such exceedingly high oversaturation values for smectite and illite will suppress the formation of amorphous silica which is in contradiction to the observations by White et al. (2011). We therefore excluded these two minerals from our reaction network. This conclusion is valid even when we vary the Al^{+3} and Fe^{+2} activities by two orders of magnitude.

Based on the observation of a SDB that coincides with a decrease in dissolved Si and K at Site 808 (Figure 5- 2), and guided by our mineral saturation analyses, we selected the dehydrated K-bearing clinoptilolite (clinoptilolite-dehy-K) as the authigenic mineral controlling the $SiO_{2(aq)}$ and K distributions, using stoichiometry from the CrunchFlow database such that:

$$\text{Clinoptilolite} + 13.868\ H^{+} \rightarrow 0.017\ Fe^{+3} + 3.45\ Al^{+3} + 3.467\ K^{+} + 6.934\ H_2O + 16.633\ SiO_{2(aq)} \quad (5.4)$$

We noted that the high dependency on potassium activities matches the observation that these solutes are depleted at the depths where smear slide observations indicate that significant ash alteration has occurred (Figure 5- 3). Furthermore, the presence of zeolite minerals, including clinoptilolite and analcime, was confirmed through XRD observations in the lower Shikoku Basin at Site C0011 (Expedition 322 Scientists, 2010) and Site 808 (Masuda et al., 1993). The presence of clinoptilolite coincides with the marked decrease in silica and potassium content of the pore fluids at that site (Figure 5- 2).

5.5.3 Carbonate and pH control

Alteration of ash releases enough Ca and consumes enough protons to drive carbonate formation, as evidenced by calcite equilibrium models (Wallmann et al., 2008; Sample et al., in review). Carbonate is commonly observed in the input sediment sections to the Nankai Trough (Underwood et al., 2010; Expedition 333 Scientists, 2012a; Sample et al., in review) and serves as an important regulator on both alkalinity and pH in the pore water. This reaction is formulated in CrunchFlow as:

$$\text{Calcite} + H^{+} \rightarrow Ca^{+2} + HCO_3^{-} \qquad (5.5)$$

The required kinetic and thermodynamic parameters can be found from CrunchFlow database.

We observed a noticeable increase in pH (7.5 to ~8.5) from all sites across the SDB, which equates to a drop in proton activity from $10^{-7.5}$ to $10^{-8.5}$. The absolute magnitude of such change is uncertain due to the inherent poor quality of pH measurements. As pH is usually measured hours after pore water is separated from the cored sediments, the alteration of in-situ conditions, such as temperature and pressure, as well as the exposure to the atmospheric air all contribute to the uncertainty to this measurement. However, the large magnitude of the change in proton activity and the concordant change at all sites (Figure 5- 5) lead us to suspect the involvement of pore water pH in the reaction network.

The phase equilibrium of several aluminosilicate minerals calculated by Hess (1966) suggested that high pH environment favors zeolite precipitation, which is in agreement with our solubility tests. This pH dependence has been documented by Alt and Honnorez (1984) and Alt (2004) as a controlling factor of secondary zeolite formation in basaltic rocks. It is possible that clay mineral formation through hydrolysis may dominate the pH change at our study sites, especially in the last reaction zone where more basic pore water is observed. However because of lack of evidence for this reaction, we did not explicitly include clay hydrolysis in our model but simply added a proton sink and a resulting alkalinity source to account for the observed pH variation.

If alternatively, we do not include such a hydrogen sink, and allow the model to proceed without a pH constraint, the resulting simulations call for continuous dissolution of clinoptilolite, with the concomitant release of $SiO_{2(aq)}$ and potassium, contrary to the observed low pore water potassium and $SiO_{2(aq)}$. It is possible that other zeolite phases such as analcite, the Na-containing zeolite (Masuda et al., 1993; 1996), or heulandite, the Ba-containing zeolite (Nahr and Bohrmann, 1999), outcompete clinoptilolite, regulating the level of pore water $SiO_{2(aq)}$ and potassium in the last reaction zone.

5.5.4 Reaction network controlling the kinetics of amorphous silica

Here we present our reaction network model results and compare them with the observations of pore water and sediment chemistry from four sites in the Shikoku Basin (Figure 5- 1). Pore water composition is from Shipboard Scientific Party (2001) and Expedition 333 Scientists (2012a), and are listed in the ODP and IODP databases (http://www-odp.tamu.edu/database/). Concentration of dissolved $SiO_{2(aq)}$ and K consistently decrease across the SDB at the four study sites (Figure 5- 5). Ca and Na concentrations change monotonically with depth. These elements are apparently not involved in reactions at the SDB, rather their concentration profiles are largely controlled by diffusion exchange with altered fluids in the upper oceanic crust (Torres et al., in review). Amorphous silica concentration is from White et al. (2011) and Spinelli and

Hutton (2013). As the primary purpose of this study is to investigate the reaction network that determines the distribution of amorphous silica, it should be emphasized that the exact match between simulations and observations should not be expected since we did not consider the full set of geochemical processes.

By reproducing the observed pore water profiles with our model and the proposed reaction network, we define four reaction zones based on the profiles of reaction rates (Figures 5-5 and 5-6). The estimated reaction rates for each of the reaction in different zones were reported in Table 2. By defining the reaction zones this way, they will correspond to the locations where minerals actively precipitate or dissolve. This is different from the definition based on mineral assemblage observations (e.g., Masuda et al., 1993) as the highest mineral abundance reflects precipitation-dissolution changes but not necessary where the rate is highest. The reaction zones defined by these two approaches may not completely correlate, but it is instructive to compare one with the other as we will elaborate in later paragraphs.

In the shallowest sediments, where ash is still abundant, the $SiO_{2(aq)}$ released from ash dissolution (Eq. (5.3)) is consumed by precipitation of both amorphous silica and clinoptilolite (Figure 5- 6A). Amorphous silica rapidly precipitates in the upper half of this zone but begins to dissolve in the lower half of this zone due to the competition with clinoptilolite formation (Figure 5- 6B), which also consumes pore water potassium. In the second reaction zone, the SDB, (Figure 5- 6C) where the amorphous silica is exhausted, some amount of volcanic ash still survives but gradually dissolves whereas clinoptilolite regulates the pore water $SiO_{2(aq)}$ content. The rate of clinoptilolite formation drops accordingly, but it continues to precipitate. Our model suggests that about 4-7 vol% of clinoptilolite should precipitate in the first two reaction zones to sequester pore water $SiO_{2(aq)}$ and K. In the last reaction zone (Figure 5- 6D), the reactive volcanic ash is totally exhausted and the rate of clinoptilolite formation decreases to a very low level (Table 2), but clinoptilolite remains oversaturated with respect to the pore water at the elevated pH values observed (Figure 5- 5). Such saturation states are needed to prevent the release of

$SiO_{2(aq)}$ and potassium from the mineral clinoptilolite to the pore water phase, and maintain the pore water profiles observed.

The first reaction zones defined in this study correspond to the sediment interval where Masuda et al. (1996) observed formation of diagenetic smectite at Site 808 (Figure 5- 2). We ran a simulation including smectite to test the response in pore water profiles. This reaction is formulated in CrunchFlow as:

$$\text{Smectite} + 6.64\ H^{+} \rightarrow 0.02\ Ca^{+2} + 0.15\ Na^{+} + 0.1\ Fe^{+3} + 0.2\ K^{+} + 0.2\ Fe^{+2} + 0.9\ Mg^{+2} + 1.25\ Al^{+3} + 3.75\ SiO_{2(aq)} \quad (5.6)$$

As expected, smectite formation rapidly sequesters the pore water $SiO_{2(aq)}$ in the shallow sediments, thus hindering formation of amorphous silica and clinoptilolite. Only when smectite precipitation is suppressed, (e.g. by regulating the amount of available Fe^{+2}), is $SiO_{2(aq)}$ released from ash dissolution available for amorphous silica and clinoptilolite precipitation. In addition, formation of smectite alone does not explain the observed potassium profiles. The K to $SiO_{2(aq)}$ stoichiometric ratio for clinoptilolite formation (Eq. (5.4)) is four times higher than that needed for smectite (Eq. (5.6)), so that clinoptilolite sequesters four times more potassium per mole of mineral precipitated than smectite does. These results suggest that, although authigenic smectite is important for the overall silica budget, it is probably not the main control in our study sites given our observations of amorphous silica and pore water potassium profiles.

5.5.5 Role of sediment thermal history

A plot of $SiO_{2(aq)}$ content versus temperature at each of our study sites reveals that the SDB depth is not a simple function of temperature (Figure 5- 7A), as previously suggested by Masuda et al. (1996). To further explore the temperature dependence of silica diagenesis we apply the concept of thermal maturity traditionally used to estimate organic matter maturation (e.g., Waples, 1980; Hunt et al., 1991) to the sediment columns at Sites 808, 1173, 1177, C0011, and C0012. For each site, we calculate the temperature

history of a thickening sediment column using a 1-D thermal model that accounts for heat conduction, sediment accumulation, consolidation, and dewatering between a constant temperature boundary at the seafloor (2 ˚C) and a time-dependent basal heat input (*f*) from the underlying basement rock (e.g., Hutnak and Fisher, 2007; Spinelli et al., 2007). We use site-specific porosity-depth trends and sedimentation rate histories from drilling results (Table 3) (Shipboard Scientific Party, 2001; Underwood et al., 2010; Expedition 333 Scientists, 2012a). For most of the history of these sites, we assume the basal heat input (*f)* decreases with lithospheric age (*t*) as expected for conductively cooling oceanic lithosphere, such that:

$$f = \frac{C}{\sqrt{t}} \quad (5.7)$$

where *C* is commonly ~500 mW m^{-2} $Ma^{1/2}$ (e.g., Davis and Lister, 1974; Parsons and Sclater, 1977; Stein and Stein, 1994; Harris and Chapman, 2001). Heat input to the base of the sediment column may deviate from the expected values from conductive cooling due to the redistribution of heat in the basement by fluid circulation (e.g., Lister, 1972; Davis et al., 1999; Spinelli and Wang, 2008; Spinelli, in review) and/or post-spreading volcanism (e.g., Yamano et al., 2003). Clay mineral alteration trends at Site 1173 are most consistent with heat flux through the sediments that deviates <100 mW m^{-2} from conductive predictions; additionally, the currently observed ~50 mW m^{-2} anomaly at Site 1173 may be a recent (<5 Ma) phenomenon (Spinelli and Underwood, 2005). This is consistent with observations along the entire Nankai margin that heat flux within 30 km of the deformation front averages 20% above the expected values for conductively cooled lithosphere (Harris et al., 2013). This regional anomaly is thought to result from hydrothermal circulation mining heat from the subducted crust and delivering it to the incoming plate (Spinelli and Wang, 2008; Harris et al., 2013). Finally, Spinelli (in review) shows that the observed low heat flux at C0011 and high heat flux at C0012 and are consistent with the redistribution of heat by hydrothermal circulation in the upper basement. Where observations indicate anomalous heat flux through the sediment column relative to conductively cooling lithosphere (i.e. Sites C0011, C0012, and 1173), we have

the basal heat input to follow the conductive cooling curve until the most recent 2 Ma, at which point the basal heat flux is set to the observed value (Table 3).

Using the thermal histories for each site, we calculate a thermal maturity index (TTI) of each 2-meter-thick sediment element. At every time-step (Δt [Ma]), the TTI of a given sediment packet is increased by:

$$2^{\frac{T}{10}-10.5}\Delta t \quad (5.8)$$

where T is temperature (˚C). This formulation provides a smooth increase in the exponential term, rather than the incremental increases at 10 ˚C intervals classically calculated (e.g., Waples, 1980). The thermal maturity of one particular sediment package then can be quantified by integrating TTI with time. By comparing thermal maturity estimates (ΣTTI; e.g., Waples, 1980) (Figure 5- 7B) with the depth of the SDB at each site, there is a convergence of SDB at all four sites at a ΣTTI of 0.012 +/- 0.005, despite the wide range in temperatures currently present at the diagenetic boundary among all the sites (13-69 ˚C). For example, the temperatures at the SDB at Sites 1173 and C0011 are ~51 ˚C and ~22 ˚C, respectively (Table 4). However, the ages of sediment at the SDB at Sites 1173 and C0011 are ~3.2 Ma and ~5.7 Ma, respectively. The shorter time to achieve higher temperature at Site 1173 and the longer time at lower temperature at Site C0011 both yield a ΣTTI at the SDB of ~0.012.

Based on the age and temperature relationships in sediments from the onland wells located from Akita to Niigata Prefectures along east coast of Japan, Sasaki (1986) showed that the ash-clinoptilolite-analcite transition boundaries were controlled by a geological reaction time, a concept that is similar to the thermal history of sediments used here. Although the geological settings are different, the abundant pyroclastic materials from volcanic activity were also proposed to drive the reaction sequence onland (Sasaki, 1986). The Neogene marine sediment columns were classified into four reaction zones where volcanic glass only appears in zone one and replaced by clinoptilolite in zone two.

Clinoptilolite was replaced by another zeolite mineral, analcime, in zone three and sequentially transformed to albite in zone four. We thus consider this as an analogue that supports our inference that the silica reaction network is fundamentally controlled by sedimentary thermal maturity and can be parameterized with the ΣTTI approach.

We calculated the ΣTTI for all the seven onland wells investigated by Sasaki (1986). The ΣTTI values at the top of clinoptilolite zone ranges from 0.008 to 0.051 (the grey area in Figure 5- 7b), which also cover the values for the five sites drilled in the incoming sediments to the Nankai Trough. The sedimentation rate histories for these terrestrial sites are not as well constrained as for the ODP and IODP Sites, thus increasing uncertainty in the thermal maturity estimates. Nevertheless, these good agreements obtained here give further credence to our conclusion that thermal maturity plays a major role in controlling the transition from volcanic ash to zeolite phases in Nankai area.

5.6 Implications

The prevailing ash alteration in the Nankai sediments is likely to play an important role in the overall carbon budget in the sediments along convergent margins. As Wallmann et al. (2008) demonstrated, reactive silicate weathering is an important CO_2 sink that can totally neutralize the CO_2 produced during methanogenesis and carbonate precipitation. Furthermore, the alkalinity produced during ash alteration contributes significantly to the precipitation of carbonate minerals as observed by Sample et al. (in review) at Sites C0011 and C0012. The mass balance and cycling of carbon driven by silica alteration reactions is worthy of further study to fully quantify their global significance.

We also note the observation of Spinelli et al. (2007) that the sediments above the SDB have anomalously constant porosity, which displays a marked drop beneath this diagenetic boundary. Based on additional studies (e.g. White et al., 2011), they concluded that alteration of disseminated glass to an amorphous silica phase that coats grains, effectively inhibits sediment consolidation (Spinelli et al., 2007). In addition to anomalous porosity, the cemented sediment also has anomalous seismic velocity, and

rigidity (Spinelli et al., 2007). Cement dissolution leads to dramatic reduction in rigidity and a collapse of the sediment framework (i.e. porosity loss). Although the actual consequential relationship between silica diagenesis and physical properties of the Shikoku Basin sediments is not fully confirmed, the observed profiles suggest a connection, that if it is confirmed, will impact our understanding of the distribution and activity of faults over time and seismogenic processes, not only in the Nankai area but also along subduction zones worldwide.

5.7 Conclusions

We investigated the reactions, rates and controlling parameters of early silica diageneisis at four sites drilled on the incoming sediments to the Nankai Trough. Our transport-reaction model approach, validated against pore water and sediment geochemical data, identified the following factors controlling the growth of amorphous silica, and emphasized the significance of ash alteration in the Nankai area:

1. A marked decrease in dissolved silica concentration at all studied sites defines a silica diagenetic boundary (SDB) at the depth where volcanic ash content and pore water $SiO_{2(aq)}$ and K are dramatically reduced.
2. Volcanic ash alteration can be constrained by modeling pore water Sr isotope and amorphous silica profiles, and we show how this reaction serves as the dissolved silica source necessary for amorphous silica to precipitate. The formation of the amorphous silica coincides with a zone of constant porosity, and thus such amorphous silica phase has been put forward as a coating that solidifies sediment texture (Spinelli et al., 2007). Such silica coatings are suspected to influence geomechanical behavior of these sediments (Spinelli et al., 2007). Ash alteration may also contribute to enhanced carbonate formation in these sediments, as postulated by Sample et al., (in review).
3. Potassium-rich clinoptilolite competes for dissolved silica with the amorphous silica and forces amorphous silica to dissolve at the SDB, where the ash supply is depleted. Our model shows that a pH control on clinoptilolite stability, which may

originate from hydrolysis reactions during clay mineral formation, is essential in maintaining dissolution of silica cement below the diagenetic boundary.

4. We also demonstrate the importance of thermal maturity of the sediments, in controlling silica diagenesis, as indicated by the development of the SDB at approximately the same ΣTTI at all four study sites, which have significantly different thermal gradients.

5.8 Acknowledgements

This research used samples and data provided by the Integrated Ocean Drilling Program (IODP), which is sponsored by the US National Science Foundation and participating countries under management of IODP-MI. We gratefully acknowledge the efforts of the D/V Chikyu shipboard and drilling personnel and of the Scientific Parties of IODP Expeditions 322 and 333 and Carl Steefel (Earth Science Division, Lawrence Berkeley National Laboratory) for use of the Crunch flow code. Funding for this research was provided by the U.S. Science Support Program (USSP) and NSF grants OCE-1061189.

Figure 5-1Map showing the 4 sites investigated in this study (Sites 1173, 1177, C0011, and C0012) and three additional sites discussed (Site 297, 808, and 1174).

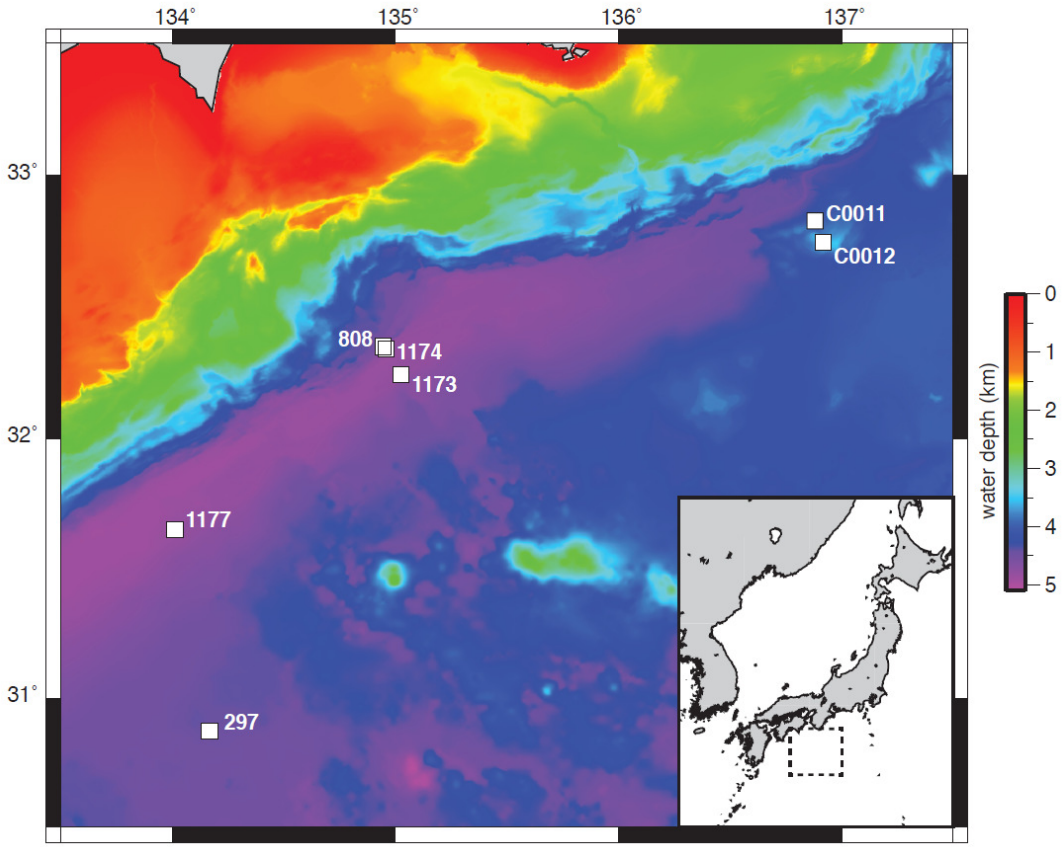

Figure 5-2 Pore water Si and K from site 808 and the predominated mineral assemblages identified by XRD in Masuda et al. (1993). (Clino. stands for clinoptilolite)

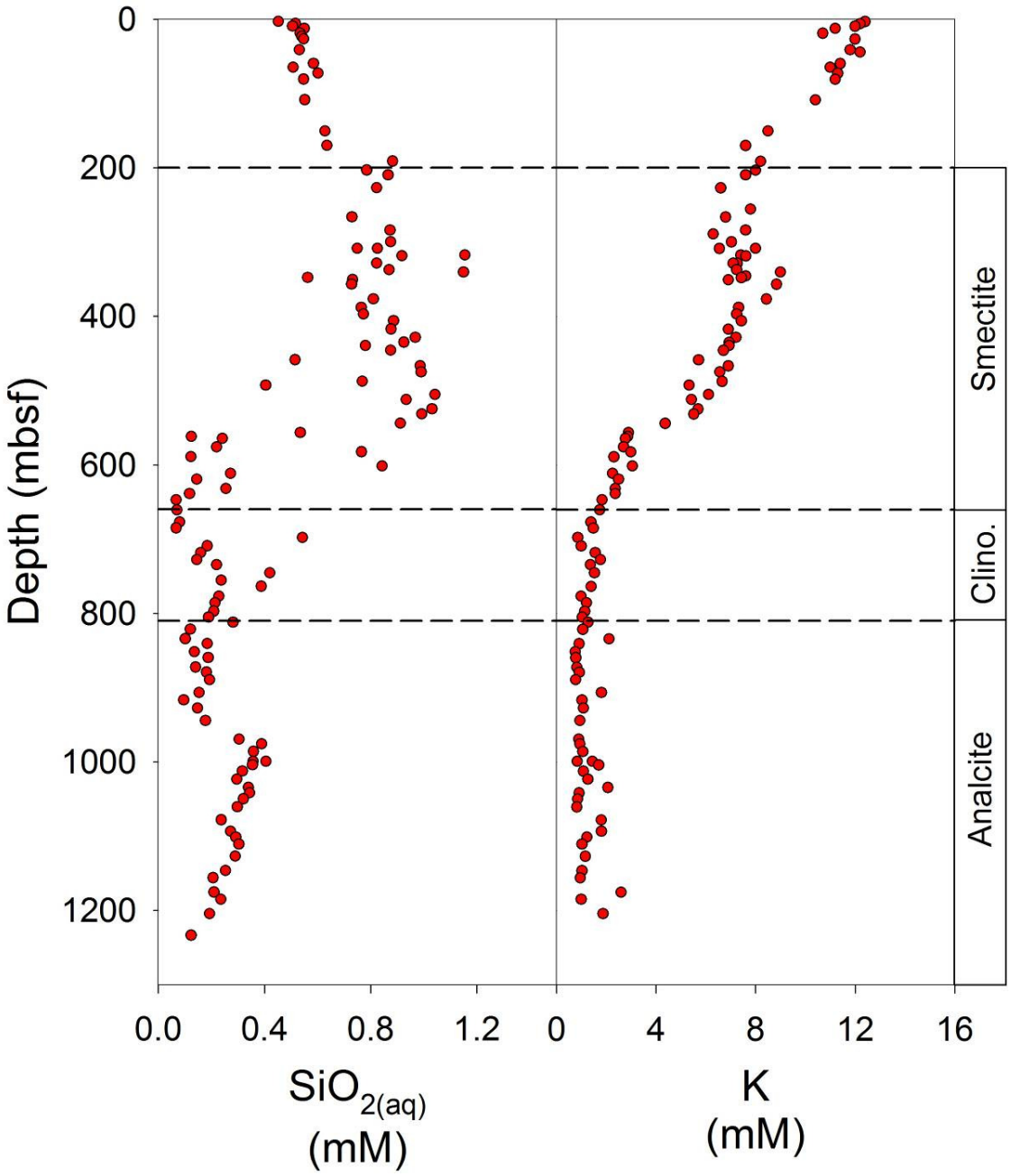

Figure 5-3 Strontium isotopic profiles at (A&B) Sites C0011 and (C&D) C0012 (Joseph et al., 2013). By simulating the observed profiles (black lines in (B) and (D)), our model helps constraining the rate of volcanic ash decomposition. Thin section observations from Site C0012 (E) (Expedition 333 Scientists, 2012c) demonstrate different degrees of volcanic ash alteration which correlates well with the Sr isotopic profile.

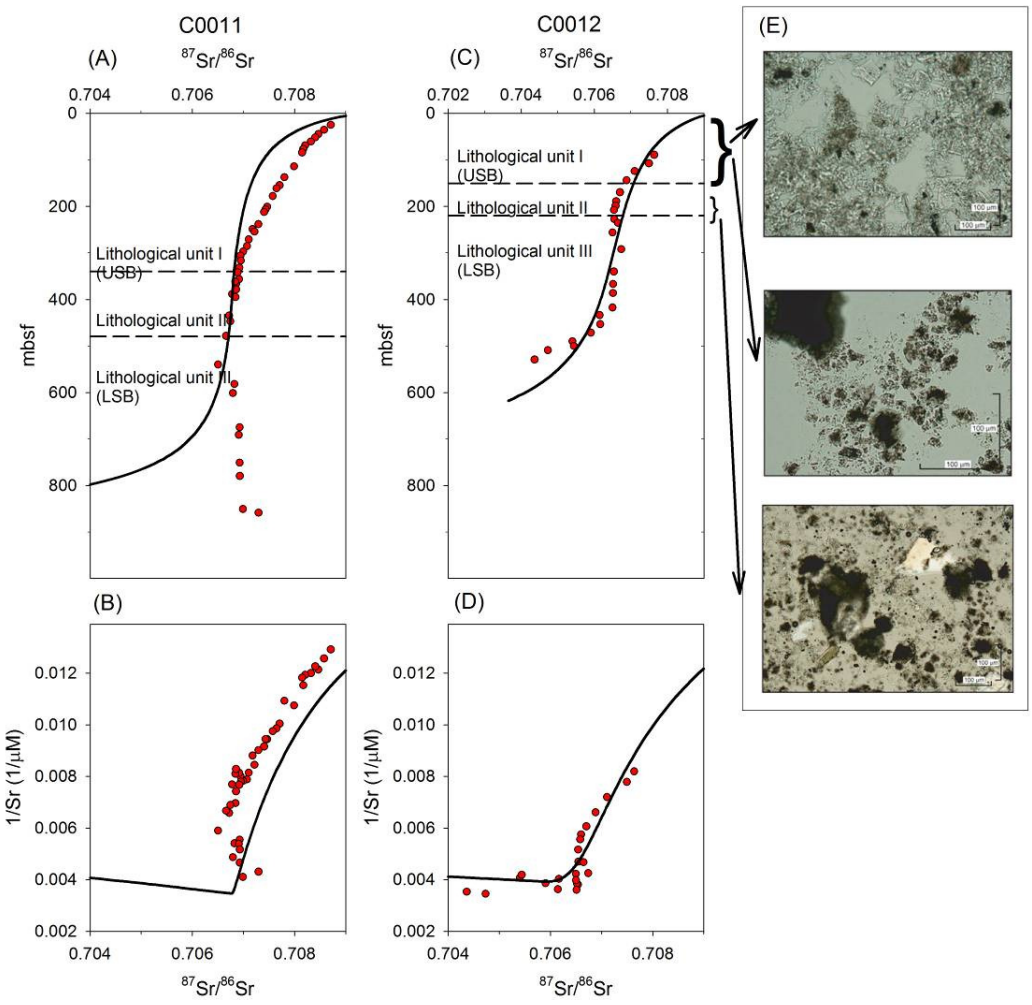

Figure 5-4 Illite, smectite, and clinoptilolite solubility at the current pore water composition in our four study sites. The activity product, Q, was calculated by CrunchFlow uses an extended Debye-Huckel model (Steefel, 2009). Solubility, K_{eq}, of each mineral was from CrunchFlow database. Among these minerals, only clinoptilolite is barely oversaturated, we thus chose it in the model so that by controlling pore water $SiO_{2(aq)}$ content clinoptilolite formation can regulate but not completely suppress the growth of amorphous silica.

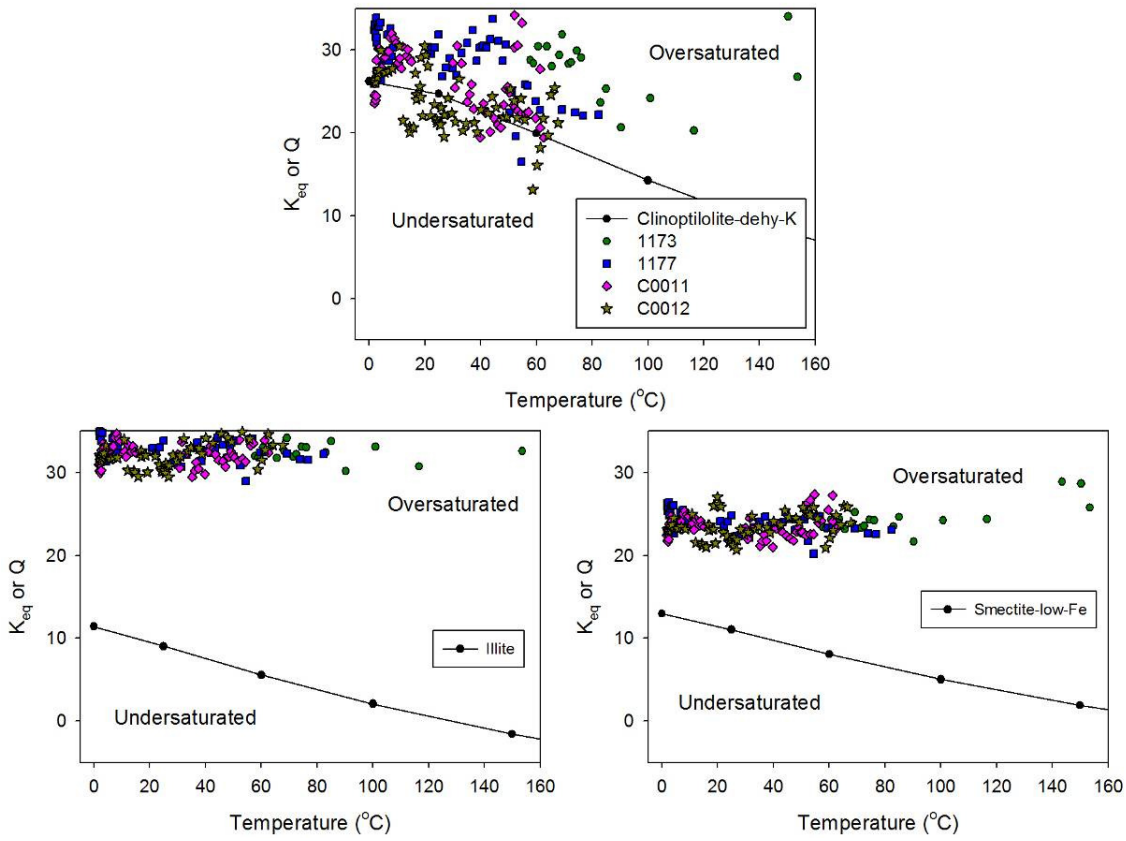

Figure 5-5 Observed (closed dots) and modeled (blue lines) profiles of key pore water species and volcanic ash for the four study sites. Modeled amorphous silica content is shown as red lines. Three reaction zones were defined from the reaction rates estimated by the model.

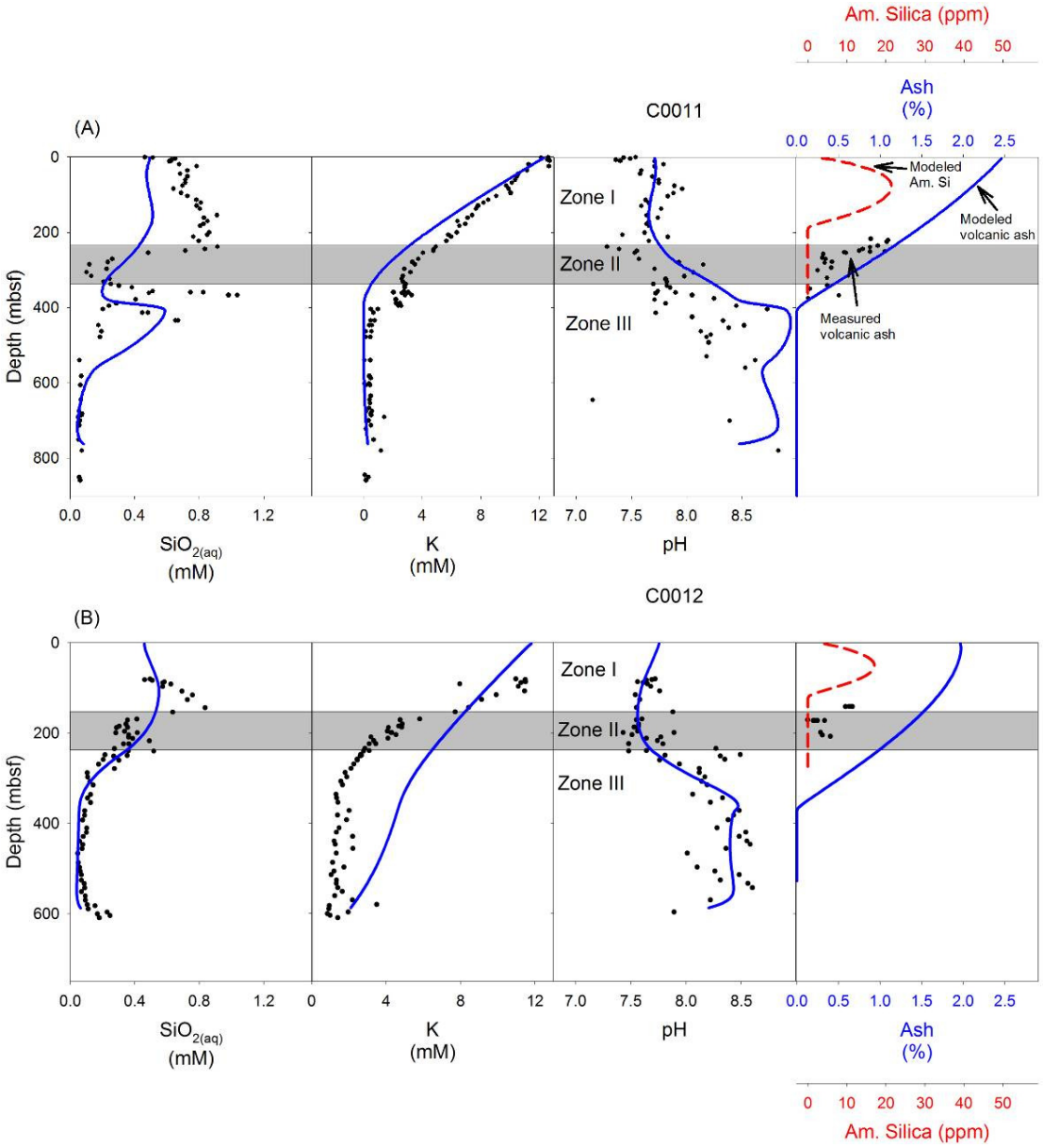

Figure 5-5 (Continued)

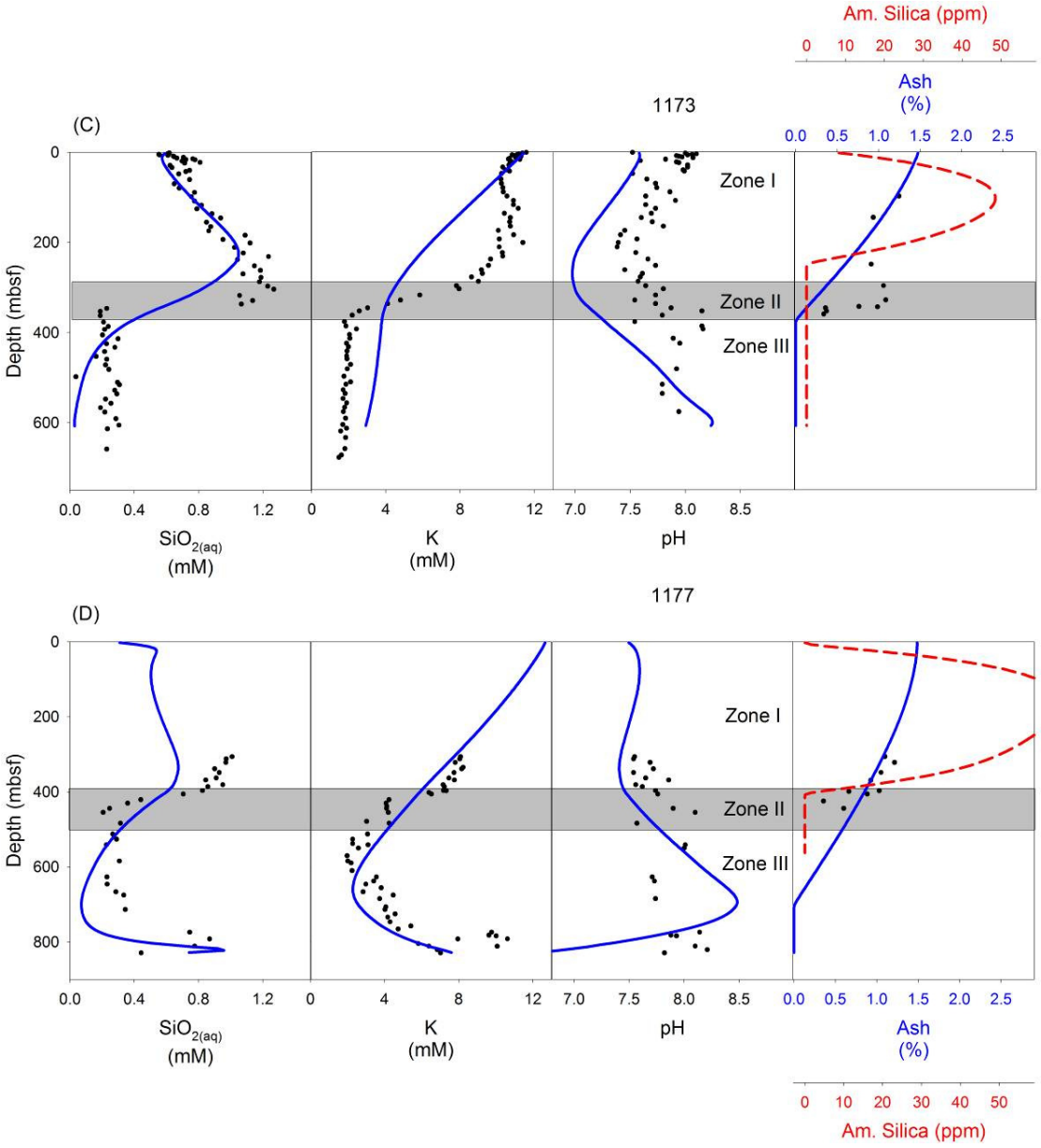

Figure 5-6 Reaction network proposed in the three reaction zones (see Figure 5-5 for the boundaries of these zones). Size of the arrows roughly depicts the relative magnitude of each reaction.

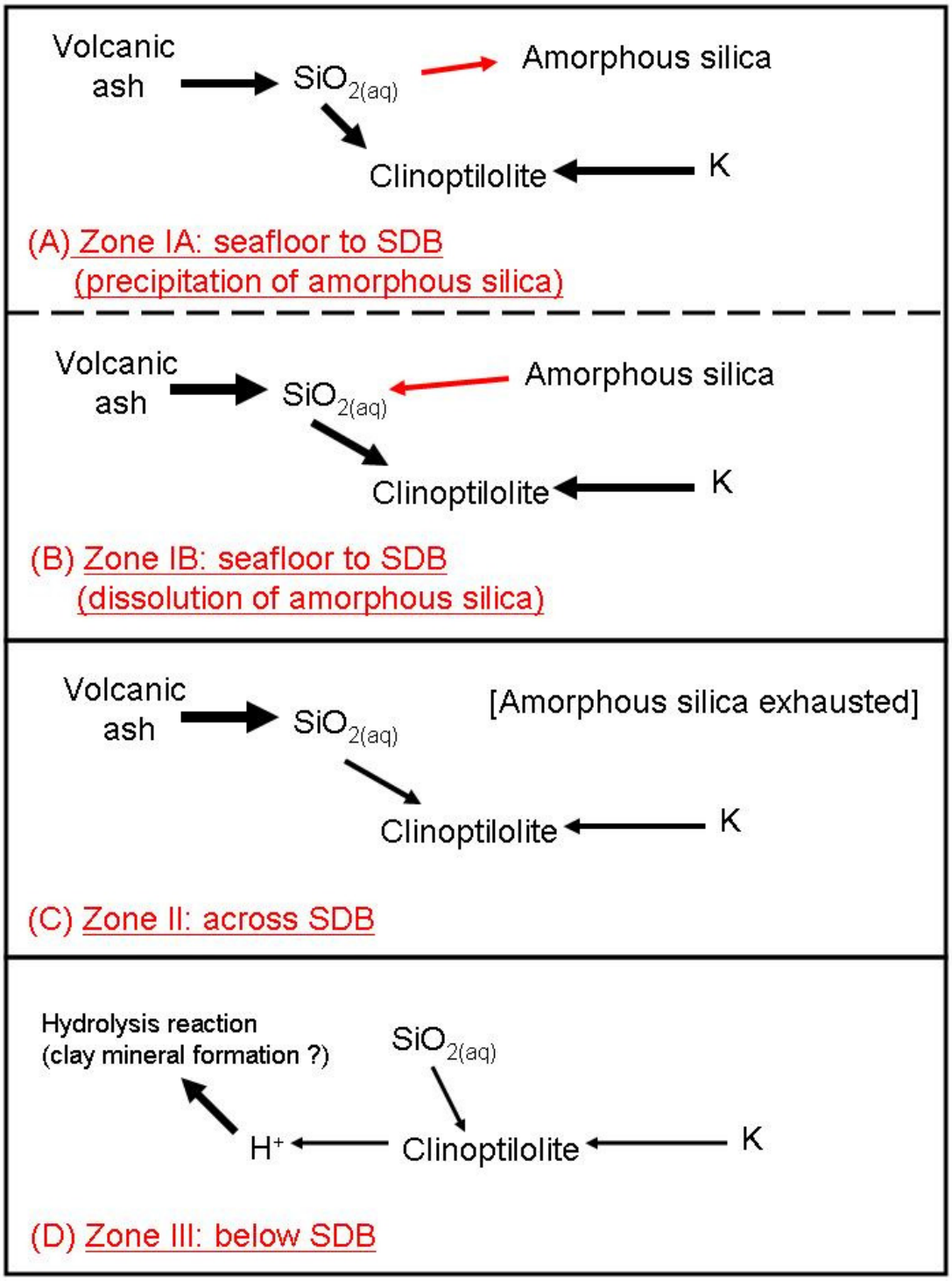
Volcanic ash
$SiO_{2(aq)}$
Amorphous silica
Clinoptilolite
K
(A) Zone IA: seafloor to SDB
(precipitation of amorphous silica)
Volcanic ash
$SiO_{2(aq)}$
Amorphous silica
Clinoptilolite
K
(B) Zone IB: seafloor to SDB
(dissolution of amorphous silica)
Volcanic ash
$SiO_{2(aq)}$
[Amorphous silica exhausted]
Clinoptilolite
K
(C) Zone II: across SDB
Hydrolysis reaction
(clay mineral formation ?)
$SiO_{2(aq)}$
H^+
Clinoptilolite
K
(D) Zone III: below SDB

Figure 5-7 Temperature and thermal maturity dependency of SDB at the four study sites and includes data from Site 808 (Figure 1). (A) The SDB (clearly delineated by a drop in dissolved silica concentration in the pore water) occurs at temperatures ranging from ~13 ˚C (Site C0012) to ~69 ˚C (Site 808). (B) Despite the difference in temperatures at the SDB between sites, the diagenetic boundary occurs within a narrow range of sediment thermal maturity. The gray band indicates the range of thermal maturity at the SDB for onland wells documented by Sasaki (1986).

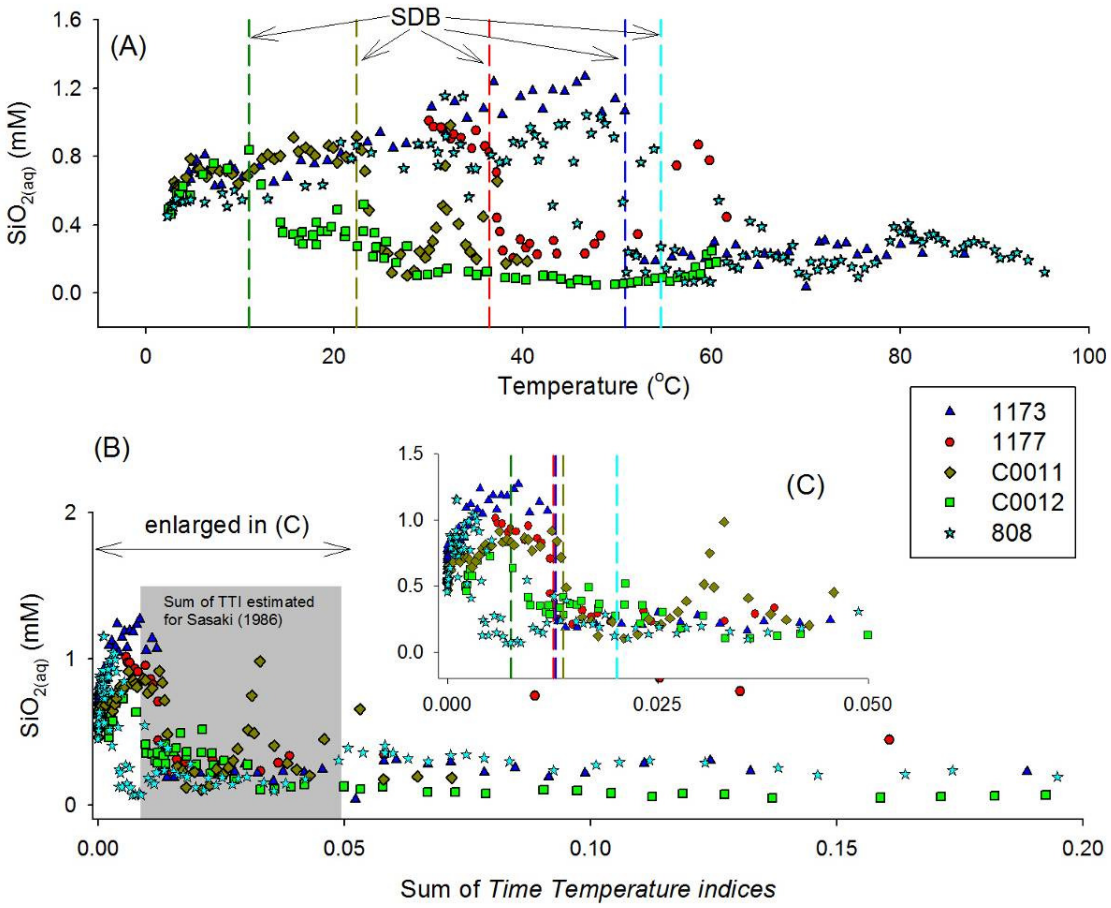

Table 5-1 Initial and boundary conditions of all sites

Primary Species	Surface condition/basement condition			
	1173	1177	C0011	C0012
$SiO_{2(aq)}$ (μM)	618/228	190/230	465/67.7	465/180.9
Cl (mM)	554.5/517.5	550/550	550/550	549/608
pH	8/7.94	7.5/7.99	7.5/8.53	7.7/7.89
Na^+	Charge balance species			
SO_4^{-2} (mM)	28/10	28/0	28/5	28/8
K^+ (mM)	11.57/1.47	12.7/8	12.6/0.39	12/1.4
Mg^{++} (mM)	48.8/6.15	50/20	52.3/4.34	49.98/7.2
Ca^{++} (mM)	8.86/86.6	10.5/17	10.8/82.7	10.5/177
Al^{+++} (μM)	1/1	1/1	1/1	1.1
HCO_3^- (mM)	4.71/12.23	5/6	2.9/0.99	2.58/0.26
H_2O (M)	53.6/53.6	53.6/53.6	53.6/53.6	53.6/53.6
Fe^{+++} (μM)	1/1	1/1	1/1	1/1
	Solid phase kinetic constants (10^x)			
Volcanic ash	-11.8	-12.13	-11.75	-11.85
$SiO_{2(am)}$	-11.8	-11.8	-11.8	-11.8
Clinoptilolite	-13	-13	-14	-12
Calcite	-11	-9	-8	-8
	Temperature, sedimentation rate, and porosity			
Length of sediment column (m)	725	830	800	620
Average burial rate (m/Myr)	48.3	41.6	60	30.9
Bottom water temperature (^oC)	1.78	1.78	1.72	1.89
Geothermal gradient (^oC/m)	0.183	0.054	0.076	0.140
Porosity parameter (A)	0.635	0.635	0.662	0.696
Porosity parameter (γ)	-0.0013	-0.0013	-0.0007	-0.0013

Table 5-2 Reaction rates (mmol Si/ m^2 sediments /yr) in each zone ("+" gain Si, "-" lost Si)

	Volcanic ash	Amorphous Si	Clinoptilolite	Diffusive flux
		Site 1173		
Zone IA	0.97	-0.18	-0.86	0.07
Zone IB	1.56	0.17	-0.10	-1.63
Zone II	1.09	<0.01	-0.07	-1.03
Zone III	0	0	-0.01	0.01
		Site 1177		
Zone IA	0.66	-0.20	-0.24	-0.22
Zone IB	1.24	0.20	-0.09	-1.35
Zone II	1.28	<0.01	-0.08	-1.20
Zone III	0	0	-0.01	0.01
		Site C0011		
Zone IA	1.45	-0.10	-1.29	-0.04
Zone IB	2.41	0.10	-0.15	-2.36
Zone II	3.71	<0.01	-0.22	-3.48
Zone III	0	0	-0.01	0.01
		Site C0012		
Zone IA	0.43	-0.04	-0.02	-0.36
Zone IB	0.82	0.06	-0.05	-083
Zone II	2.23	<0.01	-0.14	-2.09
Zone III	0	0	-0.01	0.01

Table 5-3 Histories of sedimentation rate and basal heat input

1173	time interval (Ma)	0-11.4	11.4-13	13-14.7	14.7-15		
	sediment accumulation rate (mm/yr)	0.0306	0.0785	0.0785	0.39		
	Basal heat input (mW/m2)	$\frac{500}{\sqrt{age}}$	$\frac{500}{\sqrt{age}}$	180	180		
1177	time interval (Ma)	0-16.7	16.7-17.9	17.9-20			
	sediment accumulation rate (mm/yr)	0.0276	0.0583	0.143			
	Basal heat input (mW/m2)	$\frac{500}{\sqrt{age}}$	$\frac{500}{\sqrt{age}}$	$\frac{500}{\sqrt{age}}$			
808	time interval (Ma)	0-1.4	1.4-12.4	12.4-14.5	14.5-14.7	14.7-14.9	14.9-15
	sediment accumulation rate (mm/yr)	0.0336	0.03826	0.0913	2.183	0.789	0.9
	q_base (mW/m2)	$\frac{500}{\sqrt{age}}$	$\frac{500}{\sqrt{age}}$	$\frac{500}{\sqrt{age}}$	$\frac{500}{\sqrt{age}}$	$\frac{500}{\sqrt{age}}$	$\frac{500}{\sqrt{age}}$

Table 5-3 (Continued)

C0011	time interval (Ma)	0-5.9	5.9-9	9-10.9	10.9-12.4	12.4-15.5	15.5-16.9	16.9-18	18-20
	sediment accumulation rate (mm/yr)	0.056	0.1	0.037	0.093	0.043	0.084	0.1	0.1
	Basal heat input (mW/m2)	$\frac{500}{\sqrt{age}}$	$\frac{500}{\sqrt{age}}$	$\frac{500}{\sqrt{age}}$	$\frac{500}{\sqrt{age}}$	$\frac{500}{\sqrt{age}}$	$\frac{500}{\sqrt{age}}$	$\frac{500}{\sqrt{age}}$	90
C0012	time interval (Ma)	0-5	5-9	9-14	14-16.6	16.6-18	18-20		
	sediment accumulation rate (mm/yr)	0.0056	0.07	0.0275	0.0154	0.0441	0.0441		
	Basal heat input (mW/m2)	$\frac{500}{\sqrt{age}}$	$\frac{500}{\sqrt{age}}$	$\frac{500}{\sqrt{age}}$	$\frac{500}{\sqrt{age}}$	$\frac{500}{\sqrt{age}}$	140		

Table 5-4 Temperature and sum of TTI at SDB of each site

Site	depth at SDB (mbsf)	T at SDB (˚C)	ΣTTI at SDB
C0011	238	22.4	0.0124
C0012	64	11.0	0.0067
1173	337	50.8	0.0119
1177	381	36.0	0.0107
808	602	53.9*	0.0053

* Temperature at Site 808 was calculated using 2 ^{o}C as bottom water temperature and 0.086 ^{o}C/m as geothermal gradient.

CHAPTER 6
General Conclusion

The work included in this dissertation demonstrates the power of a transport-reaction modeling approach to explore the different aspects of geochemical data. As I have shown, transport-reaction models are able to assess different hypotheses in complex and multivariable geochemical systems based on a thorough examination of all available information, including field and laboratory observations. In the same fashion, this modeling approach can also help validate the conclusions derived from laboratory experiments. The models I developed for Ulleung Basin (Chapter 2&3) and Shikoku Basin (Chapter 5) unraveled the most critical reactions at play in these environments, through a comprehensive consideration of pore water and sediment geochemistry, as well as physical properties of sediments and other pertinent geological information. Diffusional transport of solute and the different burial rates of solute and solids for each specific environment were considered. Reactions were expressed based on the formulation derived from laboratory works. The significance of these models lies in their power to connect the knowledge derived theoretically or experimentally with the field observations.

Another powerful application of the transport-reaction modeling approach is to resolve the temporal changes of a system. As I have demonstrated in the simulation of K-G Basin (Chapter 4) and the simulation experiment in Ulleung Basin (Chapter 3), the temporal evolution of the pore water profiles can be investigated based on principles of chemistry and physics and reasonable assumptions of the initial conditions. Such reconstruction is informative to quantify the geological events in the past (e.g., mass transfer in K-G Basin) and to investigate the consequences when a geochemical equilibrium in the pore water is disturbed by an enhanced flux (e.g., model experiment in Ulleung Basin). With field observations, transport-reaction modeling opens a new window for geochemists to track a process that occurred in the past, and predict system response to future perturbations.

Bibliography

Alt, J. (2004). Alteration of the upper oceanic crust: mineralogy, chemistry, and processes. Hydrogeology of the Oceanic Lithosphere. E. Davis and H. Elderfield. Cambridge, Cambridge University Press**:** 456-488.

Alt, J. C. and J. Honnorez (1984). "Alteration of the upper oceanic-crust, DSDP Site-417: mineralogy and chemistry." Contributions to Mineralogy and Petrology **87**(2): 149-169. doi: 10.1007/bf00376221.

Bahk, J. J., G.-Y. Kim, et al. (2013). "Characterization of gas hydrate reservoirs in the Ulleung Basin, East Sea (Korea), by integration of core and log data." Marine and Petroleum Geology **47**: 30-42.

Bahk, J.-J., J.-H. Kim, et al. (2009). "Occurrence of near-seafloor gas hydrates and associated cold vents in the Ulleung Basin, East Sea." Geosciences Journal **13**(4): 371-385. doi: 10.1007/s12303-009-0039-8.

Barnes, R. O. and E. D. Goldberg (1976). "Methane production and consumption in anoxic marine-sediments." Geology **4**(5): 297-300.

Bastia, R. (2004). "Depositional model and reservoir architecture of tertiary deep water sedimentation, Krishna-Godavari Offshore Basin, India." Journal of the Geological Society of India **64**(1): 11-20.

Benjamin, M. M. (2002). Water chemistry, McGraw-Hill New York.

Berner, R. A. (1971). Principles of chemical sedimentology McGraw-Hill.

Berner, R. A. (1980). Early Diagenesis. A Theoretical Approach. Princeton, N. J., Princeton University Press.

Bethke, C. (1996). Geochemical reaction modeling: Concepts and applications. New York, Oxford University Press

Bethke, C. (2008). Geochemical and biogeochemical reaction modeling. Cambridge, Cambridge University Press

Bhatnagar, G., W. G. Chapman, et al. (2008). "Sulfate-methane transition as a proxy for average methane hydrate saturation in marine sediments." Geophysical Research Letters **35**(3): L03611. doi: 10.1029/2007GL032500.

Bhatnagar, G., S. Chatterjee, et al. (2011). "Analytical theory relating the depth of the sulfate-methane transition to gas hydrate distribution and saturation." Geochemistry Geophysics Geosystems **12**: Q03003. doi: 10.1029/2010GC003397.

Borowski, W. S., C. K. Paull, et al. (1996). "Marine pore-water sulfate profiles indicate in situ methane flux from underlying gas hydrate." Geology **24**(7): 655-658.

Borowski, W. S., C. K. Paull, et al. (1997). "Carbon cycling within the upper methanogenic zone of continental rise sediments: An example from the methane-rich sediments overlying the Blake Ridge gas hydrate deposits." Marine Chemistry **57**(3-4): 299-311.

Borowski, W. S., C. K. Paull, et al. (1999). "Global and local variations of interstitial sulfate gradients in deep-water, continental margin sediments: Sensitivity to underlying methane and gas hydrates." Marine Geology **159**(1-4): 131-154. doi: 10.1016/s0025-3227(99)00004-3.

Boudreau, B. P. (1997). Diagenetic models and their implementation: modeling transport and reactions in aquatic sediments. Berlin, Springer.

Brumsack, H. J. and J. M. Gieskes (1983). "Interstitial water trace-metal chemistry of laminated sediments from the gulf of California, Mexico." Marine Chemistry **14**(1): 89-106. doi: 10.1016/0304-4203(83)90072-5.

Burdige, D. J. (2006). Geochemistry of marine sediments. Princeton New Jersey Princeton University Press.

Cambray, F. W., T. A. Vogel, et al. (1995). "Origin of compositional heterogeneities in tuffs of the timber mountain-group - the relationship between magma batches and magma transfer and emplacement in an extensional environment." Journal of Geophysical Research-Solid Earth **100**(B8): 15793-15805. doi: 10.1029/95JB00515.

Cartwright, J. (2011). "Diagenetically induced shear failure of fine-grained sediments and the development of polygonal fault systems." Marine and Petroleum Geology **28**(9): 1593-1610. doi: 10.1016/j.marpetgeo.2011.06.004.

Chatterjee, S., G. R. Dickens, et al. (2011). "Pore water sulfate, alkalinity, and carbon isotope profiles in shallow sediment above marine gas hydrate systems: A numerical modeling perspective." Journal of Geophysical Research-Solid Earth **116**. doi: B09103
10.1029/2011jb008290.

Choi, J., J.-H. Kim, et al. (2013). "Gas origin and migration in the Ulleung Basin, East Sea; results from the Second Ulleung Basin Gas Hydrate Drilling Expedition (UBGH2)." Marine and Petroleum Geology **47**: 113-124. doi: 10.1016/j.marpetgeo.2013.05.022.

Chuang, P. C., A. W. Dale, et al. (2013). "Relating sulfate and methane dynamics to geology: Accretionary prism offshore SW Taiwan." Geochemistry Geophysics Geosystems **14**(7): 2523-2545. doi: 10.1002/ggge.20168.

Chuang, P. C., T. F. Yang, et al. (2010). "Estimation of methane flux offshore SW Taiwan and the influence of tectonics on gas hydrate accumulation." Geofluids **10**(4): 497-510. doi: 10.1111/j.1468-8123.2010.00313.x.

Chuang, P. C., T. F. Yang, et al. (2006). "Extremely high methane concentration in bottom water and cored sediments from offshore southwestern Taiwan." Terrestrial Atmospheric and Oceanic Sciences **17**(4): 903-920.

Chun, J.-H., B.-J. Ryu, et al. (2011). "Sediment mounds and other sedimentary features related to hydrate occurrences in a columnar seismic blanking zone of the Ulleung Basin, East Sea, Korea." Marine and Petroleum Geology **28**(10): 1787-1800.

Claypool, G. and I. Kaplan (1974). The Origin and Distribution of Methane in Marine Sediments. Natural gases in marine sediments. I. R. Kaplan. New York, Plenum Publishing Corporation**:** 99.

Claypool, G. E., A. V. Milkov, et al. (2006). Microbial methane generation and gas transport in shallow sediments of an accretionary complex, southern Hydrate Ridge (ODP Leg 204), offshore Oregon, USA. Proceeding Ocean Drilling Program Scientific Results. G. Bohrmann, A. M. Tréhu, M. E. Torres and F. S. Colwell. **204**.

Claypool, G. E. and C. N. Threlkeld (1983). "Anoxic Diagenesis and Methane Generation in Sediments of the Blake Outer Ridge, Deep-Sea Drilling Project Site-533, Leg-76." Initial Reports of the Deep Sea Drilling Project **76**(Nov): 391-402.

Collett, T., M. Riedel, et al. (2008). Indian national gas hydrate program expedition 01 initial reports. New Delhi, India.

Colwell, F. S., S. Boyd, et al. (2008). "Estimates of biogenic methane production rates in deep marine sediments at Hydrate Ridge, Cascadia margin." Applied and Environmental Microbiology **74**(11): 3444-3452. doi: 10.1128/aem.02114-07.

Dale, A. W., V. Bruchert, et al. (2009). "An integrated sulfur isotope model for Namibian shelf sediments." Geochimica Et Cosmochimica Acta **73**(7): 1924-1944. doi: 10.1016/j.gca.2008.12.015.

Dale, A. W., P. Regnier, et al. (2008). "Anaerobic oxidation of methane (AOM) in marine sediments from the Skagerrak (Denmark): II. Reaction-transport modeling." Geochimica et Cosmochimica Acta **72**(12): 2880-2894. doi: DOI 10.1016/j.gca.2007.11.039.

Dale, A. W., P. Regnier, et al. (2006). "Bioenergetic controls on anaerobic oxidation of methane (AOM) in coastal marine sediments: A theoretical analysis." American Journal of Science **306**(4): 246-294.

Davis, E. E., D. S. Chapman, et al. (1999). "Regional heat flow variations across the sedimented Juan de Fuca Ridge eastern flank: Constraints on lithospheric cooling and lateral hydrothermal heat transport." Journal of Geophysical Research-Solid Earth **104**(B8): 17675-17688. doi: 10.1029/1999jb900124.

Davis, E. E. and C. R. B. Lister (1974). "Fundamentals of ridge crest topography." Earth And Planetary Science Letters **21**(4): 405-413. doi: 10.1016/0012-821x(74)90180-0.

De Laeter, J., J. Bohlke, et al. (2003). "Atomic weights of the elements: Review 2000." Pure Applied Chemistry **75**(6): 683-800.

Declercq, J., T. Diedrich, et al. (2013). "Experimental determination of rhyolitic glass dissolution rates at 40-200 degrees C and 2 < pH < 10.1." Geochimica Et Cosmochimica Acta **100**: 251-263. doi: 10.1016/j.gca.2012.10.006.

Dickens, G. R. (2001). "Sulfate profiles and barium fronts in sediment on the Blake Ridge: Present and past methane fluxes through a large gas hydrate reservoir." Geochimica Et Cosmochimica Acta **65**(4): 529-543.

Eberli, G. P., G. T. Baechle, et al. (2003). "Factors controlling elastic properties in carbonate sediments and rocks." The Leading Edge **22**(7): 654-660.

Forsberg, C., A. Solheim, et al. (2007). Slope instability and mass transport deposits on the Godavari River Delta, east Indian margin from a regional geological perspective. Submarine Mass Movements and Their Consequences, Springer**:** 19-27.

Fossing, H., T. G. Ferdelman, et al. (2000). "Sulfate reduction and methane oxidation in continental margin sediments influenced by irrigation (South-East Atlantic off Namibia)." Geochimica Et Cosmochimica Acta **64**(5): 897-910. doi: 10.1016/s0016-7037(99)00349-x.

Froelich, P. N., G. Klinkhammer, et al. (1979). "Early oxidation of organic matter in pelagic sediments of the eastern equatorial Atlantic: suboxic diagenesis." Geochimica et Cosmochimica Acta **43**(7): 1075-1090.

Galimov, E. M. and K. A. Kvenvolden (1983). "Concentrations and Carbon Isotopic Compositions of CH4 and CO2 in Gas from Sediments of the Blake Outer Ridge, Deep-Sea Drilling Project Leg-76." Initial Reports of the Deep Sea Drilling Project **76**(Nov): 403-407.

Garrels, R. M. and M. E. Thompson (1962). "A chemical model for sea water at 25 degrees C and one atmosphere total pressure." American Journal of Science **260**(1): 57-66. doi: 10.2475/ajs.260.1.57.

Giambalvo, E. R., C. I. Steefel, et al. (2002). "Effect of fluid-sediment reaction on hydrothermal fluxes of major elements, eastern flank of the Juan de Fuca Ridge." Geochimica Et Cosmochimica Acta **66**(10): 1739-1757. doi: Pii s0016-7037(01)00878-x
10.1016/s0016-7037(01)00878-x.

Haacke, R. R., R. D. Hyndman, et al. (2009). "Migration and venting of deep gases into the ocean through hydrate-choked chimneys offshore Korea." Geology **37**(6): 531-534. doi: 10.1130/G25681A.1.

Hallam, S. J., N. Putnam, et al. (2004). "Reverse methanogenesis: Testing the hypothesis with environmental genomics." Science **305**(5689): 1457-1462.

Hang, P. T. and G. Brindley (1970). "Methylene blue absorption by clay minerals. Determination of surface areas and cation exchange capacities (clay-organic studies XVIII)." Clays and Clay Minerals **18**(4): 203-212.

Harris, R., M. Yamano, et al. (2013). "A synthesis of heat flow determinations and thermal modeling along the Nankai Trough, Japan." Journal of Geophysical Research: Solid Earth **118**(6): 2687-2702. doi: 10.1002/jgrb.50230.

Harris, R. N. and D. S. Chapman (2001). "Mid-Latitude (30 degrees-60 degrees N) climatic warming inferred by combining borehole temperatures with surface air temperatures." Geophysical Research Letters **28**(5): 747-750. doi: 10.1029/2000gl012348.

Heeschen, K. U., R. W. Collier, et al. (2005). "Methane sources, distributions, and fluxes from cold vent sites at Hydrate Ridge, Cascadia Margin." Global Biogeochemical Cycles **19**(2): GB2016. doi: 10.1029/2004GB002266.

Helgeson, H. C. (1968). "Evaluation of irreversible reactions in geochemical processes involving minerals and aqueous solutions .i. Thermodynamic relations. " Geochimica Et Cosmochimica Acta **32**(8): 853-877. doi: 10.1016/0016-7037(68)90100-2.

Helgeson, H. C. and D. H. Kirkham (1974). "Theoretical prediction of thermodynamic behavior of aqueous electrolytes at high pressures and temperatures.1. summary of thermodynamic-electrostatic properties of solvent." American Journal of Science **274**(10): 1089-1198.

Helgeson, H. C. and D. H. Kirkham (1974). "Theoretical prediction of thermodynamic behavior of aqueous electrolytes at high pressures and temperatures. 2. debye-huckel parameters for activity-coefficients and relative partial molal properties." American Journal of Science **274**(10): 1199-1261.

Helgeson, H. C. and D. H. Kirkham (1976). "Theoretical prediction of the thermodynamic properties of aqueous electrolytes at high pressures and temperatures. III. Equation of state for aqueous species at infinite dilution." American Journal of Science **276**(2): 97-240. doi: 10.2475/ajs.276.2.97.

Helgeson, H. C., D. H. Kirkham, et al. (1981). "Theoretical prediction of the thermodynamic behavior of aqueous-electrolytes at high-pressures and temperatures. 4. calculation of activity-coefficients, osmotic coefficients, and

apparent molal and standard and relative partial molal properties to 600-degrees-C and 5 kb." American Journal of Science **281**(10): 1249-1516.

Hensen, C., M. Zabel, et al. (2003). "Control of sulfate pore-water profiles by sedimentary events and the significance of anaerobic oxidation of methane for the burial of sulfur in marine sediments." Geochimica et Cosmochimica Acta **67**(14): 2631-2647. doi: 10.1016/S0016-7037(00)00199-6.

Hess, P. C. (1966). "Phase equilibria of some minerals in K2O-Na2O-Al2O3-SiO2-H2O system at 25 degrees C and 1 atmosphere." American Journal of Science **264**(4): 289-309.

Hoehler, T. M., M. J. Alperin, et al. (1994). "Field and Laboratory Studies of Methane Oxidation in an Anoxic Marine Sediment - Evidence for a Methanogen-Sulfate Reducer Consortium." Global Biogeochemical Cycles **8**(4): 451-463.

Holler, T., G. Wegener, et al. (2009). "Substantial C-13/C-12 and D/H fractionation during anaerobic oxidation of methane by marine consortia enriched in vitro." Environmental Microbiology Reports **1**(5): 370-376. doi: 10.1111/j.1758-2229.2009.00074.x.

Holstein, J. M. and K. W. Wirtz (2010). "Organic matter accumulation and degradation in subsurface coastal sediments: a model-based comparison of rapid sedimentation and aquifer transport." Biogeosciences **7**(11): 3741-3753. doi: 10.5194/bg-7-3741-2010.

Hong, W. L., M. E. Torres, et al. (2013). "Carbon cycling within the sulfate-methane-transition-zone in marine sediments from the Ulleung Basin." Biogeochemistry **115**(1-3): 129-148. doi: 10.1007/s10533-012-9824-y.

Hong, W.-L., M. E. Torres, et al. (2013). "Carbon cycling within the sulfate-methane-transition-zone in marine sediments from the Ulleung Basin." Biogeochemistry: 1-20. doi: 10.1007/s10533-012-9824-y.

Hong, W.-L., M. E. Torres, et al. (2014). "Towards quantifying the reaction network around the sulfate-methane-transition-zone in the Ulleung Basin, East Sea, with a kinetic modeling approach." Gechimica et Cosmochimica Acta **in review**.

Horozal, S., G. H. Lee, et al. (2009). "Seismic indicators of gas hydrate and associated gas in the Ulleung Basin, East Sea (Japan Sea) and implications of heat flows derived from depths of the bottom-simulating reflector." Marine Geology **258**(1-4): 126-138. doi: 10.1016/j.margeo.2008.12.004.

House, C. H., V. J. Orphan, et al. (2009). "Extensive carbon isotopic heterogeneity among methane seep microbiota." Environmental Microbiology **11**(9): 2207-2215. doi: 10.1111/j.1462-2920.2009.01934.x.

Huggett, J. (1993). "Petrology and diagenesis of Palaeogene clays from Olst and Albaekhoved, Denmark." Bulletin of the Geological Society of Denmark **40**: 256-271.

Hunt, J. M., M. Lewan, et al. (1991). "Modeling Oil Generation with Time-Temperature Index Graphs Based on the Arrhenius Equation (1)." AAPG Bulletin **75**(4): 795-807.

Hutnak, M. and A. T. Fisher (2007). "Influence of sedimentation, local and regional hydrothermal circulation, and thermal rebound on measurements of seafloor heat

flux." Journal of Geophysical Research-Solid Earth **112**(B12): B12101. doi: 10.1029/2007jb005022.

Ike, T., G. F. Moore, et al. (2008). "Variations in sediment thickness and type along the northern Philippine Sea Plate at the Nankai Trough." Island Arc **17**(3): 342-357. doi: 10.1111/j.1440-1738.2008.00624.x.

Jahne, B., G. Heinz, et al. (1987). "Measurement of the Diffusion-coefficients of Sparingly Soluble Gases in Water." Journal of Geophysical Research-Oceans **92**(C10): 10767-10776. doi: 10.1029/JC092iC10p10767.

Jaynes, W. and J. Bigham (1987). "Charge reduction, octahedral charge, and lithium retention in heated, Li-saturated smectites." Clays and Clay Minerals **35**(6): 440-448.

Jeans, C. V., D. S. Wray, et al. (2000). "Volcanogenic clays in Jurassic and Cretaceous strata of England and the North Sea basin." Clay Minerals **35**(1): 25-55. doi: 10.1180/000985500546710.

Jin, Q. S. and C. M. Bethke (2005). "Predicting the rate of microbial respiration in geochemical environments." Geochimica Et Cosmochimica Acta **69**(5): 1133-1143. doi: 10.1016/j.gca.2004.08.010.

Johnson, J. W., E. H. Oelkers, et al. (1992). "SUPCRT92 - A software package for calculating the standard molal thermodynamic properties of minerals, gases, aqueous species, and reactions from 1-bar to 5000-bar and 0-degrees-C to 1000-degrees-C." Computers & Geosciences **18**(7): 899-947. doi: 10.1016/0098-3004(92)90029-q.

Jorgensen, B. B., A. Weber, et al. (2001). "Sulfate reduction and anaerobic methane oxidation in Black Sea sediments." Deep-Sea Research Part I-Oceanographic Research Papers **48**(9): 2097-2120. doi: 10.1016/s0967-0637(01)00007-3.

Joseph, C., M. E. Torres, et al. (2013). Data report: 87Sr/86Sr in pore fluids from NanTroSEIZE Expeditions 322 and 333. Proceeding of the Integrated Ocean Drilling Program S. Saito, M. B. Underwood, Y. Kubo and E. Scientists. Tokyo, Integrated Ocean Drilling Program Management International, Inc. **322**.

Kameda, J., S. Hina, et al. (2012). "Silica diagenesis and its effect on interplate seismicity in cold subduction zones." Earth And Planetary Science Letters **317**: 136-144. doi: 10.1016/j.epsl.2011.11.041.

Kastner, M. (1981). Authigenic silicates in deep-sea sediments: formation and diagenesis. The sea. **7:** 915-980.

Kennett, J. P., A. R. McBirney, et al. (1977). "Episodes of Cenozoic volcanism in circum-Pacific region." Journal of Volcanology and Geothermal Research **2**(2): 145-163. doi: 10.1016/0377-0273(77)90007-5.

KIGAM (2011). Studies on Gas Hydrate Geology and Geochemistry. KIGAM research report. Daejeon. **GP2010-002-2011(2):** 951.

Kim, J. H. (2007). Geochemical Characteristic of Organic Matter, Pore Waters and Methane Gas of Upper Quaternary Sediments from the Ulleung Basin, East Sea. Seoul, Seoul National University. **Ph.D. Dissertation**.

Kim, J. H., M. H. Park, et al. (2011). "Molecular and isotopic signatures in sediments and gas hydrate of the central/southwestern Ulleung Basin: high alkalinity escape

fuelled by biogenically sourced methane." Geo-Marine Letters **31**(1): 37-49. doi: 10.1007/s00367-010-0214-y.
Kim, J. H., M. E. Torres, et al. (2012). "Inferences on gas transport based on molecular and isotopic signatures of gases at acoustic chimneys and background sites in the Ulleung Basin." Organic Geochemistry **43**(1): 26-38. doi: 10.1016/j.orggeochem.2011.11.004.
Kim, J.-H., M.-H. Park, et al. (2007). "Geochemical characterization of the organic matter, pore water constituents and shallow methane gas in the eastern part of the Ulleung Basin, East Sea (Japan Sea)." Island Arc **16**(1): 93-104. doi: 10.1111/j.1440-1738.2007.00560.x.
Kim, J.-H., M. E. Torres, et al. (2013a). "Pore fluid chemistry from the Second Gas Hydrate Drilling Expedition in the Ulleung Basin (UBGH2): Source, mechanisms and consequences of fluid freshening in the central part of the Ulleung Basin, East Sea." Marine and Petroleum Geology **47**: 99-112. doi: j.marpetgeo.2012.12.011.
Kim, J.-H., M. E. Torres, et al. (2013b). "Depressurization experiment of pressure cores from the central Ulleung Basin, East Sea; insights into gas chemistry." Organic Geochemistry **62**: 86-95. doi: j.orggeochem.2013.07.010.
Kirkner, D. J. and H. Reeves (1988). "Multicomponent mass transport with homogeneous and heterogeneous chemical reactions: effect of the chemistry on the choice of numerical algorithm: 1. Theory." Water Resources Research **24**(10): 1719-1729.
Knab, N. J., B. A. Cragg, et al. (2009). "Regulation of anaerobic methane oxidation in sediments of the Black Sea." Biogeosciences **6**(8): 1505-1518.
Kotha, Y. (2002). "Sedimentology and sequence stratigraphy of hydrocarbon-bearing Mandapeta pays: A braided fluvial reservoir, Krishna-Godavari basin." Journal of the Geological Society of India **60**(3): 249-270.
Ledbetter, M. T. and R. S. J. Sparks (1979). "Duration of large-magnitude explosive eruptions deduced from graded bedding in deep-sea ash layers." Geology **7**(5): 240-244. doi: 10.1130/0091-7613(1979)7<240:doleed>2.0.co;2.
Li, Y. H. and S. Gregory (1974). "Diffusion of Ions in Sea-water and in Deep-sea Sediments." Geochimica Et Cosmochimica Acta **38**(5): 703-714.
Lichtner, P. C. (1985). "Continuum model for simultaneous chemical reactions and mass transport in hydrothermal systems." Geochimica Et Cosmochimica Acta **49**(3): 779-800.
Lim, Y. C., S. Lin, et al. (2011). "Variations of methane induced pyrite formation in the accretionary wedge sediments offshore southwestern Taiwan." Marine and Petroleum Geology **28**(10): 1829-1837. doi: 10.1016/j.marpetgeo.2011.04.004.
Lin, S., W. C. Hsieh, et al. (2006). "Methane migration and its influence on sulfate reduction in the Good Weather Ridge region, South China Sea continental margin sediments." Terrestrial Atmospheric and Oceanic Sciences **17**(4): 883-902.
Lister, C. R. B. (1972). "Thermal balance of a mid-ocean ridge." Geophysical Journal of the Royal Astronomical Society **26**(5): 515-&. doi: 10.1111/j.1365-246X.1972.tb05766.x.
Lloyd, K. G., M. J. Alperin, et al. (2011). "Environmental evidence for net methane production and oxidation in putative ANaerobic MEthanotrophic (ANME)

archaea." Environmental Microbiology **13**(9): 2548-2564. doi: 10.1111/j.1462-2920.2011.02526.x.

Luff, R., K. Wallmann, et al. (2000). "Numerical modeling of benthic processes in the deep Arabian Sea." Deep-Sea Research Part Ii-Topical Studies in Oceanography **47**(14): 3039-3072.

Mackin, J. E. and R. C. Aller (1984). "Diagenesis of dissolved aluminum in organic-rich estuarine sediments." Geochimica Et Cosmochimica Acta **48**(2): 299-313. doi: 10.1016/0016-7037(84)90252-7.

Maggi, F. and W. J. Riley (2009). "Transient competitive complexation in biological kinetic isotope fractionation explains nonsteady isotopic effects: Theory and application to denitrification in soils." Journal of Geophysical Research-Biogeosciences **114**: G04012. doi: 10.1029/2008jg000878.

Maher, K., C. I. Steefel, et al. (2009). "The role of reaction affinity and secondary minerals in regulating chemical weathering rates at the Santa Cruz Soil Chronosequence, California." Geochimica Et Cosmochimica Acta **73**(10): 2804-2831. doi: 10.1016/j.gca.2009.01.030.

Malinverno, A. and J. W. Pohlman (2011). "Modeling sulfate reduction in methane hydrate-bearing continental margin sediments: Does a sulfate-methane transition require anaerobic oxidation of methane?" Geochemistry Geophysics Geosystems **12**: Q07006. doi: 10.1029/2011gc003501.

Manheim, F. T. and F. L. Sayles (1974). Composition and origin of interstitial waters of marine sedimnets, based on Deep Sea Drill Cores. The sea. E. D. Goldberg. New York, John Wiley & Sons. **5:** 527-568.

Masuda, H., J. R. Oneil, et al. (1996). "Relation between interlayer composition of authigenic smectite, mineral assemblages, I/S reaction rate and fluid composition in silicic ash of the Nankai Trough." Clays and Clay Minerals **44**(4): 443-459. doi: 10.1346/ccmn.1996.0440402.

Masuda, H., H. Tanaka, et al. (1993). Major element chemistry and alteration mineralogy of volcanic ash, Site 808 in the Nankai Trough. Proceedings of Ocean Drilling Program Scientific Results 131B. I. A. Hill, A. Taira and J. V. Firth. College Station, TX, Ocean Drilling Program**:** 175-183.

Mazumdar, A., P. Dewangan, et al. (2009). "Evidence of paleo-cold seep activity from the Bay of Bengal, offshore India." Geochemistry Geophysics Geosystems **10**. doi: 10.1029/2008GC002337.

Mazumdar, A., H. M. Joao, et al. (2012). "Geochemical and geological constraints on the composition of marine sediment pore fluid: Possible link to gas hydrate deposits." Marine and Petroleum Geology **38**(1): 35-52. doi: 10.1016/j.marpetgeo.2012.07.004.

Mook, W. G. (1986). "C-13 in atmospheric CO2." Netherlands Journal of Sea Research **20**(2-3): 211-223. doi: 10.1016/0077-7579(86)90043-8.

Moore, G. F., A. Taira, et al. (2001). "New insights into deformation and fluid flow processes in the Nankai Trough accretionary prism: Results of Ocean Drilling Program Leg 190." Geochemistry Geophysics Geosystems **2**: 2001GC000166. doi: 2001gc000166.

Mork, M. B. E., D. A. Leith, et al. (2001). "Origin of carbonate-cemented beds on the Naglfar Dome, Voring Basin, Norwegian Sea." Marine and Petroleum Geology **18**(2): 223-234. doi: 10.1016/s0264-8172(00)00062-3.

Murthy, K. (1999). "Continental margin of Andhra Pradesh: Some new problems and perspectives." Visakha Science Journal **3**(1): 21-28.

Nahr, T. H. and G. Bohrmann (1999). "Barium-rich authigenic clinoptilolite in sediments from the Japan Sea - a sink for dissolved barium?" Chemical Geology **158**(3-4): 227-244. doi: 10.1016/s0009-2541(99)00051-0.

Nauhaus, K., A. Boetius, et al. (2002). "In vitro demonstration of anaerobic oxidation of methane coupled to sulphate reduction in sediment from a marine gas hydrate area." Environmental Microbiology **4**(5): 296-305.

Nehza, O., K. S. Woo, et al. (2012). "The origin of cold-water authigenic carbonates from deep-water, muddy sediments in the Ulleung Basin, East Sea of Korea." Geosciences Journal **16**(1): 25-34. doi: 10.1007/s12303-012-0005-8.

Niewohner, C., C. Hensen, et al. (1998). "Deep sulfate reduction completely mediated by anaerobic methane oxidation in sediments of the upwelling area off Namibia." Geochimica Et Cosmochimica Acta **62**(3): 455-464. doi: 10.1016/s0016-7037(98)00055-6.

Oleary, M. H. (1984). "Measurement of the Isotope Fractionation Associated with Diffusion of Carbon-dioxide in Aqueous Solution." Journal of Physical Chemistry **88**(4): 823-825. doi: 10.1021/j150648a041.

Orcutt, B., A. Boetius, et al. (2005). "Molecular biogeochemistry of sulfate reduction, methanogenesis and the anaerobic oxidation of methane at Gulf of Mexico cold seeps." Geochimica Et Cosmochimica Acta **69**(17): 4267-4281. doi: DOI 10.1016/j.gca.2005.04.012.

Orcutt, B., V. Samarkin, et al. (2008). "On the relationship between methane production and oxidation by anaerobic methanotrophic communities from cold seeps of the Gulf of Mexico." Environmental Microbiology **10**(5): 1108-1117. doi: DOI 10.1111/j.1462-2920.2007.01526.x.

Oremland, R. S., L. M. Marsh, et al. (1982). "Methane Production and Simultaneous Sulfate Reduction in Anoxic, Salt-marsh Sediments." Nature **296**(5853): 143-145. doi: 10.1038/296143a0.

Park, M. H., J. H. Kim, et al. (2005). "Tephrostratigraphy and paleo-environmental implications of Late Quaternary sediments and interstitial water in the western Ulleung Basin, East/Japan Sea." Geo-Marine Letters **25**(1): 54-62. doi: 10.1007/s00367-004-0203-0.

Parkhurst, D. L. and C. Appelo (1999). User's guide to PHREEQC (Version 2): A computer program for speciation, batch-reaction, one-dimensional transport, and inverse geochemical calculations.

Parsons, B. and J. G. Sclater (1977). "Analysis of variation of ocean-floor bathymetry and heat-flow with age." Journal of geophysical Research **82**(5): 803-827. doi: 10.1029/JB082i005p00803.

Party, S. S. (2001). Leg 190 Summary. Proceeding of the Ocean Drilling Program, Initial Reports. G. F. Moore, A. Taira, A. Klaus and S. S. Party. College Station, TX, Ocean Drilling Program**:** 1-87.

Pattan, J. N., G. Parthiban, et al. (2008). "A note on geochemistry of surface sediments from Krishna-Godavari basin, East Coast of India." Journal of the Geological Society of India **71**(1): 107-114.

Peters, J. L., R. W. Murray, et al. (2000). Terrigenous matter and dispersed ash in sediment from the Caribbean Sea; results from Leg 165. Proceeding of the Ocean Drilling Program Scientific Results. R. M. Leckie, H. Sigurdsson, G. D. Acton and G. Draper. College Station, TX, Ocean Drilling Program. **165:** 115-124.

Phillips, S. C. and J. E. Johnson (2014). "Data Report: Long-timescale particulate carbon and nitrogen variability in the Bay of Bengal and Arabian Sea." Marine and Petroleum Geology **(submitted)**.

Pimenov, N. V., I. Rusanov, et al. (1997). "Bacterial mats on coral-like structures at methane seeps in the Black Sea." Microbiology **66**(3): 354-360.

Pohlman, J. W., C. Ruppel, et al. (2008). "Assessing sulfate reduction and methane cycling in a high salinity pore water system in the northern Gulf of Mexico." Marine and Petroleum Geology **25**(9): 942-951. doi: 10.1016/j.marpetgeo.2008.01.016.

Prabhakar, K. and P. Zutshi (1993). "Evolution of southern part of indian east-coast basins." Journal of the Geological Society of India **41**(3): 215-230.

Ramana, M., T. Ramprasad, et al. (2009). "Multidisciplinary investigations exploring indicators of gas hydrate occurrence in the Krishna-Godavari Basin offshore, east coast of India." Geo-Marine Letters **29**(1): 25-38. doi: 10.1007/s00367-008-0121-7.

Ramprasad, T., P. Dewangan, et al. (2011). "Evidence of slumping/sliding in Krishna-Godavari offshore basin due to gas/fluid movements." Marine and Petroleum Geology **28**(10): 1806-1816. doi: 10.1016/j.marpetgeo.2011.02.007.

Reeburgh, W. S. (2007). "Oceanic methane biogeochemistry." Chemical Reviews **107**(2): 486-513.

Reed, M. H. (1982). "Calculation of multicomponent chemical equilibria and reaction processes in systems involving minerals, gases and an aqueous phase." Geochimica Et Cosmochimica Acta **46**(4): 513-528.

Rees, C. E. (1973). "Steady-State Model for Sulfur Isotope Fractionation in Bacterial Reduction Processes." Geochimica Et Cosmochimica Acta **37**(5): 1141-1162.

Regnier, P., A. W. Dale, et al. (2011). "Quantitative analysis of anaerobic oxidation of methane (AOM) in marine sediments: A modeling perspective." Earth-Science Reviews **106**(1-2): 105-130. doi: 10.1016/j.earscirev.2011.01.002.

Rickard, D. (1997). "Kinetics of pyrite formation by the H2S oxidation of iron (II) monosulfide in aqueous solutions between 25 and 125 degrees C: The rate equation." Geochimica Et Cosmochimica Acta **61**(1): 115-134. doi: 10.1016/s0016-7037(96)00321-3.

Rickard, D. and G. W. Luther (1997). "Kinetics of pyrite formation by the H2S oxidation of iron(II) monosulfide in aqueous solutions between 25 and 125 degrees C: The mechanism." Geochimica Et Cosmochimica Acta **61**(1): 135-147. doi: 10.1016/s0016-7037(96)00322-5.

Rickard, D. and G. W. Luther (2007). "Chemistry of iron sulfides." Chemical Reviews **107**(2): 514-562. doi: 10.1021/cr0503658.

Riedel, M., T. S. Collett, et al. (2013). "Large-scale depositional characteristics of the Ulleung Basin and its impact on electrical resistivity and Archie-parameters for gas hydrate saturation estimates." Marine and Petroleum Geology **47**: 222-235. doi: 10.1016/j.marpetgeo.2013.03.014.

Riedel, M., I. Novosel, et al. (2006). "Geophysical and geochemical signatures associated with gas hydrate-related venting in the northern Cascadia margin." Geological Society of America Bulletin **118**(1-2): 23-38. doi: 10.1130/1325720.1.

Rosenfeld, J. K. (1979). "Ammonium adsorption in nearshore anoxic sediments." Limnology and Oceanography **24**(2): 356-364.

Ryu, B.-J., G. Y. Kim, et al. (2012). Ulleung Basin Gas Hydrate Drilling Expedition 2 (UBGH2). . Expedition Report. Daejeon, KIGAM**:** 667.

Saberi, M. R., T. A. Johansen, et al. (2009). "Textural and burial effects on rock physics characterization of chalks." Petroleum Geoscience **15**(4): 355-365.

Sample, J., M. E. Torres, et al. (2013). "Diagenetic carbonate in Shikoku Basin sediments accurately records deep formation temperatures." **(Submitted)**.

Sasaki, A. (1986). "Effect of geological reaction-time on transformation temperature in zeolite diagenesis." Energy Sources **8**(2-3): 193-215. doi: 10.1080/00908318608946050.

Scholz, F., C. Hensen, et al. (2013). "Submarine weathering of silicate minerals and the extent of pore water freshening at active continental margins." Geochimica Et Cosmochimica Acta **100**(2013): 200-216. doi: 10.1016/j.gca.2012.09.043.

Schrag, D. P., J. A. Higgins, et al. (2013). "Authigenic Carbonate and the History of the Global Carbon Cycle." Science **339**(6119): 540-543. doi: 10.1126/science.1229578.

Schrum, H. N., A. J. Spivack, et al. (2009). "Sulfate-reducing ammonium oxidation: A thermodynamically feasible metabolic pathway in subseafloor sediment." Geology **37**(10): 939-942. doi: 10.1130/g30238a.1.

Schulz, H. D. and M. Zabel (2006). Marine geochemistry, Springer.

Scientists, E. (2010). Site C0011. Proceeding of the Integrated Ocean Drilling Program S. Saito, M. B. Underwood, Y. Kubo and E. Scientists. Tokyo, Integrated Ocean Drilling Program Management International, Inc. **322**.

Scientists, E. (2012a). Expedition 333 summary. Proceeding of the Integrated Ocean Drilling Program P. Henry, T. Kanamatsu, K. Moe and E. Scientists. Tokyo, Integrated Ocean Drilling Program Management International, Inc. **333**.

Scientists, E. (2012b). Site C0011. Proceeding of the Integrated Ocean Drilling Program P. Henry, T. Kanamatsu, K. Moe and E. Scientists. Tokyo, Integrated Ocean Drilling Program Management International, Inc. **333**.

Scientists, E. (2012c). Site C0012. Proceeding of the Integrated Ocean Drilling Program P. Henry, T. Kanamatsu, K. Moe and E. Scientists. Tokyo, Integrated Ocean Drilling Program Management International, Inc. **333**.

Scudder, R. P., R. W. Murray, et al. (2009). "Dispersed ash in deeply buried sediment from the northwest Pacific Ocean: An example from the Izu-Bonin arc (ODP Site 1149)." Earth And Planetary Science Letters **284**(3-4): 639-648. doi: 10.1016/j.epsl.2009.05.037.

Shanmugam, G., S. K. Shrivastava, et al. (2009). "Sandy debrites and tidalites of pliocene reservoir sands in upper-slope canyon environments, offshore krishna-godavari

basin (india): implications." Journal of Sedimentary Research **79**(9-10): 736-756. doi: 10.2110/jsr.2009.076.

Shikazono, N., A. Takino, et al. (2005). "An estimate of dissolution rate constant of volcanic glass in volcanic ash soil from the Mt. Fuji area, central Japan." Geochemical Journal **39**(2): 185-196. doi: 10.2343/geochemj.39.185.

Snyder, G. T., A. Hiruta, et al. (2007). "Pore water profiles and authigenic mineralization in shallow marine sediments above the methane-charged system on Umitaka Spur, Japan Sea." Deep-Sea Research Part Ii-Topical Studies in Oceanography **54**(11-13): 1216-1239. doi: 10.1016/j.dsr2.2007.04.001.

Solheim, A., C. Forsberg, et al. (2007). The role of geological setting and depositional history in offshore slope instability. Offshore Technology Conference.

Solomon, E. A., A. J. Spivack, et al. (2014). "Synthesis of pore fluid geochemistry in the Krishna-Godavari Basin - Gas hydrate distribution and carbon sequestration through coupled microbial methanogenesis and silicate weathering." Marine and Petroleum Geology **(Submitted)**.

Spinelli, G. A. (2013). "Long-distance fluid and heat transport in the oceanic crust entering the Nankai subduction zone, NanTroSEIZE transect." **(Submitted)**.

Spinelli, G. A. and A. Hutton (2013). Data report: amorphous silica content of sediment from Sites C0011 and C0012 in the Shikoku Basin on the NanTroSEIZE transect. Proceeding of the Integrated Ocean Drilling Program S. Saito, M. B. Underwood, Y. Kubo and E. Scientists. Tokyo, Integrated Ocean Drilling Program Management International, Inc. **322**.

Spinelli, G. A., P. S. Mozley, et al. (2007). "Diagenesis, sediment strength, and pore collapse in sediment approaching the Nankai Trough subduction zone." Geological Society of America Bulletin **119**(3-4): 377-390. doi: 10.1130/b25920.1.

Spinelli, G. A. and M. B. Underwood (2005). "Modeling thermal history of subducting crust in Nankai Trough: Constraints from in situ sediment temperature and diagenetic reaction progress." Geophysical Research Letters **32**(9). doi: L09301 10.1029/2005gl022793.

Spinelli, G. A. and K. Wang (2008). "Effects of fluid circulation in subducting crust on Nankai margin seismogenic zone temperatures." Geology **36**(11): 887-890. doi: 10.1130/g25145a.1.

Staudigel, H., S. R. Hart, et al. (1981). "Alteration of the oceanic-crust - processes and timing." Earth And Planetary Science Letters **52**(2): 311-327. doi: 10.1016/0012-821x(81)90186-2.

Steefel, C. and S. Yabusaki (1996). OS3D/GIMRT, software for multicomponent-multidimensional reactive transport. User Manual and Programmer's Guide. Richland, WA, Pacific Northwest National Laboratory.

Steefel, C. I. (1992). Coupled fluid flow and chemical reaction: Model development and application to water-rock interaction, Yale University.

Steefel, C. I. (2009). CrunchFlow- Software for Modeling Multicomponent Reactive Flow and Transport: User's Manual**:** 91.

Steefel, C. I. and A. C. Lasaga (1994). "A coupled model for transport of multiple chemical species and kinetic precipitation/dissolution reactions with application to

reactive flow in single phase hydrothermal systems." American Journal of Science **294**(5): 529-592.

Steefel, C. I. and K. Maher (2009). Fluid-Rock Interaction: A Reactive Transport Approach. Thermodynamics and Kinetics of Water-Rock Interaction. E. H. Oelkers and J. Schott. **70:** 485-532.

Stein, C. A. and S. Stein (1994). "Comparison of plate and asthenospheric flow models for the thermal evolution of oceanic lithosphere." Geophysical Research Letters **21**(8): 709-712. doi: 10.1029/94gl00632.

Torres, M. E., J.-H. Kim, et al. (2011). Occurrence of High Salinity Fluids Associated with Massive Near-seafloor Gas Hydrate Deposits. 7th International Conference on Gas Hydrates. Edinburgh, Scotland, United Kingdom.

Torres, M. E., A. C. Mix, et al. (2005). "Precise delta C-13 analysis of dissolved inorganic carbon in natural waters using automated headspace sampling and continuous-flow mass spectrometry." Limnology and Oceanography-Methods **3**: 349-360.

Torres, M. E., J. W. Moreau, et al. (2013). "Fluid-flow through the Philippine Sea plate prior to subduction along the Nankai Trough: Impact on the deep biosphere." **(Submitted)**.

Torres, M. E., A. M. Trehu, et al. (2008). "Methane hydrate formation in turbidite sediments of northern Cascadia, IODP Expedition 311." Earth And Planetary Science Letters **271**(1-4): 170-180.

Tudge, J., M. Lovell, et al. (2013). Data report: Site C0011 LWD resistivity-derived porosity. Proceeding of the Integrated Ocean Drilling Program. S. Saito, M. B. Underwood, Y. Kubo and E. Scientists. Tokyo, Integrated Ocean Drilling Program Management International, Inc. **322**.

UBGH2, S. (2010). Ulleung Basin Gas Hydrate Drilling Expedition 2. Preliminary Report. Daejeon, Republic of Korea, KIGAM.

Underwood, M. B. (2007). Sediment inputs to subduction zones: why lithostratigraphy and clay mineralogy matter. The Seismogenic Zone of Subduction Thrust Faults. T. Dixon and J. C. Moore. New York Columbia University Press**:** 42-85.

Underwood, M. B., S. Saito, et al. (2010). Expedition 322 summary. Proceeding of the Integrated Ocean Drilling Program S. Saito, M. B. Underwood, Y. Kubo and E. Scientists. Tokyo, Integrated Ocean Drilling Program Management International, Inc. **322**.

Valle, N., A. Verney-Carron, et al. (2010). "Elemental and isotopic (Si-29 and O-18) tracing of glass alteration mechanisms." Geochimica Et Cosmochimica Acta **74**(12): 3412-3431. doi: 10.1016/j.gca.2010.03.028.

Vavilin, V. (2013). "Estimating changes of isotopic fractionation based on chemical kinetics and microbial dynamics during anaerobic methane oxidation: apparent zero-and first-order kinetics at high and low initial methane concentrations." Antonie van Leeuwenhoek **103**(2): 375-383.

Venkatarathnam, K. and P. E. Biscaye (1973). Clay mineralogy and sedimentation in the eastern Indian Ocean. Deep Sea Research and Oceanographic Abstracts, Elsevier.

Von Breymann, M. T., R. Collier, et al. (1990). "Magnesium adsorption and ion-exchange in marine-sediments - a multicomponent model." Geochimica et Cosmochimica Acta **54**(12): 3295-3313. doi: 10.1016/0016-7037(90)90286-t.

Von Breymann, M. T. and E. Suess (1988a). "Magnesium in the marine sedimentary environment - Mg-NH4 ion-exchange." Chemical Geology **70**(4): 359-371. doi: 10.1016/0009-2541(88)90125-8.

Von Breymann, M. T., C. A. Ungerer, et al. (1988b). "Mg-NH4 exchange on humic-acid - a radiotracer technique for conditional exchange constants in a seawater medium." Chemical Geology **70**(4): 349-357. doi: 10.1016/0009-2541(88)90124-6.

Wallace, P. J., G. R. Dickens, et al. (2000). Effects of Core Retrieval and Degassing on the Carbon Isotope Composition of Methane in Gas Hydrate- and Free Gas-Bearing Sediments from Blake Ridge. Proceedings of the Ocean Drilling Program, Scientific Results. C. K. Paul, R. Matumoto, P. J. Wallace and W. P. Oillon. **164**.

Wallmann, K., G. Aloisi, et al. (2006). "Kinetics of organic matter degradation, microbial methane generation, and gas hydrate formation in anoxic marine sediments." Geochimica et Cosmochimica Acta **70**(15): 3905-3927.

Wallmann, K., G. Aloisi, et al. (2008). "Silicate weathering in anoxic marine sediments." Geochimica et Cosmochimica Acta **72**(12): 2895-2918. doi: 10.1016/j.gca.2008.03.026.

Waples, D. W. (1980). Time and temperature in petroleum formation: application of Lopatin's method to petroleum exploration. The Petroleum System- from Source to Trap. L. B. Magoon and W. G. Dow. Tulsa, Oklahoma, American Association Of Petroleum Geologists. **60:** 916-926.

Wegener, G. and A. Boetius (2009). "An experimental study on short-term changes in the anaerobic oxidation of methane in response to varying methane and sulfate fluxes." Biogeosciences **6**(5): 867-876.

Wehrmann, L. M., N. Risgaard-Petersen, et al. (2011). "Coupled organic and inorganic carbon cycling in the deep subseafloor sediment of the northeastern Bering Sea Slope (IODP Exp. 323)." Chemical Geology **284**(3-4): 251-261. doi: 10.1016/j.chemgeo.2011.03.002.

White, R. J., G. A. Spinelli, et al. (2011). "Importance of volcanic glass alteration to sediment stabilization: offshore Japan." Sedimentology **58**(5): 1138-1154. doi: 10.1111/j.1365-3091.2010.01198.x.

Whiticar, M. J. (1999). "Carbon and hydrogen isotope systematics of bacterial formation and oxidation of methane." Chemical Geology **161**(1-3): 291-314.

Wolery, T. J. (1978). Some chemical aspects of hydrothermal processes at mid-oceanic ridges: A theoretical study. Evanston, Illinois, Northwestern University. **PhD thesis**.

Wolery, T. J. (1979). Calculation of chemical equilibrium between aqueous solution and minerals: the EQ3/6 software package. [In FORTRAN extended 4. 6 for CDC6600 and 7600]**:** Medium: ED; Size: Pages: 46.

Wolery, T. J. (1992). EQ3/6: A software package for geochemical modeling of aqueous systems: package overview and installation guide (version 7.0), Lawrence Livermore National Laboratory Livermore, CA.

Yamano, M., M. Kinoshita, et al. (2003). "Extremely high heat flow anomaly in the middle part of the Nankai Trough." Physics and Chemistry of the Earth **28**(9-11): 487-497. doi: 10.1016/s1474-7065(03)00068-8.

Yang, L., C. I. Steefel, et al. (2010). "Kinetics of Fe(II)-Catalyzed Transformation of 6-line Ferrihydrite under Anaerobic Flow Conditions." Environmental Science & Technology **44**(14): 5469-5475. doi: 10.1021/es1007565.

Yang, T., S. Y. Jiang, et al. (2008). "Dissolved inorganic carbon (DIC) and its carbon isotopic composition in sediment pore waters from the Shenhu area, northern South China Sea." Journal of Oceanography **64**(2): 303-310.

Yang, T. F., P. C. Chuang, et al. (2006). "Methane venting in gas hydrate potential area offshore of SW Taiwan: Evidence of gas analysis of water column samples." Terrestrial Atmospheric and Oceanic Sciences **17**(4): 933-950.

Yi, S., J.-J. Bahk, et al. (2012). "Pliocene-Pleistocene boundary determination in hemipelagic sediment from the Ulleung Basin (East Sea, offshore Korea) inferred from terrigenous and marine palynofloras." Review of Palaeobotany and Palynology **181**: 54-63. doi: 10.1016/j.revpalbo.2012.05.002.

Yokoyama, T. and J. F. Banfield (2002). "Direct determinations of the rates of rhyolite dissolution and clay formation over 52,000 years and comparison with laboratory measurements." Geochimica Et Cosmochimica Acta **66**(15): 2665-2681. doi: Pii s0016-7037(02)00867-0

10.1016/s0016-7037(02)00867-0.

Yoo, D. G., N. K. Kang, et al. (2013). "Occurrence and seismic characteristics of gas hydrate in the Ulleung Basin, East Sea." Marine and Petroleum Geology **47**: 236-247. doi: 10.1016/j.marpetgeo.2013.07.001.

Zabel, M. and H. D. Schulz (2001). "Importance of submarine landslides for non-steady state conditions in pore water systems - lower Zaire (Congo) deep-sea fan." Marine Geology **176**(1-4): 87-99. doi: 10.1016/s0025-3227(01)00164-5.

Zeebe, R. E. and D. Wolf-Gladrow (2001). CO2 in Seawater Equilibrium, Kinetics, Isotopes. New York, Elsevier Science.

Zehnder, A. J. B. and T. D. Brock (1979). "Methane Formation and Methane Oxidation by Methanogenic Bacteria." Journal of Bacteriology **137**(1): 420-432.

Zhang, J., P. D. Quay, et al. (1995). "Carbon-isotope fractionation during gas-water exchange and dissolution of CO2." Geochimica Et Cosmochimica Acta **59**(1): 107-114. doi: 10.1016/00167-0379(59)1550d-.

Appendices

Appendix 1 Table of parameters used in the box model in Chapter 2.

Variables	Symbol	Value or Explanation
α	Degree of isotopic fractionation	
	α_{POCSR}	1
	α_{CP}	1
	α_{AMO}	1.004-1.03
	α_{ME}	1.055-1.095
	α_{CR}	1.055-1.095
b	Proportion of AMO that is being recycled through CR	
$\frac{\Delta(\phi C)}{\Delta z}$	Concentration gradient (porosity corrected)	
$^{12/13}C$	Concentration of carbon 12 or carbon 13	
	$^{12/13}C_{CH4\text{-}SMTZ}$	Concentration of carbon 12 or 13 of CH_4 at SMTZ
	$^{12/13}C_{CH4\text{-}bot}$	Concentration of carbon 12 or 13 of CH_4 at the same depth as $r_{CH4\text{-}bot}$
	$^{12/13}C_{DIC}$	Concentration of carbon 12 or 13 of DIC
$\delta^{13}C$	$\delta^{13}C_{CH2O}$	Carbon isotope of organic matter
	$\delta^{13}C_{CH4\text{-}bot}$	Carbon isotope of CH_4 at core bottom
	$\delta^{13}C_{CH4\text{-}SMTZ}$	Carbon isotope of CH_4 at the SMTZ
	$\delta^{13}C_{DIC\text{-}bot}$	Carbon isotope of DIC at core bottom
	$\delta^{13}C_{DIC\text{-}SMTZ}$	Carbon isotope of DIC at the SMTZ
C_T	Total concentration of carbon (*i.e.*, $^{12}C+^{13}C$)	
D	Diffusion coefficient	
f	Fraction of organic matter being utilized by POCSR	
ϕ	Porosity	
	ϕ_0	Porosity at water-sediment interface
	ϕ_f	Porosity at great depth
F_{in}	Flux into SMTZ	
	$F_{SO4.in}$	
	$F_{DIC.in}$	
	$F_{CH4.in}$	
	F_{Ca}	
F_{out}	Flux out from SMTZ	
	$F_{SO4.out}$	
	$F_{DIC.out}$	
	$F_{CH4.out}$	
γ	Empirical constant for porosity fitting	
k	Rate constant	
	k^L	Rate constant for light isotope
	k^H	Rate constant for heavy isotope
r	$^{13}C/^{12}C$ ratio	
	r_r	$^{13}C/^{12}C$ ratio of reactant
	r_p	$^{13}C/^{12}C$ ratio of product
	r_{std}	$^{13}C/^{12}C$ ratio of PDB standard (0.0112372)
	r_{OM}	$^{13}C/^{12}C$ ratio of organic matter
	r_{DIC}	$^{13}C/^{12}C$ ratio of DIC
	$r_{DIC\text{-}SMTZ}$	$^{13}C/^{12}C$ ratio of DIC at SMTZ
	$r_{CH4\text{-}SMTZ}$	$^{13}C/^{12}C$ ratio of CH_4 at SMTZ
	$r_{DIC\text{-}bot}$	$^{13}C/^{12}C$ ratio of CH_4 at the depth where isotopic value approaching a

		fixed value
	$r_{CH4\text{-}bot}$	$^{13}C/^{12}C$ ratio of CH_4 at the depth where isotopic value approaching a fixed value
$^{12/13}R$	Reaction rate for carbon 12 or 13	
	$^{12/13}R_{OM}$	Gross organic matter degradation rate
	$^{12/13}R_{POCSR\text{-}S}$	Rate of POC sulfate reduction in terms of sulfate consumption
	$^{12/13}R_{POCSR\text{-}C}$	Rate of POC sulfate reduction in terms of DIC production
	$^{12/13}R_{CP}$	Rate of carbonate precipitation
	$^{12/13}R_{AOM}$	Rate of anaerobic oxidation of methane
	$^{12/13}R_{ME\text{-}CH4}$	Rate methane production from methanogenesis
	$^{12/13}R_{ME\text{-}DIC}$	Rate DIC production from methanogenesis
	$^{12/13}R_{CR}$	Rate of CO_2 reduction
z	Depth in the sediments	

Appendix 2 The CrunchFlow input file for the transport-reaction model in Chapter 3

```
TITLE
UBGH2-1-1
END

RUNTIME
time_units        years
timestep_max      500.0
timestep_init     1.E-12
time_tolerance    0.1
hindmarsh         true
correction_max    2.0
debye-huckel      true
database_sweep    false
speciate_only     false
gimrt             true
graphics          kaleidagraph
fix_saturation    1.0
database          carbon_cycle.dbs
screen_output     50
Steady_state      false
END

OUTPUT
time_units        years
Spatial_profile   400000
END

PRIMARY_SPECIES
HCO3-
H13CO3-
CH4(aq)
13CH4(aq)
NH4+
HPO4--
HS-
SO4--
Fe++
H+
H2(aq)
Cl-
Ca++
Na+
Mg++
END

SECONDARY_SPECIES
CO2(aq)
13CO2(aq)
CO3--
13CO3--
NH3(aq)
H3PO4(aq)
H2PO4-
```

```
PO4---
H2S(aq)
S--
END

GASES
CO2(g)
13CO2(g)
H2S(g)
CH4(g)
13CH4(g)
END

MINERALS
Calcite-Ca -rate -9.7
Calcite-Mg -rate -10.7
CH2O_SO4 -rate -9.6
CH2O_ME -associate CH2O_SO4 -rate -9.8
Pyrite_FeS -rate -14.8
Mackinawite
END

AQUEOUS_KINETICS
AOM
13AOM
CO2_reduction
13CO2_reduction
END

TRANSPORT
distance_units centimeters
time_units  seconds
fix_diffusion         1.000e-5
D_25  Cl-             2.055e-5
D_25  Na+             1.349e-5
D_25  H+              9.328e-5
D_25  Mg++            7.040e-6
D_25  Ca++            8.075e-6
D_25  Fe++            7.060e-6
D_25  HCO3-           1.194e-5
D_25  H13CO3-         1.191e-5
D_25  CH4(aq)         1.850e-5
D_25  13CH4(aq)       1.821e-5
D_25  NH3(aq)         2.280e-5
D_25  HPO4--          7.685e-6
D_25  HS-             1.726e-5
D_25  SO4--           1.068e-5
D_25  H2(aq)          5.126e-5
D_25  CO2(aq)         1.916e-5
D_25  13CO2(aq)       1.910e-5
D_25  CO3--           9.305e-6
D_25  13CO3--         9.287e-6
D_25  NH4+            1.983e-5
D_25  H3PO4(aq)       9.595e-6
D_25  H2PO4-          9.595e-6
```

```
D_25  PO4---          6.195e-6
D_25  H2S(aq)         2.100e-5
D_25  S--             1.068e-5
diffusion_activation  4.539
cementation_exponent   1.9
END

BOUNDARY_CONDITIONS
x_begin   surface    Dirichlet
x_end     bottom     Dirichlet
END

INITIAL_CONDITIONS
surface 1-200
END

ION_EXCHANGE
exchange   X-
convention Gaines-Thomas
END

Condition surface
units           mol/kg
pH              7.8
set_porosity     0.8
HCO3-           2.2e-3
H13CO3-          0.02472184E-3
CH4(aq)         1e-9
13CH4(aq)        0.010731526e-9
NH4+          1e-4
HPO4--          1e-5
HS-             1e-9
SO4--           28e-3
Fe++            0.2e-2
H2(aq)          1e-9
Cl-             0.55
Ca++            0.01
Na+             charge
Mg++            0.05
Calcite-Ca         2e-2 1
Calcite-Mg         2e-2 1
CH2O_SO4         0.04 1
CH2O_ME          0.04 1
Pyrite_FeS       0.01 1
Mackinawite      0.01 1
X- -cec 1.5e-4
SolidDensity CalculateFromMinerals
END

Condition bottom
units           mol/kg
set_porosity     0.486
pH              7.6
HCO3-           70e-3
H13CO3-          0.79258219E-3
```

```
CH4(aq)          10e-3
13CH4(aq)        0.103719356e-3
NH4+             5e-3
HPO4--           1e-5
HS-              0
SO4--            0
Fe++             0.7e-2
H2(aq)           1e-9
Cl-              0.55
Ca++             0.0045
Na+              charge
Mg++             0.05
Calcite-Ca       2e-2 1
Calcite-Mg       2e-2 1
CH2O_SO4         0.04 1
CH2O_ME          0.04 1
Pyrite_FeS       0.01 1
Mackinawite      0.01 1
X- -cec 1.5e-4
SolidDensity CalculateFromMinerals
END

POROSITY
read_PorosityFile  UBGH2-1-1_porosity.txt
END

TEMPERATURE
set_temperature       1.3
temperature_gradient  0.1
END

DISCRETIZATION
xzones 200 0.1
distance_units meters
END

EROSION/BURIAL
time_units     years
distance_units meters
read_burialfile alkalinity_burial.dat FullForm
END
```

Appendix 3 CrunchFlow database used for the transport-reaction model in Chapter 3

```
'temperature points' 8   0.  25.  60. 100. 150. 200. 250. 300.
'Debye-Huckel adh'   0.4939  0.5114 0.5465 0.5995 0.6855 0.7994 0.9593 1.2180
'Debye-Huckel bdh'   0.3253  0.3288 0.3346 0.3421 0.3525 0.3639 0.3766 0.3925
'Debye-Huckel bdt'   0.0374  0.0410 0.0440 0.0460 0.0470 0.0470 0.0340 0.0000

'HCO3-' 4.0 -1.0    61.0171
'H13CO3-' 4.0 -1.0    62.0171
'CH4(aq)' 3.0 0.0 16.00
'13CH4(aq)' 3.0 0.0 17.00
'H2O' 3.0  0.0    18.0153
'Ca++' 6.0  2.0    40.0780

'Cl-' 3.0 -1.0    35.4527
'Fe++' 6.0  2.0    55.8470
'Fe+++' 9.0  3.0    55.8470
'H+' 9.0  1.0     1.0079
'H2(aq)' 9.0 0.0 1.0079
'HPO4--' 4.0 -2.0    95.9793
'HS-'   3.0 -1.0 33.08
'K+' 3.0  1.0    39.0983
'Mg++' 8.0  2.0    24.3050
'NH4+' 3.0 1.0    18.0306
'Na+' 4.0  1.0    22.9898
'SO4--' 4.0 -2.0    96.0636
'H2(aq)' 3.0 0.0 2.0159
'End of primary'  0.0  0.0  0.0

'CO2(aq)' 3   -1.0000 'H2O'    1.0000 'H+'    1.0000 'HCO3-'   -6.5804    -6.3447    -6.2684    -6.3882    -
      6.7235    -7.1969    -7.7868    -8.5280  3.0  0.0    44.0098
'CO3--' 2   -1.0000 'H+'    1.0000 'HCO3-'   10.6241    10.3288    10.1304    10.0836    10.2003    10.4648
      10.8707    11.4638  4.5 -2.0    60.0092
'13CO2(aq)' 3   -1.0000 'H2O'    1.0000 'H+'    1.0000 'H13CO3-'   -6.575157231 -6.340786483 -
      6.266007282 -6.387191367 -6.723849202 -7.198317074 -7.789078905 -8.530989082  3.0  0.0
      44.0098
'13CO3--' 2   -1.0000 'H+'    1.0000 'H13CO3-'   10.62438416 10.32896851 10.1304358 10.08351465
      10.20009546 10.46450148 10.87032548 11.46336275  4.5 -2.0    60.0092

'NH3(aq)' 2    -1.0000 'H+'    1.0000 'NH4+'  10.0691    9.2410    8.2847    7.4010    6.5156    5.7992
      5.1995    4.6767  2.5  0.0    18.0385
'H2PO4-' 2    1.0000 'H+'    1.0000 'HPO4--'   -7.3231    -7.2054    -7.1888    -7.2876    -7.5259    -7.8671    -
      8.3189    -8.9357  4.0 -1.0    96.9872
'H3PO4(aq)' 2    1.0000 'HPO4--'    2.0000 'H+'   -9.3933    -9.3751    -9.5434    -9.8805   -10.4425   -
      11.1429   -12.0169   -13.1928  3.0  0.0    97.9952
'PO4---' 2   -1.0000 'H+'    1.0000 'HPO4--'   12.6048    12.3218    12.1275    12.0760    12.1809    12.4313
      12.8214    13.3896  4.0 -3.0    94.9714
'H2S(aq)' 2    1.0000 'H+'    1.0000 'HS-'   -7.4159    -6.9877    -6.6467    -6.4827    -6.4960    -6.6831    -
      7.0225    -7.5536  3.0  0.0    34.0819
'S--' 2   -1.0000 'H+'    1.0000 'HS-'   13.7100    12.9351    12.0082    11.1018    10.1202    9.2545    8.4250
      7.5568  5.0 -2.0    32.0660
'FeS(aq)' 3 -1.00 'H+' 1.00 'Fe++' 1.00 'HS-' -4.6480 -4.6480 -4.6480 -4.6480 -4.6480 -4.6480 -4.6480 -
      4.6480 3.0 0.0 87.9110
'End of secondary' 1 0. '0' 0. 0. 0. 0. 0. 0. 0. 0. 0. 0. 0.
```

```
'CO2(g)'    0.0000  1    1.0000 'CO2(aq)' -0.4 -0.4 -0.4 -0.4 -0.4 -0.4 -0.4 -0.4 44.0098
'13CO2(g)'    0.0000  1    1.0000 '13CO2(aq)' -0.400510835 -0.400461052 -0.400403915 -0.400351746 -
      0.400300412 -0.400259931 -0.40022719 -0.400200164  44.0098
'CH4(g)'    0.0000  1    1.0000 'CH4(aq)'   -2.5846    -2.8502    -3.0228    -3.0582    -2.9646    -2.7795    -
      2.5344    -2.2310    16.0428
'13CH4(g)'    0.0000  1    1.0000 '13CH4(aq)'   -2.584947575 -2.850547575 -3.023147575 -3.058547575 -
      2.964947575 -2.779847575 -2.534747575 -2.231347575    16.0428

'H2S(g)'    0.0000  2    1.0000 'H+'    1.0000 'HS-'   -8.0781    -7.9759    -7.9295    -7.9572    -8.0759    -
      8.2750    -8.5671    -9.0074    34.0819
'End of gases' 0. 1 1. '0' 0. 0. 0. 0. 0. 0. 0. 0. 0.

'Calcite-Ca'   36.9340  4   -1.0000 'H+'    1.0000 'Ca++'    0.989305424 'HCO3-' 0.010694576 'H13CO3-'
      2.2257     1.8487     1.3330     0.7743     0.0999    -0.5838    -1.3262    -2.2154   100.0872
'Calcite-Mg'   36.9340  4   -1.0000 'H+'    1.0000 'Mg++'    0.989305424 'HCO3-' 0.010694576 'H13CO3-'
      2.2257     1.8487     1.3330     0.7743     0.0999    -0.5838    -1.3262    -2.2154   84.21413
'Pyrite_FeS' 23.94 3 -1.00 'H2(aq)' 1.00 'H2S(aq)' 1.00 'Mackinawite'  -6.5285  -5.9811  -5.3527  -4.7789  -
      4.2142  -3.7689  -3.4087  -3.1113 119.9790
'CH2O_SO4' 28.81 7 -1 'SO4--' -0.264 'H+' 1.0 'H2S(aq)' 1.978281341 'HCO3-' 0.021718659 'H13CO3-'
      0.302 'NH4+' 0.019 'HPO4--' 4 4 4 4 4 4 4 4 67.037
'CH2O_ME' 28.81 9 -0.264 'H2O' 0.989712522 'CH4(aq)' 0.010287478 '13CH4(aq)' 0.727578763
      'CO2(aq)' 0.008421237 '13CO2(aq)' 0.260979678 'HCO3-' 0.003020322 'H13CO3-' 0.302 'NH4+'
      0.019 'HPO4--' 4 4 4 4 4 4 4 4 67.037
'Mackinawite' 23.94 3 -1.0 'H+' 1.0   'Fe++'  1.0 'HS-' -4.648 -4.648 -4.648 -4.648 -4.648 -4.648 -4.648 -
      4.648 87.911
'End of minerals' 0. 1 0. '0' 0. 0. 0. 0. 0. 0. 0. 0. 0.

Begin aqueous kinetics
AOM 1 'monod' 5  -1.0 'SO4--'  -1 'CH4(aq)' 1 'HCO3-' 1.0 'HS-' 1.0 'H2O' 5.8
  0.5e-4    2 'SO4--' 5e-4  'CH4(aq)' 5e-3
  'Inhibition' 0
13AOM 1 'monod' 5  -1.0 'SO4--'  -1.0 '13CH4(aq)' 1.0 'H13CO3-' 1.0 'HS-' 1.0 'H2O' 5.8
  0.3960396e-6   2 'SO4--' 5e-4 '13CH4(aq)' 4e-5
  'Inhibition' 0
CO2_reduction 1 'monod' 5  -4.0 'H2(aq)'  -1.0 'HCO3-' -1.0 'H+' 1.0 'CH4(aq)' 3.0 'H2O' 40.25
  2.35e-5  2 'H2(aq)' 1e-6  'HCO3-' 1e-2
  'Inhibition' 1 'SO4--'  1e-4

13CO2_reduction 1 'monod' 5  -4.0 'H2(aq)'  -1.0 'H13CO3-' -1.0 'H+' 1.0 '13CH4(aq)' 3.0 'H2O' 40.25
   1.9E-07       2 'H2(aq)' 1e-6  'H13CO3-' 8.8730E-05
  'Inhibition' 1 'SO4--'  1e-4

End of aqueous kinetic

Begin mineral kinetics
+-----------------------------------------------------
CH2O_SO4
  label = default
  type  = monod
  rate(25C) = -12.40
  activation = 0.0  (kcal/mole)
  monod_terms :  SO4--  100e-06
  inhibition :
  1 ch2o_so4 + 14 h+ + 53 so4-2 --> 53 h2s(aq) +  1 hpo4-2 + 16 nh4+ + 106 hco3-
+-----------------------------------------------------
```

```
CH2O_ME
  label = default
  type  = monod
  rate(25C) = -12.40
  activation = 0.0  (kcal/mole)
  monod_terms :
  inhibition : SO4--  1600.0e-06 HCO3- 15e-3 CH4(aq) 15e-3
  1 ch2o_so4 + 14 h+ + 53 so4-2 --> 53 h2s(aq) +  1 hpo4-2 + 16 nh4+ + 106 hco3-
+-----------------------------------------------------
Calcite-Ca
  label = default
  type  = tst
  rate(25C) = -6.19
  activation = 15.0  (kcal/mole)
  dependence : HCO3- 1.0
  1.0 Calcite + 1.0 H+ =  1.0 Ca+2 + 1.0 HCO3-
+-----------------------------------------------------
Calcite-Mg
  label = default
  type  = tst
  rate(25C) = -6.19
  activation = 15.0  (kcal/mole)
  dependence : HCO3- 1.0
  1.0 Calcite + 1.0 H+ =  1.0 Ca+2 + 1.0 HCO3-
+-----------------------------------------------------
Pyrite_FeS
  label = default
  type  = tst
  rate(25C) = -8
  activation = 15.0  (kcal/mole)
  dependence :
+-----------------------------------------------------
Mackinawite
  label = default
  type  = tst
  rate(25C) = -8.90
  activation = 0.0  (kcal/mole)
  dependence :
  1.0 FeS(am) + 1.0 H+ =  1.0 Fe+2 + 1.0 HS-
+-----------------------------------------------------
End of mineral kinetics
Begin exchange
'NaX'   2 1.0 'Na+'  1.0 'X-'   0.00  0.000
'KX'    2 1.0 'K+'   1.0 'X-'  -0.48  0.000
'CaX2'  2 1.0 'Ca++' 2.0 'X-'  -0.99  0.000
'MgX2'  2 1.0 'Mg++' 2.0 'X-'  -0.86  0.000
'NH4X'  2 1.0 'NH4+' 1.0 'X-'  -0.48  0.000
'NaXhan_zach1' 2  1.0 'Na+' 1.0 'Xhan_zach1-'          6.76  0.000
'NaXhan_zach2' 2  1.0 'Na+' 1.0 'Xhan_zach2-'          2.20  0.000
'CsXhan_zach1' 2  1.0 'Cs+' 1.0 'Xhan_zach1-'          0.00  0.000
'CsXhan_zach2' 2  1.0 'Cs+' 1.0 'Xhan_zach2-'          0.00  0.000
'NaXhan1' 2  1.0 'Na+' 1.0 'Xhan_col1-'               6.99  0.000
'NaXhan2' 2  1.0 'Na+' 1.0 'Xhan_col2-'               2.52  0.000
'CsXhan1' 2  1.0 'Cs+' 1.0 'Xhan_col1-'               0.00  0.000
'CsXhan2' 2  1.0 'Cs+' 1.0 'Xhan_col2-'               0.00  0.000
```

```
'NaXhan1' 2  1.0 'Na+' 1.0 'Xhan1-'          7.388  0.000
'NaXhan2' 2  1.0 'Na+' 1.0 'Xhan2-'          4.301  0.000
'NaXhan3' 2  1.0 'Na+' 1.0 'Xhan3-'          1.906  0.000
'KXhan1' 2  1.0 'K+' 1.0 'Xhan1-'           5.034  0.000
'KXhan2' 2  1.0 'K+' 1.0 'Xhan2-'           2.287  0.000
'KXhan3' 2  1.0 'K+' 1.0 'Xhan3-'           1.050  0.000
'Ca0.5Xhan1' 2  0.5 'Ca++' 1.0 'Xhan1-'      7.906  0.000
'Ca0.5Xhan2' 2  0.5 'Ca++' 1.0 'Xhan2-'      5.202  0.000
'Ca0.5Xhan3' 2  0.5 'Ca++' 1.0 'Xhan3-'      1.764  0.000
'CsXhan1' 2  1.0 'Cs+' 1.0 'Xhan1-'          0.00  0.000
'CsXhan2' 2  1.0 'Cs+' 1.0 'Xhan2-'          0.00  0.000
'CsXhan3' 2  1.0 'Cs+' 1.0 'Xhan3-'          0.00  0.000
'NaXhan1' 2  1.0 'Na+' 1.0 'Xhan1a-'          6.99  0.000
'NaXhan2' 2  1.0 'Na+' 1.0 'Xhan2a-'          2.34  0.000
'CsXhan1' 2  1.0 'Cs+' 1.0 'Xhan1a-'          0.00  0.000
'CsXhan2' 2  1.0 'Cs+' 1.0 'Xhan2a-'          0.00  0.000
End of exchange
```

Appendix 4 Graphic presentation of the model scheme in Chapter 5. For each time step, a 5-meter sediment layer was added then the sediment column was allowed to evolve chemically for a time period equivalent to that needed for the 5-meter sediment to accumulate (i.e., 5 m divided by the sedimentation rate). The initial condition for each step was the output of the previous step. Upper boundary condition was set to be bottom seawater composition whereas the lower boundary condition was always the composition of the volcanic basement, which was inferred from the deepest pore water measurements. In the sediment column, porosity was assigned following the observed profiles; reaction and the chemistry were allowed to evolve with time. In contrast, in the basement aquifer, porosity was fixed to be a constant value and reactions were set to be inactive.

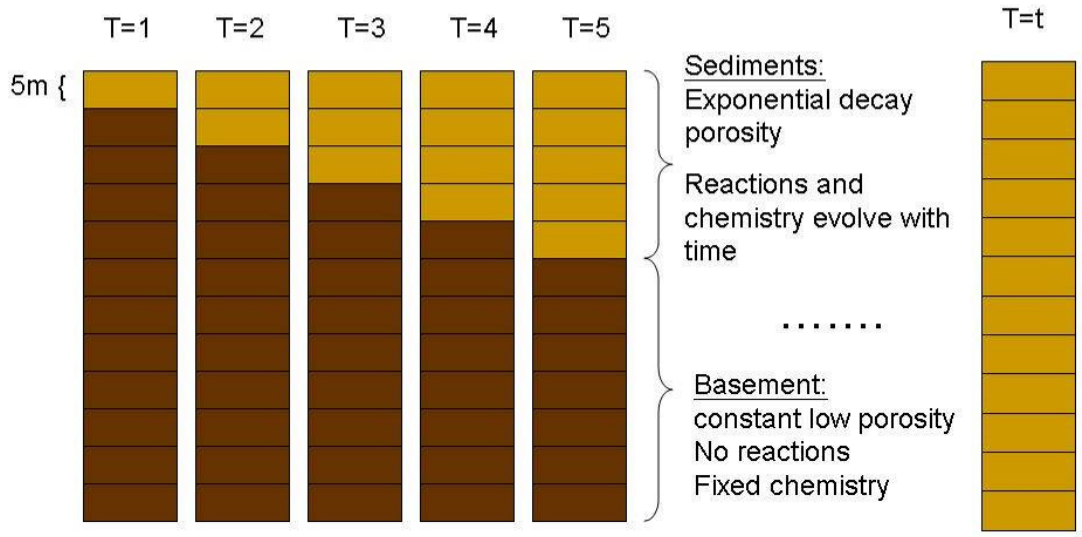

Appendix 5 Test of different lower boundary conditions in Chpater 5. In one simulation (solid blue line), the lower boundary condition was set to evolve from the composition of bottom seawater to the volcanic basement aquifer. In the other simulation (dash blue line), the boundary condition was always fixed as the basement aquifer composition. Due to the faster rate of diffusion than of sedimentation, pore water composition rapidly responds to the changes in the lower boundary condition. The resulting profile at 20 Myr is similar between the two trials. The resulting ash alteration rates estimated by these two trials are only 3.6% different. As we have no direct data on how the basement aquifer composition evolved with time, we adopted the fixed lower boundary condition in this study.

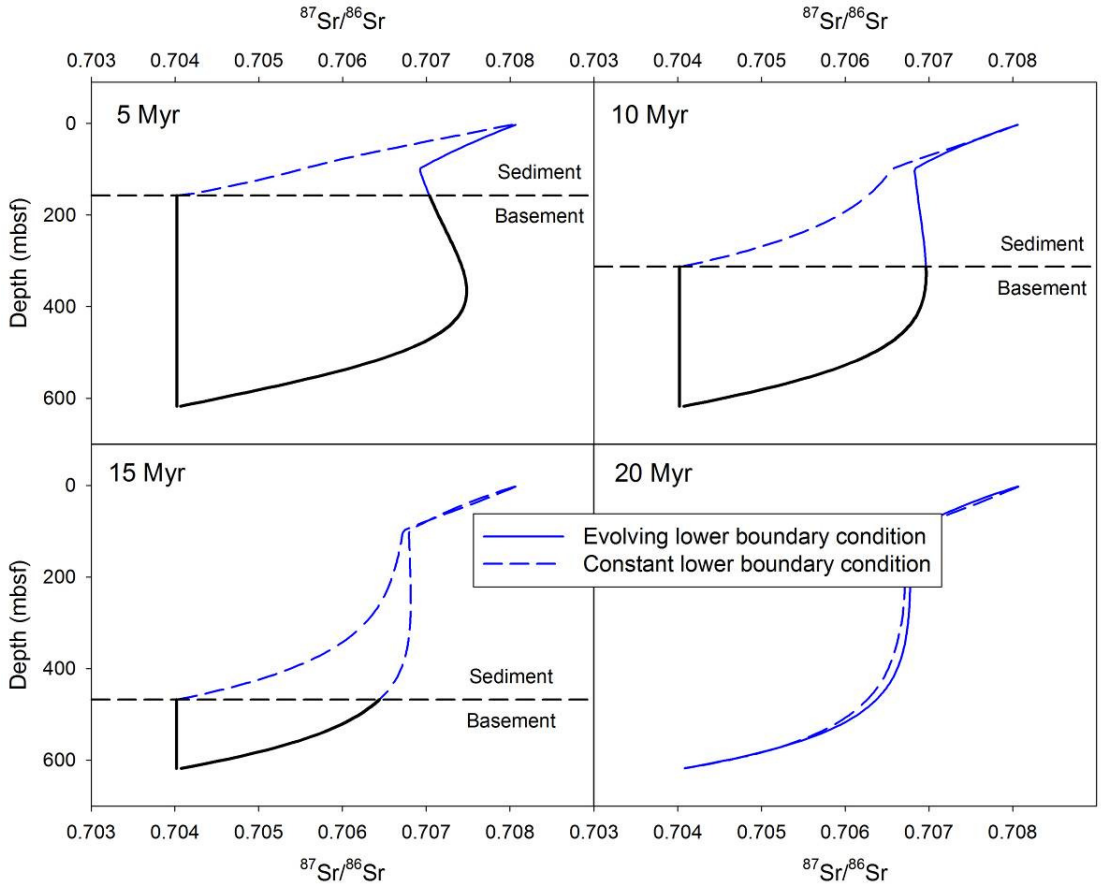

Appendix 6 Sensitivity tests on ash alteration rate using Sr isotopes and volcanic ash content in Chapter 5. Results of such test show that both Sr isotopes and volcanic ash profiles are very sensitive to the chosen ash alteration rate and therefore these data provide good constraints on reaction rates.

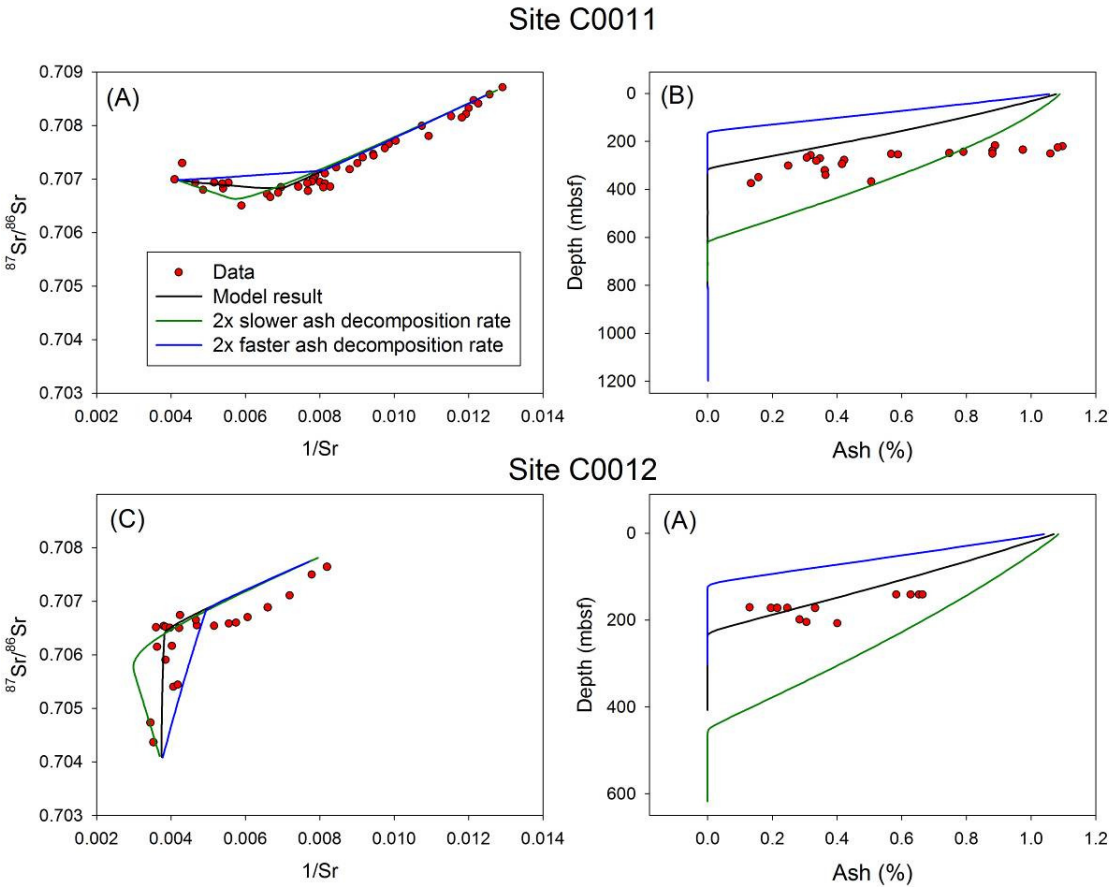

Appendix 7 Model setup for the tests of different lower boundary conditions in Chapter 5.

	Evolving bottom boundary condition	Constant bottom boundary condition
Bottom water condition	Volcanic ash input, $^{87}Sr/^{86}Sr$=0.7095	
Volcanic basement condition	No ash, $^{87}Sr/^{86}Sr$=0.7040	
Upper boundary condition	Bottom water condition	
Initial lower boundary condition	Bottom water condition	Volcanic basement condition
Final lower boundary condition	Volcanic basement condition	